Fermionic Quantum Information in Surface Acoustic Waves

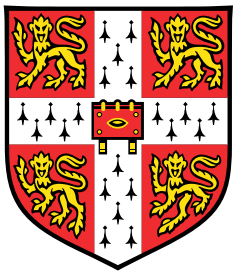

Hugo Vincent Lepage

Cavendish Laboratory
University of Cambridge

This dissertation is submitted for the degree of
Doctor of Philosophy

St Edmund's College

April 2020

DECLARATION

I hereby declare that except where specific reference is made to the work of others, the contents of this dissertation are original and have not been submitted in whole or in part for consideration for any other degree or qualification in this, or any other university. This dissertation is my own work and contains nothing which is the outcome of work done in collaboration with others, except as specified in the text and Acknowledgements. This dissertation contains fewer than 60,000 words including appendices, bibliography, footnotes, tables and equations and has fewer than 150 figures.

Hugo Vincent Lepage
April 2020

Abstract

Fermionic Quantum Information in Surface Acoustic Waves

Hugo Vincent Lepage

Quantum computers are on the verge of revolutionising modern technology by providing scientists with unparalleled computational resources. With quantum-mechanical phenomena such as the superposition principle and entanglement, these computers could solve certain computational problems that are otherwise impossible for even the most powerful classical supercomputers. One of the major challenges standing in the way of this computing revolution is the accurate control of quantum bits. Quantum systems are extremely fragile and, by their nature, cannot be measured without destroying their quantum state.

I wrote a numerical program to solve the time-dependent Schrödinger equation, the differential equation that describes the evolution of wave functions. The advantage of my code over other solvers is its speed. I used graphics processing units (GPUs), a technology that has only recently matured, to accelerate high-performance computing. Hardware-acceleration allows me to solve complex time-evolution problems within days rather than years. Such an exceptional speedup has enabled me to calculate the behaviour of single electrons in semiconductor devices. Electrons are particularly interesting because they are ubiquitous in modern technology, as well as being fundamental quantum particles. Using the simulations produced by my code, I track the time evolution of an electron wave function as it propagates along quantum circuits. By animating the evolution of the wave function, I am able to visualise the wave function of electrons propagating in space and time. This is a remarkable tool for studying the behaviour of quantum particles in nanodevices. I focused my thesis on the realistic modelling of devices that are readily available in a laboratory or on designs that could be fabricated in the near future. I began by modelling single electrons as quantum bits. I provide a definition for an optimal qubit and lay out the set of operations required to manipulate the quantum information carried by the electron.

In all my simulations, I aim to model experimentally realistic devices. I calculated the electrostatic potential of a real nanodevice and simulated the time-evolution of a single electron. I show that it is possible to create a single-electron beam splitter by tuning the voltages applied to various parts of the device and I calculate the range of voltages in which quantum information is preserved and manipulated accurately. These results were verified experimentally by collaborators at the Institut Néel and were published in *Nature Communications 10, 4557 (2019)*.

Using my code, I developed a framework for general measurements of electron qubits and provided a design for a semiconductor device capable of performing positive-operator valued measures (POVMs). A POVM is a powerful measurement technique in quantum mechanics that allows quantum information to be manipulated in interesting ways. The proposed setup is suggested as an implementation of entanglement distillation, which is a useful error correction tool that transforms an arbitrary entangled state into a pure Bell pair. Entanglement is one of the most fascinating aspects of quantum mechanics and it remains a challenge to generate perfectly entangled particle pairs. An experimentally viable method for distilling – or perfecting – entanglement is crucial for the design of quantum computers or quantum communication systems. Using this design, I introduced a protocol to use electrons, rather than photons, in quantum-optics-like systems. These results were published in *Phys. Rev. A 96, 052305 (2017)*.

Going beyond single-particle behaviour, I compare different methods for generating entanglement between electron-spin qubits using the power-of-SWAP operation. By using realistic experimental parameters in my simulations, I demonstrate that generating entanglement via electron-electron collisions in a harmonic channel cannot be implemented for multidimensional systems. These findings go against what researchers thought was possible and put forward the need for new solutions to particle entanglement. I provide an alternative by demonstrating that a method based on the exchange energy is more viable than previously thought. I present a semiconductor device structure and an electrostatic potential that experimental groups can use in order to obtain the most efficient entangling quantum logic gates. These findings were published in *Phys. Rev. A 101, 022329 (2020)*.

The results presented in this thesis provide a comprehensive description of the control of single electrons in a surface-acoustic-wave-based quantum circuit. However, work in this field is far from over. I present various research paths for future projects. These include going beyond the time-dependent Schrödinger equation to capture more complicated dynamics, using different hardware solutions to further accelerate numerical problem solving, and studying new systems of interest to extend this project beyond semiconductor physics.

ACKNOWLEDGEMENTS

First and foremost, I should thank my supervisor, Prof. Crispin H. W. Barnes, for his continued support of my research. My PhD has been an incredible learning experience and some of the best years of my life. I will forever remember this time with great fondness and I hope we will continue working together far into the future.

I would also like to thank Prof. Chris Ford who has had my back since my very first day in Cambridge during the summer of 2012. Your encouragement and your comments have ensured that I strive for excellence in my research.

I extend my gratitude to Dr. Stuart Holmes and Dr. Masaya Kataoka, my *Viva Voce* examiners. Your insight into my work was very profound and I found the examination to be an enriching experience.

My academic journey was far from lonely and I am delighted to have spent it in the wonderful environment that is the University of Cambridge. I would like to acknowledge in particular the members of the Semiconductor Physics Group and the Quantum Information Group at the Cavendish Laboratory. Whether they be formal group meetings, discussions on the lawn, or chaotic scribblings on office windows, our interactions have always been enriching. To my group members, Jacek Mosakowski, David Arvidsson Shukur, Aleksander Lasek, Kexin Zhang, Yordan Yordanov, and Niall Devlin, I am thankful for our time spent together inside and out of the Cavendish Lab. Our healthy work environment has allowed me to expand my comfort zone to new levels. To my Cavendish lunch crew, Ankita Anirban and Hippolyte Astier, although sometimes the duration of our meals was a little bit exaggerated, I would always consider it time well spent. A warm thank you is due to the SAWtrain network; we have had some great times together and I always looked forward to our network meetings. I would like to give a special thanks to Hermann Edlbauer, Chris Bäuerle, and Shintaro Takada for being such amazing research collaborators.

I will forever see Cambridge as a great learning opportunity. Conversations, from the most basic to the most elevated, can readily be found everywhere throughout the city. I can't think of a better group than *ze boot* to highlight both of these extremes. In alphabetical order, I would like to give a special thanks to the members of this friend group who have made my

stay in Cambridge extra *guud*: Aleksander Lasek, Bono Xu, Bram van der Velden, Daniel Chiriţoiu, Dario Palumbo, David Arvidsson Shukur, Eleni Courea, Elisabetta Garletti, Enrico Ghiorzi, Hippolyte Astier, Marianne Haroche, Martin Schlegel, Sophie Morrison, and Susie Ní Chróinín. Sophie, thank you for always believing in me. You were there for the best and also the toughest parts of my PhD. Now that it's all done, we are well overdue a solid celebration! David, I am so glad that an informal interview at the pub has since developed into such a treasured friendship. You are destined for great things and I hope to be at your side to see them materialise.

À mes amis au Canada, merci d'avoir été si proche quand j'étais si loin. Je me suis toujours senti inclus dans toutes vos aventures et péripéties. Gabriel Bouchard Roby, Josué Djossou, Maxime Gagnon Lemay, Patrick Lasserre, Philip Hague et Tristan Delorme, j'ai très hâte de vous revoir! Noémie, je ne sais pas où je serais sans toi. Tu m'as fait découvrir le monde entier et tu fais de moi une personne meilleure.

Maman, tu m'orientes toujours vers l'excellence, de la première année du primaire jusqu'au doctorat et plus loin encore j'espère. Ça me fait toujours un immense plaisir d'entendre que tu es fière de moi et je veux te dire que moi aussi, je suis fier de t'avoir comme mère.

To my dad, your imagination and continuous curiosity about the unknowns of the world is a great source of inspiration. I will never get tired of our conversations about science, art, or philosophy. I look forward to future travels with you, wherever in the world that may be.

Finally, I would like to express my sincere gratitude to the various organisations that have supported my studies and research financially: The Institute of Physics, the Marie Skłodowska Curie Actions, the Fonds de Recherche du Québec – Nature et technologies, St Edmund's College, the Canadian Imperial Bank of Commerce, the Canadian Centennial Scholarship Fund, and the Institute of Engineering and Technology.

TABLE OF CONTENTS

List of Figures

1

INTRODUCTION

Calculating tools have been used for thousands of years to help us tackle complex problems. As early as 2700–2300 BCE, Mesopotamian scholars were using an early form of the abacus to aid them in computational tasks such as addition and subtraction in a sexagesimal base system. Over several millennia, number systems evolved to include different base systems, a well defined ordered set of numbers, the concept of zero, and a modern labelling system amongst other improvements [82]. However, computation tools did not evolve much from the original abacus. The first century CE marks the earliest archaeological record of a Roman "pocket abacus". This small metal plate with sliding beads, each of which is associated to a different order of magnitude, was not very different from the Babylonian bead abacus in function. Although the abacus was helpful to evaluate larger arithmetic problems, it did not compute anything itself; it was merely a tool to help humans calculate. It wasn't until the end of the European Renaissance that true calculating machines were developed. Gears and levers were assembled into a so-called "calculating clock" that could perform arithmetical operations such as addition and subtraction purely mechanically, with minimal input from the user.

Throughout the years of the industrial revolution, mechanical calculators were developed to handle more difficult problems and to count to larger numbers. Between the years 1834 and 1836, the English mathematician and inventor Charles Babbage drafted the theoretical design

for the Analytical Engine. This machine would be the first capable of universal computations since memory and processing power were theoretically unlimited. The engine would also be capable of complex algorithms owing to its ability to process conditional statements. It was Ada Lovelace, an English mathematician, who first understood the possibilities and future of computing machines. Together, Charles Babbage and Ada Lovelace are recognised as the father of the computer and the first computer programmer.

It wasn't until the early 20th century, when electricity had become widely available, that the development of electromechanical calculating machines opened a new realm of possibilities for such devices. These calculators were initially used mostly for accounting purposes. During the second world war, the need for more complex operations to be carried out led to the development of modern computers as we know them. The British *Colossus Mk1* (1943), the first electronic digital programmable computer, and the American *ENIAC* (1946), the first Turing-complete device, were constructed for the purposes of decryption and ballistic-trajectory calculations, respectively [82, 71, 42].

When transistors replaced vacuum tubes in computer designs in 1955, it became an engineering problem to increase computer performance. The miniaturization of microelectronic components on integrated circuits led Gordon Moore to propose the famous "Moore's Law" in 1965 stating that semiconductor complexity would double annually. This law was revised in 1975 when Moore suggested that this rate would decrease around 1980 to a complexity doubling every two years [30]. Moore's prediction has been accurate over the decades since its inception, however, at the time of writing this thesis, semiconductor transistors have reached a size of approximately 10nm and are predicted to reach their physical limit due to quantum tunnelling at 5nm. This limit effectively marks the end of Moore's Law and the end of high-paced advancements in classical computing performance [91, 152, 135]. Although computational resources may be stunted for classical systems, a new era of computing is on the horizon through the development of quantum computers.

1.1 Quantum Computing

The Church-Turing-Deutsch (CTD) principle [46, 154] states that: "every finitely realisable physical system can be perfectly simulated by a universal model computing machine operating by finite means." In other words, there could exist a computation tool capable of simulating any finite physical process. A quantum system can simulate itself, but can also be used to simulate a different system of equivalent complexity. Since the complexity of a quantum system increases exponentially with the number of particles, computing resources

are not limited by classical standards [1]. Complex problems with a high dimensionality are no longer impossible to solve at a practical level.

The exploitation of quantum systems can also be tailored to specific tasks through the use of quantum algorithms. Two of the most well known algorithms are Shor's algorithm for finding the prime factors [16, 142] of large integers and Grover's algorithm for inverting functions. In a more applied sense, Grover's algorithm could be used for searching large data structures [73].

Analogous to the fundamental unit of information of a classical computer, the binary digit, or bit, defined by a 0 or a 1, the basic unit of information of a quantum computer is the quantum bit, named *qubit*. A qubit is an arbitrary superposition of a two-level quantum state $\alpha|0\rangle + \beta|1\rangle$, where α and β are complex numbers [162, 136]. There exist additional schemes for other units of information such as the *qutrit* for 3-level systems or the *qudit* for arbitrary d-level quantum systems, each offering their advantages and drawbacks. However, these unit systems are beyond the scope of this research.

A qubit can be encoded onto many physical systems. Proposed quantum computing platforms include the optical manipulation of atoms [155] or ions [52], the use of superconducting Josephson junctions [58, 145], and quantum dots in GaAs [144]. Quantum information can also be carried by single photons and single electrons [112]. In this thesis, I am mainly focused on single electrons as the carriers of quantum information. Single-electron qubits are often referred to as spin or charge qubits, but as is discussed by Owen *et al.*, the dynamics of an electron are complex and the spin and charge components are not independent [122]. It was shown that the spin-orbit interaction (SOI) causes a coherent-state spin qubit to precess around the Bloch sphere. This precession is especially relevant when two electron qubits interact with each other as it can cause them to be entangled conditionally, thus effectively acting as a two-qubit gate. A definition of the Bloch sphere is presented in Sec. 1.1.3.

1.1.1 Why Quantum Computers?

In recent years, quantum technologies have gained an enormous amount of attention. Claims that quantum computers would be exponentially faster than any technology currently available has led to the inception of terms such as "quantum supremacy" [126] and, in a less extreme version, "quantum advantage". Quantum supremacy defines a threshold at which it becomes impossible for a classical computer to simulate – and therefore verify – the results produced by a quantum computer. The problem that the computers are attempting to solve do not need to be useful in any practical way to demonstrate quantum supremacy. Quantum advantage relaxes the definition of supremacy, simply requiring that a quantum computer be faster at

a given task than its classical counterpart. Quantum advantage is more straightforward to verify since a classical computer can calculate the solution to the problem and therefore validate the accuracy of the quantum computation. In 2019, Google claimed that they had achieved quantum supremacy using their superconducting processor [7], stating that:

> Our Sycamore processor takes about 200 seconds to sample one instance of a quantum circuit a million times – our benchmarks currently indicate that the equivalent task for a state-of-the-art classical supercomputer would take approximately 10,000 years. This dramatic increase in speed compared to all known classical algorithms is an experimental realization of quantum supremacy for this specific computational task, heralding a much-anticipated computing paradigm.

Given these bold definitions as well the hype that has been generated around quantum computers, it is easy to be deceived in thinking that this technology is the Holy Grail of information science and that every computer will be quantum in the next few years. From claims that "a quantum computer could break 2048-bit RSA encryption in 8 hours"[56] to pop culture references, quantum computers are made out to be some magical do-all device with seemingly no limits. Although it is important to remain skeptical towards extraordinary claims, one shouldn't discard quantum computers since their true potential could be revolutionary in many fields of science as well as industry. The most straightforward implementation of quantum computers – simulating quantum systems – has already led to breakthroughs in physics, chemistry, and nanotechnology. In this section, I will go over the realistic advantages of a quantum computer, the motivation behind the extensive research in the field, and the limitations of this technology[1].

The acceleration attributed to quantum computers comes from algorithms reducing the complexity of a certain set of problems. This does not necessarily imply that quantum computers run faster or can accomplish basic operations or clock cycles in less time. Instead, the use of quantum computers changes the way problems scale. When discussing the computational complexity of a problem, it is useful to use Big O notation, which describes the growth rate of a problem in the limit when it is large. For example, searching for a particular element in an unordered list of N elements is of order $\mathcal{O}(N)$. Given that there is no structure in the data, one would have to check every entry, one by one, to find the correct answer. On average, a solution is found after $N/2$ queries, but this problem scales linearly with N. Running Grover's algorithm on a quantum computer would reduce the complexity of the search problem to $\mathcal{O}(\sqrt{N})$ [73, 74]. Another famous example of the acceleration provided by quantum computers is the Deutsch–Jozsa algorithm[47]. The problem statement goes as

follows: a black box takes an N-bit input and outputs a single binary digit (either a 0 or a 1). The function within the black box is either constant (it always outputs a 0 or always a 1) or it is balanced (half of the inputs yield a 0 and half yield a 1). In order to test whether the function is constant or balanced without uncertainty, a classical computer requires $\mathcal{O}(2^N)$ trial input states. This exponential scaling with the number of input bits quickly makes this problem impossible for even the most advanced supercomputers. However, by using the Deutsch-Jozsa algorithm on quantum computers, the solution can be found exactly in one query, reducing the problem to $\mathcal{O}(1)$.[47]

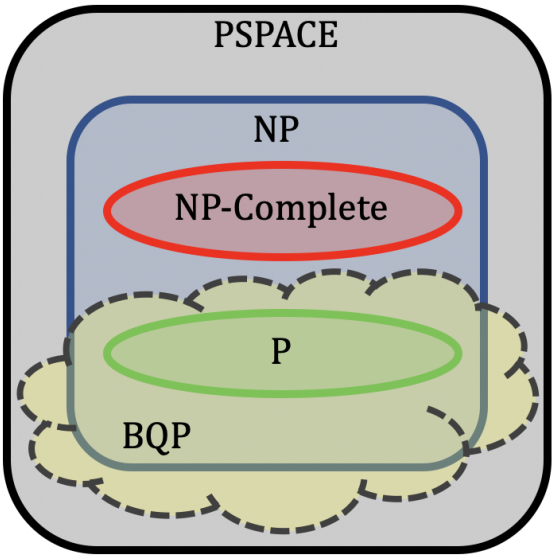

Fig. 1.1 Relation between the different complexity classes. The boundaries of BQP are not well defined.

Although quantum computers will not provide a speedup to every type of decision problem, they are expected to reduce the complexity of problems from the bounded-error quantum polynomial time (BQP) class. Figure 1.1 illustrates the expected relation between BQP and other computational complexity classes. Complexity classes are a useful tool to compare the difficulty of a computational problem [70, 6]. The field of computational complexity theory is thriving, with the P versus NP problem being one of the Millennium Prize Problems offered by the Clay Institute [37]. The complexity classes compared in Fig. 1.1 are the following:

P problems: The class of problems that can be solved in deterministic way by a computer in polynomial time. Example: Calculating the greatest common divisor (gcd) between two integers will have at most a complexity of $\mathcal{O}(N^2)$ for a number of size N [95]. Note that two integers are said to be coprime if their gcd is 1.

NP problems: Nondeterministic polynomial problems are those that are verifiable in polynomial time using a deterministic machine. Ones whose solutions are easy to verify. Example: The decision version of the travelling salesman problem. Given a number of cities and the relative distances between them, is there a path with total length less than x? Although the problem itself is hard to solve, the verification of the solution, once found, is possible in polynomial time. In this case, the distances between cities for the final path are summed and compared to x.

NP-complete problems: This subset of the NP class shares the same solution to any problem within NP-complete. If a solution that is more efficient than a brute force approach can be found, the same solution can be used for all other problems. Example: Solving an $N \times N$ Sudoku is hard, but can be verified in polynomial time. The solution to an arbitrary Sudoku can be mapped onto the full travelling salesman problem [69], graph coloring [85], bin packing [19], and many other combinatorial, graph, and game problems.

BQP problems: Problems in the bounded-error quantum polynomial class are solvable by a quantum computer in polynomial time. The solution to a BQP problem does not need to be found using a deterministic algorithm, meaning that the answer produced is always correct. BQP requires that the probabilistic error rate of an algorithm be at most 1/3 for all instances [118]. Example: Shor's algorithm reduces the complexity class for factoring prime numbers from sub-exponential to $\mathcal{O}((\log N)^2(\log\log N)(\log\log\log N))$, which is polynomial in $\log N$ [142].

PSPACE problems: This class represents the set of decision problems that are solved using a polynomial amount of space. This is a limitation on storage space for finding the solution to the problem. Although algorithms in PSPACE are not explicitly bounded in time, finite space requirements also imply finite time requirements [6, 35]. Example: Generalized chess and Go, played on an $N \times N$ grid, are examples of games that require a polynomial storage space. The solution to these games are not found in polynomial time. Both of these games require algorithms with time complexity that scales exponentially with the size of the grid [146].

There are several real-world application problems that could, in principle, be solved by classical computers but in practice require an unreasonable amount of time or computational resources. One of the most well known problems is large integer factorisation [16]. The complexity of finding the prime factors of large composite numbers exceeds the computational capacity of classical computers. This principle is currently the basis for the RSA encryption algorithm [130].

Another problem that is not realistically solved by current computers is the simulation of many-body quantum systems. The complexity of such a problem grows exponentially with the number of particles in the simulation such that the state of a system of N particles with m accessible energy levels is described by an m^N-dimensional complex vector with a Hamiltonian represented by an $m^N \times m^N$ matrix. For example, an N-particle system where each particle has two levels would require more bits than there are atoms in the observable universe to simulate classically if $N > 300$. There are many reasons for simulating physical systems, both quantum and classical. Simulations allow us to analyze simpler models of the physical systems and quantify the effects of assumptions and constraints on the model. Simulations also provide insight into systems that are otherwise inaccessible experimentally owing to technological or even physical limitations. For example, simulations provide the full wave function $|\psi\rangle$ of a quantum system whereas an experimental setup can only measure the probability of an outcome A, $|\langle\psi_A|\psi\rangle|^2$. A quantum system can be set up, manipulated and have its properties measured to acquire information related to its state after manipulation. Richard Feynman used this idea to propose the possibility of exploiting quantum mechanical processes to store data and operate on it to execute computational tasks [60]. Feynman's suggestion went on to launch the entire field of *quantum computing*.

1.1.2 DiVincenzo Criteria

In 1985, Deutsch first described a set of properties that a universal quantum computer should possess.[46] In 2000, DiVincenzo expanded and formalized these requirements and proposed a set of 5+2 criteria necessary for the physical realisation of a quantum computer [49]. The two supplementary conditions concern the implementation of quantum communication. The seven criteria as presented by DiVincenzo [49] are the following:

1. **A scalable physical system with well-characterized qubits.**

   Well-characterized qubits imply well-defined two-level quantum systems ($|0\rangle$ and $|1\rangle$) with known dynamics and a good description of the coupling to other degrees of freedom. If a qubit has the capacity to access more than two levels, the probability of the system going to these higher states should be small. Scalability requires that the general state of a many-qubit system composed of N qubits span the entire 2^N-dimensional complex vector space. That is to say that multiple qubits can become entangled and their combined Hilbert space cannot be written as a product of individual states.

2. **The ability to initialise the state of the qubits to a simple fiducial state.**

Before starting the quantum computation, the system should be set to a simple initial state such as $|000...0\rangle$. This fiducial, or reference state, must be known before manipulating the system for computation. One way to obtain a simple initial state is to let the system evolve naturally and have it cool down to the Hamiltonian ground state. Another approach for initialising electron-spin qubits is to place them in a strong magnetic field forcing them to align with it. More techniques and their advantages are described further in the following references: [49, 159, 140, 106, 84].

3. **Long relevant decoherence times, much longer than the gate operation time.**

   The dynamics of a qubit in contact with its environment, or decoherence, must be limited in comparison to the time taken by a computational gate to act on the qubit. Simply put, the decoherence time is the time taken by a system in a state $|\psi\rangle = a|0\rangle + b|1\rangle$ to transform into the mixed state $\rho = |a|^2 |0\rangle\langle 0| + |b|^2 |1\rangle\langle 1|$. The use of error correcting codes can lessen the effect of decoherence but the decoherence times must remain long compared to the gate operation time.

4. **A "universal" set of quantum gates.**

   A quantum computer should be programmable in that algorithms should be implemented in a controllable and reliable way. Similar to a classical computer, where computational operations are executed by a set of logic gates, a quantum computer must be operated using new quantum gates. It has been shown that a set of single-qubit gates performing unitary operations on the quantum state, such as the Hadamard gate, and two-qubit entangling gates, such as the CNOT, CPHASE, or root-of-SWAP gates, set sequentially are sufficient to implement any quantum algorithm [11, 48].

5. **A qubit-specific measurement capability.**

   The readout process is essential to any quantum computer if the result of a computation is to be known. As such, it must be possible to measure the state of each qubit output from the computer. Although the best reliability is desirable, a perfect efficiency in readout operations is not a requirement for quantum computers. In the case of sub-100% efficiency, multiple computations can be performed to increase the reliability of the result.

6. **The ability to interconvert stationary and flying qubits.**

   For quantum computers to communicate with other quantum information systems, there must exist a quantum channel along which quantum information can be transmitted. The computer must be able to convert quantum information from stationary qubits

executing the computation to flying qubits. Flying qubits are simply defined as moving qubits; these are typically photon qubits but can also be moving electron-charge qubits or electron-spin qubits.

7. **The ability faithfully to transmit flying qubits between specified locations.**

   For tasks like quantum cryptography, only requirement 7 of the two extra requirements is sufficient since flying qubits can be created and detected directly.

Although each of these criteria must be considered and addressed, the main focus of this thesis will be on the 4^{th} and the 6^{th} requirements.

1.1.3 Bloch Sphere Representation

The state of a qubit is represented as a superposition of two basis states $\{|0\rangle, |1\rangle\}$

$$|\psi\rangle = \alpha|0\rangle + \beta|1\rangle \tag{1.1}$$

where α and β are complex constants with unit normalization imposing that

$$|\alpha|^2 + |\beta|^2 = 1. \tag{1.2}$$

A convenient geometrical representation of the qubit state space known as the Bloch sphere provides a simple visualization of two-level pure states. The wave function of the qubit is rewritten as

$$|\psi\rangle = \cos\left(\frac{\theta}{2}\right)|0\rangle + e^{i\phi}\sin\left(\frac{\theta}{2}\right)|1\rangle \tag{1.3}$$

where the polar angle θ ranges from $0 \leq \theta \leq \pi$ and the azimuthal angle ϕ ranges from $0 \leq \phi \leq 2\pi$ and the basis states $|0\rangle$ and $|1\rangle$ are respectively located at the north and south poles of the sphere. A graphical representation of the Bloch sphere is shown in Figure 1.2.

The Bloch sphere is particularly useful for representing a state changed by a single-qubit unitary operation. It can be shown that any unitary operation on a pure state (ignoring global phase changes) can be represented as a rotation on the Bloch sphere.

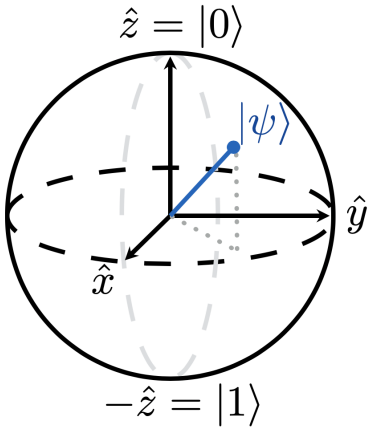

Fig. 1.2 Graphical representation of a given pure state $|\psi\rangle$ on the surface of the Bloch sphere.

1.2 Semiconductor Devices

There are many physical systems capable of forming qubits such as superconductors, ion traps, optical devices and semiconductor devices. My research is focused on semiconductor devices, which integrate well with current technology and are part of a mature industry. When opting for semiconductor based quantum computers, an important consideration is the wealth of knowledge and the expertise available on the properties and fabrication techniques of semiconductors. The ubiquity of semiconducting materials in almost all of modern electronics has pushed the industry to optimize their fabrication. Manufacturing techniques offer the possibility of relatively inexpensive development of quantum computing and quantum communication technologies and the existing knowledge base indicates a viable scalability from a few to many qubits.

The materials studied in this research project are gallium arsenide (GaAs) and aluminium gallium arsenide ($Al_xGa_{1-x}As$) as crystals arranged in a layered heterostructure. The difference in band gap of GaAs and AlGaAs forces electrons to be confined in a two-dimensional electron gas (2DEG) at the interface between the two materials. Metallic gates at the surface of the device can generate electric fields which deplete certain regions of the quantum well located in a thin layer of GaAs.

A defining property of gallium arsenide as opposed to silicon is its piezoelectric nature. The piezoelectric effect is the modulation of electric charge in a material due to an applied mechanical stress. A piezoelectric potential can be generated in several materials including semiconductor crystals of the group III-V such as GaAs. Section 1.3 describes how a propagating sinusoidal stress wave can create an electric potential with the ability to carry electrons at a constant and reliable rate.

1.2.1 Crystal Structures

In this section, I will give a brief overview of crystal structures with a focus on gallium arsenide crystals. The scope of the work in this thesis does not cover crystal sturctures in depth, but it is important to understand the origin of certain values for the parameters used in my simulations.

In atoms, electrons are distributed among orbital shells and subshells around the nucleus. Electrons are indistinguishable particles and carry the same charge and base mass, however, when structured in an atom, they will have different levels of energy. These electrons are arranged in subshells labelled s, p, d, and f. Each subshell contains an odd number of orbitals and twice that amount of electrons allowed per shell. This doubling is to allow both electron spins to exist in the same orbital.

$s \rightarrow$ 1 orbital (2 electrons maximum)

$p \rightarrow$ 3 orbitals (6 electrons maximum)

$d \rightarrow$ 5 orbitals (10 electrons maximum)

$f \rightarrow$ 7 orbitals (14 electrons maximum)

In this thesis, most of the work involves gallium arsenide semiconductors. The electron configuration of these elements is:

Ga (31 electrons): $1s^2 2s^2 2p^6 3s^2 3p^6 3d^{10} 4s^2 4p^1$

As (33 electrons): $1s^2 2s^2 2p^6 3s^2 3p^6 3d^{10} 4s^2 4p^3$

where the subshells identified in blue correspond to the core electrons and those colored red correspond to the valence electrons. The number preceding the shell label keeps track of the number of shells in the atom. The exponent indicates the number of electrons in that particular subshell. In the case of GaAs, electrons with principal number 4 are the outermost (valence) electrons. Figure 1.3 illustrated the shape of the s and p orbitals. The tetrahedral structure of GaAs, formed by one s orbital and three p orbitals causes the atoms to become sp^3 hybridised. A linear combination of the s and p orbitals generates four sp^3 orbitals:

$$
\begin{aligned}
\psi_1^{sp^3} &= \frac{1}{2}(\psi^s + \psi^{px} + \psi^{py} + \psi^{pz}), \\
\psi_2^{sp^3} &= \frac{1}{2}(\psi^s + \psi^{px} - \psi^{py} - \psi^{pz}), \\
\psi_3^{sp^3} &= \frac{1}{2}(\psi^s - \psi^{px} - \psi^{py} + \psi^{pz}), \\
\psi_4^{sp^3} &= \frac{1}{2}(\psi^s - \psi^{px} + \psi^{py} - \psi^{pz}).
\end{aligned} \tag{1.4}
$$

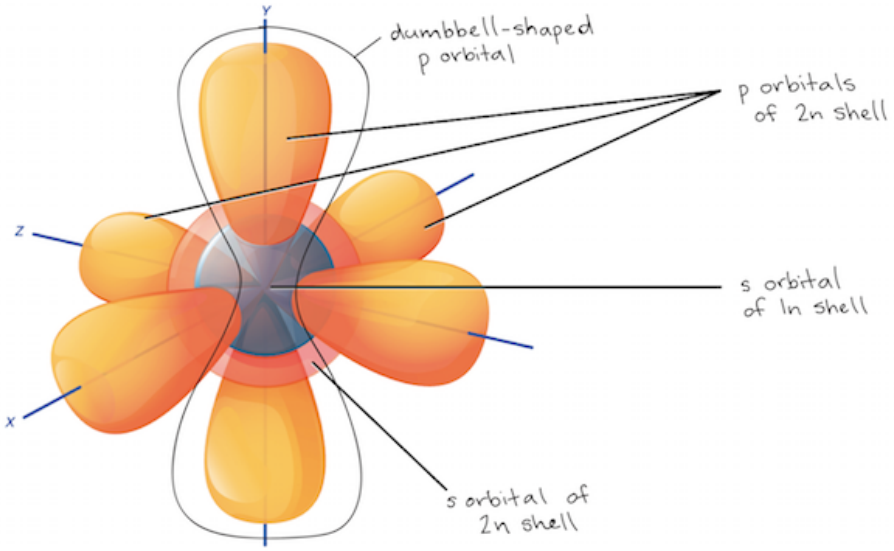

Fig. 1.3 Illustration of the first *s* and *p* electron subshells. Image taken with permission from Khan Academy.[90]

A Bravais lattice is defined as an infinite arrangement of discrete points – or lattice sites – that follow a set of regular translations in a vector space. The lattice is unchanged by any translation vector given by

$$
\vec{T}_{mno} = m\vec{a_1} + n\vec{a_2} + o\vec{a_3} \quad m,n,o \in \mathbb{Z} \tag{1.5}
$$

where $\vec{a_1}$, $\vec{a_2}$, and $\vec{a_3}$ are primitive translation vectors that define the unit cell.

In a GaAs crystal, Ga atoms are anions (negatively charged) and As atoms are cations (positively charged). The crystal structure of GaAs is called zincblende, a face-centered cubic (FCC) structure. An illustration of the zincblende unit cell is shown in Fig. 1.4.

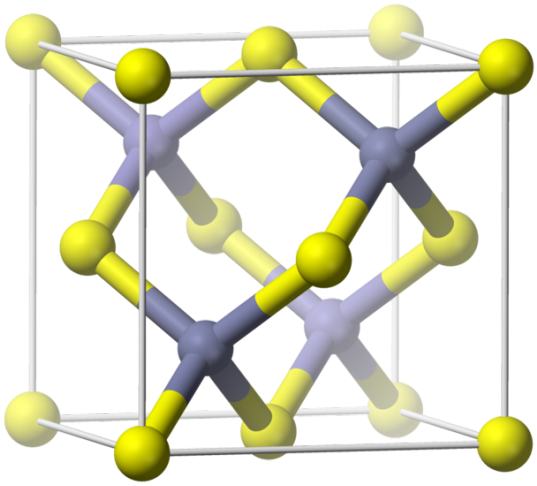

Fig. 1.4 Zincblende unit cell. Anions (Ga) are illustrated in yellow and cations (As) are grey. There are eight atoms in this unit cell. The four anions are divided into $8 \times 1/8$ corner atoms and $6 \times 1/2$ face atoms. The individual cations are located at the front bottom left, back bottom right, front top right, and back top left. Public domain image taken from Wikipedia[163].

1.2.2 GaAs Band Structure

Finding the wave function of a many-particle system scales exponentially with the number of particles. For large lattice structures, the electronic band structure can be approximated using the tight-binding model [36]. In this method, electrons in the conduction band are delocalised and are approximated as free electrons. Electrons in the valence band are "tightly bound" to the atom to which they belong.

Considering one unit cell for GaAs, the eight s and p orbitals define the bands of the zincblende structure. The Hamiltonian for these eight states is given by

	$\|\phi_{s1}\rangle$	$\|\phi_{px1}\rangle$	$\|\phi_{py1}\rangle$	$\|\phi_{pz1}\rangle$	$\|\phi_{s2}\rangle$	$\|\phi_{px2}\rangle$	$\|\phi_{py2}\rangle$	$\|\phi_{pz2}\rangle$
$\|\phi_{s1}\rangle$	E_{s1}	0	0	0	$V_{ss}g_1$	$V_{sp}g_2$	$V_{sp}g_3$	$V_{sp}g_4$
$\|\phi_{px1}\rangle$	0	E_{p1}	0	0	$-V_{sp}g_2$	$V_{xx}g_1$	$V_{xy}g_4$	$V_{xy}g_3$
$\|\phi_{py1}\rangle$	0	0	E_{p1}	0	$-V_{sp}g_3$	$V_{xy}g_4$	$V_{xx}g_1$	$V_{xy}g_2$
$\|\phi_{pz1}\rangle$	0	0	0	E_{p1}	$-V_{sp}g_4$	$V_{xy}g_3$	$V_{xy}g_2$	$V_{xx}g_1$
$\|\phi_{s2}\rangle$	$V_{ss}g_1^*$	$-V_{sp}g_2^*$	$-V_{sp}g_3^*$	$-V_{sp}g_4^*$	E_{s2}	0	0	0
$\|\phi_{px2}\rangle$	$V_{sp}g_2^*$	$V_{xx}g_1^*$	$V_{xy}g_4^*$	$V_{xy}g_3^*$	0	E_{p2}	0	0
$\|\phi_{py2}\rangle$	$V_{sp}g_3^*$	$V_{xy}g_4^*$	$V_{xx}g_1^*$	$V_{xy}g_2^*$	0	0	E_{p2}	0
$\|\phi_{pz2}\rangle$	$V_{sp}g_4^*$	$V_{xy}g_3^*$	$V_{xy}g_2^*$	$V_{xx}g_1^*$	0	0	0	E_{p2}

where E_s and E_p correspond to the energy of the s and p states, V is a molecular orbital overlap parameter, and g is a parameter defined by the position of the atoms within the GaAs unit cell. Solving the eigenvalue problem for this Hamiltonian gives the eigenvalues at a given point k of the wave vector. Figure 1.5 shows the energy bands of GaAs along high symmetry lines of the zincblende structure.

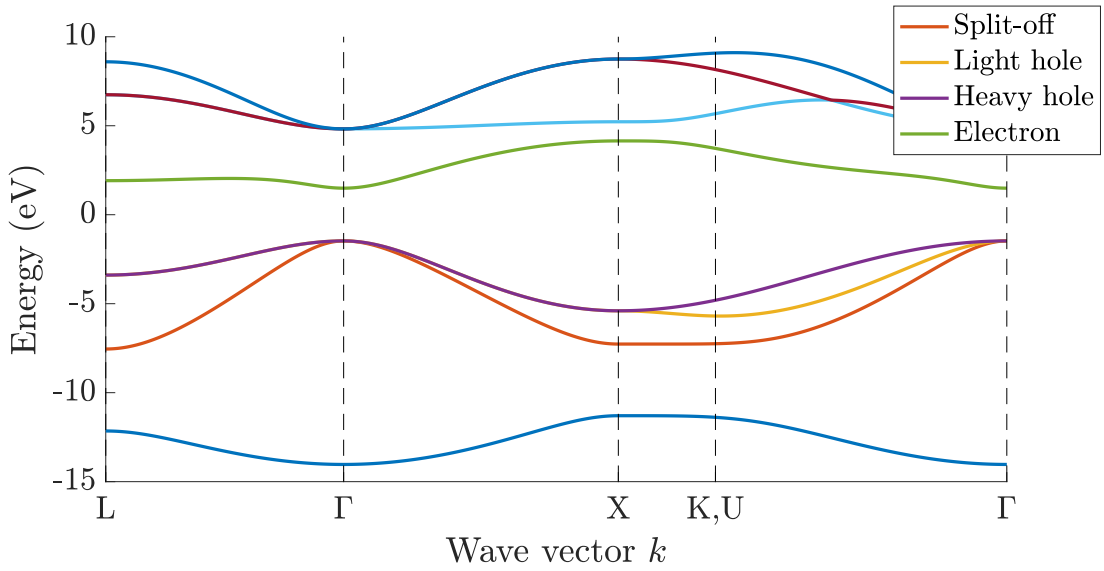

Fig. 1.5 GaAs band structure. All eight energy bands are ploted along high symmetry lines of the Brillouin zone. Only the bands relevant to calculating the effective electron and hole mass have been labeled.

For free electrons, the curvature of the energy $\mathscr{E}$ is determined by the wave vector k as

$$\mathscr{E} = \frac{\hbar^2 k^2}{2m}, \tag{1.6}$$

where m is the mass of an electron. Differentiating Eq. 1.6 with respect to k twice, defines the effective mass m^* as a function of $\mathscr{E}$.

$$\frac{1}{m^*} = \frac{1}{\hbar^2}\frac{d^2\mathscr{E}}{dk^2}. \tag{1.7}$$

Focussing on a number of k points near the Γ point (the centre of the Brillouin zone), the values of energy can be fit using a quadratic polynomial. The results can be used to find $\mathscr{E}$ and therefore deduce the effective mass of the particle m^* [92]. In this work, the effective mass for single electrons in GaAs devices is $m_e^* = 0.067m_e$ where m_e is the mass of an electron in free space.

1.3 Surface Acoustic Waves

Surface acoustic waves (SAWs) were first described by Lord Rayleigh in 1885 and often bear the name Rayleigh waves. They consist of acoustic modes propagating along the surface of an elastic material. The amplitude of a SAW typically decays exponentially with depth into the bulk. Figure 1.6 illustrates the different types of acoustic waves and their associated distortion patterns in a material. Rayleigh waves are made up of a longitudinal propagation as well as a vertical sheer component. The resulting motion for particles in the material is a retrograde elliptical path. Mechanical strain applied to a piezoelectric material triggers an accumulation of charge [44] so a periodic surface acoustic wave can be accompanied by a propagating periodic electric potential.

The modulation of an electric potential in a layered semiconductor substrate can be used to create a new dimension of confinement for electrons in the conduction band. Since the sinusoidal potential is propagating, electrons are trapped in moving quantum dots. By tuning the amplitude of the SAW, it has been shown that the number of electrons per minimum can be carefully controlled and single electron transport is achieved.[86, 111, 79]

In 2011, McNeil *et al.* demonstrated that a single electron in GaAs could be carried reliably by a surface acoustic wave back and forth across a depleted channel several times and that the same electron could travel a cumulative distance of over 0.25mm without error.[111] A reliable control of electrons over large distances is crucial for transporting qubits between corresponding parts of a quantum circuit that are not in neighbouring quantum dots.[111, 12]

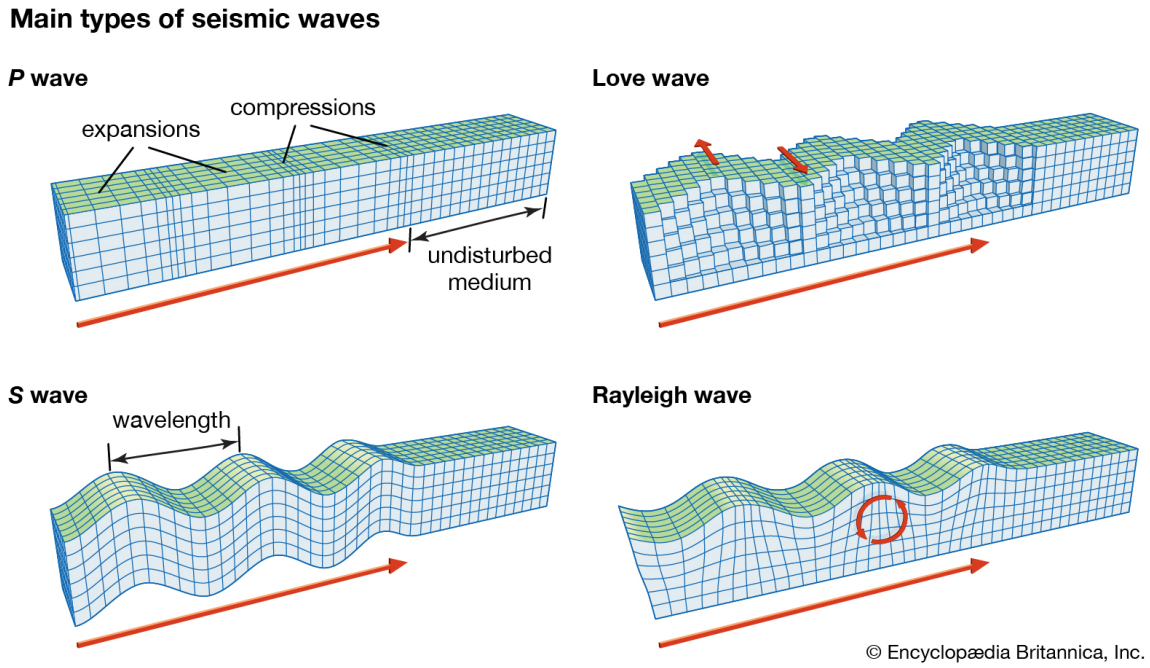

Fig. 1.6 Different Types of seismic waves. P-type and S-type waves are longitudinal and transverse waves respectively. Love waves and Rayleigh waves are surface acoustic waves where the motion of particles follows a different pattern. The surface acoustic waves used in this study are Rayleigh waves. Image taken with permission from Encyclopedia Britannica.[120]

In 2000, Barnes *et al.* proposed a scheme that uses SAW-based devices as quantum processors where single electrons trapped in the SAW minima act as spin or charge qubits [12]. A schematic of single and two qubit operations in a SAW-based quantum computation scheme can be seen in Figure 1.7. Here, magnetic split gates act as single qubit gates and two qubit gates are achieved by bringing together adjacent channels thus allowing qubits to interact via a tunnelling barrier. As stated by the DiVincenzo criteria discussed in Sec. 1.1.2, a series of single- and two-qubit operations are sufficient to construct a universal quantum computer. The propagation speed of a surface acoustic wave in GaAs is approximately 2800m/s and a SAW-driven device typically operates at a frequency of ∼3GHz, allowing a SAW-based quantum processor to perform operations billions of times per second.

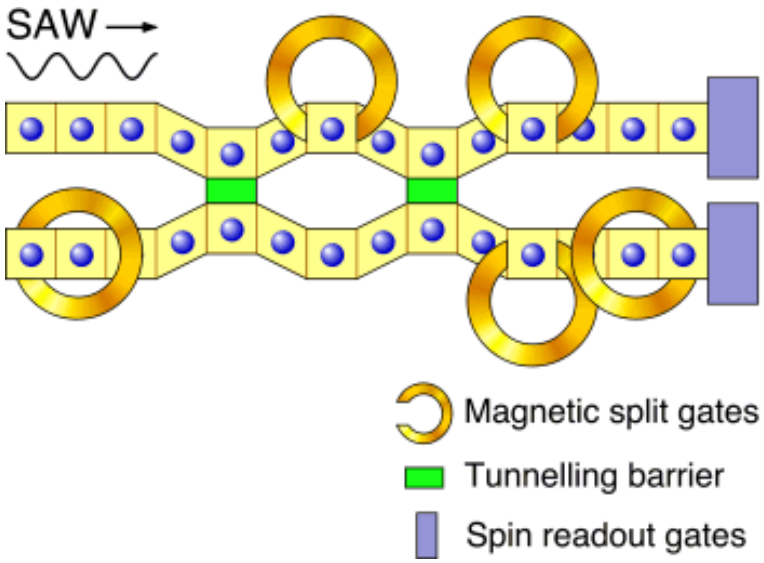

Fig. 1.7 Example quantum circuit based on the surface acoustic wave quantum computer [139].

In GaAs, surface acoustic waves are generated via a radio frequency alternating current applied to interdigital transducers (IDTs). IDTs are interlocked metallic electrodes deposited on the surface of the substrate. When an alternating current is applied to one set of fingers while the other set is grounded, a periodic propagating strain wave is generated at the surface of the piezoelectric material. A diagram of SAW generation from IDTs can be seen in Fig. 1.8.

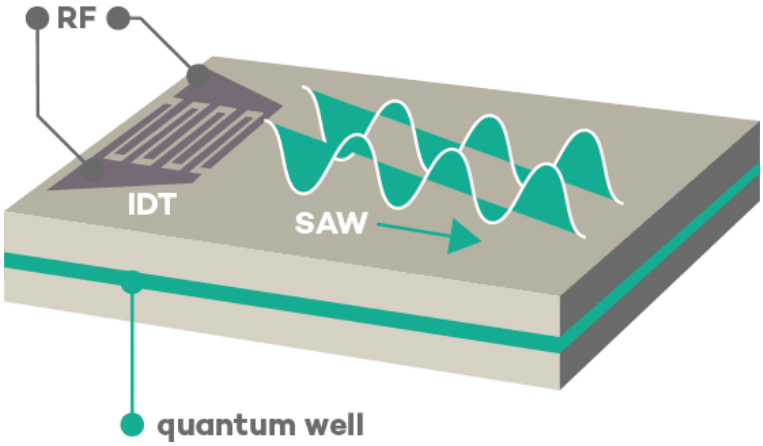

Fig. 1.8 Surface acoustic waves are generated by electrically modulating interdigitated transducers (IDT) using radio frequency (RF) currents and propagate along a semiconductor device. Image taken with permission of the SAWtrain network [133].

1.4 Outline

In this chapter, I presented the motivation for studying quantum-information systems. I discussed how the scalable physical implementation of qubits in a material whose fabrication techniques are well known and part of a mature industry is paramount for the realistic development of a quantum computer. I introduced the key concepts needed to study semiconductor systems and described the way in which surface acoustic waves can be used to physically carry single-electron qubits across a device. In the rest of my thesis, I present a comprehensive study on the use of single electrons as qubits for a quantum computer. My results describe the manipulation of quantum information including the optimal definition of a qubit, single-qubit operations and two-qubit entanglement generation.

In Chapter 2, I introduce the numerical methods available for solving physical problems on current classical computation systems. I compare various discretisation methods for making the quantum evolution problem finite and the limitations of each method. I then go on to explore the use of graphics processing units (GPUs) to parallelise the solutions to the differential equations and accelerate computation times. I provide a comparison to traditional computation methods and discuss the different hardware and software solutions currently available.

In Chapter 3, I describe the two-level system used to define a quantum bit. Here, the spatial state of a single electron is mapped to the Bloch Sphere. I show a method for changing the state of a qubit through the application of rapid electric pulses. I describe the experimental shortcomings of electric pulse generation and how these can be overcome by shaping the

pulses differently. This chapter provides the theoretical tools for single qubit manipulation, satisfying one part of the universal set of quantum gates required by the DiVincenzo criteria.

In Chapter 4, I apply my single qubit simulations to modelling real semiconductor devices. This chapter includes work done in collaboration with Dr. Hermann Edlbauer and Dr. Christopher Bäuerle from the Intitut Néel, Centre national de la recherche scientifique (CNRS) in France. While the researchers at the CNRS fabricated and measured the semiconductor device, I provide the theoretical foundations and the numerical results that accurately describe the behaviour of this device. By modelling the single-electron transport process, I pinpoint the sources of excitation that introduce unwanted errors in the quantum state of the electron. By running parameter sweeps, I uncover ways to minimize excitations and ensure a high-fidelity device.

Moving beyond what is currently realisable experimentally, I present a framework for general quantum measurements in Chapter 5. Inspired by the technology presented in Chapter 4, I designed a circuit capable of realising a positive-operator-valued measure (POVM), a generalisaion of projective measurements. I present a comparison of this circuit with current POVM implementations in photonic systems. Once again, I strive to keep realistic parameters and experimental applicability in mind. In this chapter, I identify the main challenges when using electrons instead of photons for a POVM device and I provide readily available solutions to those challenges.

In Chapter 6, I formulate an entanglement generation scheme based on the exchange interaction. I present two-dimensional two-particle simulations that push my state-of-the-art GPUs to their limit. This chapter is once more aimed at the experimental implementation of quantum operations. Using realistic device parameters, I simulate the root-of-SWAP operation – a maximally entangling operation – performed using different methods. I outline the benefits and disadvantages of each method and advocate the use of current experimental devices to carry out the two-qubit gate operation.

Finally, in Chapter 7, I lay out the future development plans for my quantum simulations. This further work is a collection of ideas that I had during my PhD but did not have time to complete as well as suggestions from colleagues and fellow researchers during conferences and collaborative work. Both the development of new software features and the implementation of the code on novel hardware platforms can make for interesting and exciting PhD projects.

2

NUMERICAL METHODS

The quantum systems I study in this thesis are dynamical in nature, meaning the state of a system goes through a time evolution and is changed into a different state. The partial differential equation describing the non-relativistic evolution of a quantum system is the time dependent Schrödinger equation and is given by

$$i\hbar\frac{\partial\psi(t)}{\partial t} = \hat{H}\psi(t) \tag{2.1}$$

where $\psi(t)$ is the wave function for an arbitrary quantum system of one or many particles and $\hat{H}$ is the Hamiltonian of the quantum system. The formal solution to Equation 2.1 is given by

$$\psi\left(t'\right) = \hat{U}\left(t',t\right)\psi(t) \tag{2.2}$$

for an initial state $\psi(t)$ and a final state $\psi(t')$. The time evolution operator $\hat{U}(t',t)$ is described by

$$\hat{U}\left(t',t\right) = \mathscr{T}\ \exp\left(-\frac{i}{\hbar}\int_t^{t'}\hat{H}(\tau)\mathrm{d}\tau\right) \tag{2.3}$$

where $\mathscr{T}$ provides time ordering. Analytic solutions to equation 2.3 only exist for a few simple cases and the time evolution operator is, in general, difficult to solve. Since the

systems we are interested in are complex, I rely on numerical solutions to study their time evolution.

Computers operate using finite computational resources such as memory, storage space, transfer bandwidths, and processing speeds. It is therefore necessary to discretise the simulated system both in space and in time. In my work, I used the finite difference method for spatial discretisation and the *staggered leapfrog* method for temporal discretisation. This method is advantageous since it is parallelisable, which allows hardware acceleration through the use of parallel-processing capabilities of graphical processing units.

2.1 Discretisation Methods

No current system is capable of simulating the time evolution of continuous physical systems numerically. Time-evolution problems must therefore be discretised in both time and space. In this section, I discuss various discretisation methods and argue for the use of the finite-difference method for spatial discretisation and the staggered leapfrog method for temporal discretisation as these methods offer a good balance between computational efficiency, speed, and accuracy.

2.1.1 Spatial Discretisation

The finite difference method limits the wave function to an ordered, real, lattice space. Let us consider the example of a single particle. The Hamiltonian of a single spinless particle in one dimension is given by

$$\hat{H}\psi(x) = \left(-\frac{\hbar^2}{2m^*}\frac{\partial^2}{\partial x^2} + V(x)\right)\psi(x) = E\psi(x), \tag{2.4}$$

where m^* is the effective mass of the particle and $V(x)$ is the external potential function. To find $\hat{H}\psi(x)$ numerically, we can discretize the wave function and use the Taylor expansion to find its derivatives. The Taylor expansion of the wave function is given by

$$\psi(x+\Delta x) = \psi(x) + \frac{\partial\psi(x)}{\partial x}\Delta x + \frac{\partial^2\psi(x)}{\partial x^2}\frac{\Delta x^2}{2} + \frac{\partial^3\psi(x)}{\partial x^3}\frac{\Delta x^3}{3!} + \ldots \tag{2.5}$$

and

$$\psi(x-\Delta x) = \psi(x) - \frac{\partial\psi(x)}{\partial x}\Delta x + \frac{\partial^2\psi(x)}{\partial x^2}\frac{\Delta x^2}{2} - \frac{\partial^3\psi(x)}{\partial x^3}\frac{\Delta x^3}{3!} + \ldots \tag{2.6}$$

Adding Eq. 2.5 and Eq. 2.6 and rearranging the terms, we obtain an expression for the second order spatial derivative of the wave function:

$$\frac{\partial^2 \psi(x)}{\partial x^2} = \frac{\psi(x+\Delta x) - 2\psi(x) + \psi(x-\Delta x)}{\Delta x^2} + \mathscr{O}\left(\Delta x^2\right). \tag{2.7}$$

Substituting Eq. 2.7 into the time-independent Schrödinger equation (TISE) and using a discretised wave function, we get

$$\left(-\frac{\hbar^2}{2m^*\Delta x^2}\right)(\psi_{n+1} - 2\psi_n + \psi_{n-1}) + V_n\psi_n = E\psi_n, \tag{2.8}$$

where n is an index of the position lattice. This equation can be expressed as a matrix from which the eigenvalues and eigenvectors can be found numerically. This eigenvalue decomposition problem is represented by

$$\begin{pmatrix} V_1+a & b & & & \\ b & V_2+a & b & & \\ & b & V_3+a & \ddots & \\ & & \ddots & \ddots & \\ & & & & \end{pmatrix} \begin{pmatrix} \psi_1 \\ \psi_2 \\ \vdots \\ \psi_n \\ \vdots \\ \psi_N \end{pmatrix} = \begin{pmatrix} \varepsilon_1 \\ \varepsilon \\ \vdots \\ \varepsilon_n \\ \vdots \\ \varepsilon_N \end{pmatrix}, \tag{2.9}$$

where

$$a = \frac{\hbar^2}{m^*\Delta x^2} \qquad \text{and} \qquad b = -\frac{\hbar^2}{2m^*\Delta x^2}$$

and where ε_n corresponds to the eigen energy associated to the eigen vector ψ_n.

The diagonalisation of the tri-diagonal matrix in Eq. 2.9 allows us to find the eigenvalues and eigenfunctions of a given 1D system. The same methodology can be applied to higher-dimensional or multi-particle systems. In such cases, the complexity of the matrix from Eq. 2.9 increases. Each additional dimension or particle adds non-zero diagonals to the Hamiltonian. Solving the TISE eigenvalue problem is useful for finding the initial state of a wave function. As the complexity of the system increases or as the lattice becomes larger, it may be too computationally demanding to solve the matrix diagonalisation directly. Under certain circumstances, it is possible to reduce the size of the matrix by solving the eigenvalue problem in momentum-space instead of real-space. This matrix is not sparse and, if the system is near its ground state, only a few momentum modes contribute to the wave function.

The final aspect to consider in the discretisation of the Hamiltonian is the boundary conditions imposed on the edges of the simulation space. A detailed description of the different type of boundary conditions used in this work is provided in Sec. 2.3.

2.1.2 Temporal Discretisation

The most commonly known temporal discretisation method is the Euler method, which uses the first term of the Taylor expansion as a linear approximation to the solution for small time steps [34]. Equation 2.3 is solved, which is unconditionally divergent under the Euler method. Increasing the number of terms used in the Taylor expansion helps the approximation approach the solution but rapidly becomes computationally demanding.

The Crank-Nicolson method offers a stable and norm-preserving approximation to Eq. 2.3 by applying a Cayley transformation to the exponential [43]. Although the Crank-Nicolson method is unconditionally stable [151], it does not provide an explicit solution to $\hat{U}(t',t)$ and requires a matrix inversion of the Hamiltonian at every time step. While there exist many algorithms specifically written to handle matrix inversions, this process can be extremely slow for large Hamiltonians.

Maestri *et al.* proposed a method that involves taking a pair of Taylor expansions at different time steps and subtracting them [107]. This method is not unconditionally stable but offers an explicit solution to Eq. 2.3 and produces accurate results for small values of Δt. Here, I present a revised derivation of the staggered leapfrog numerical method for two spinless particles in one dimension. Starting with the two-particle time-dependent Schrödinger equation and using natural units ($\hbar = c = m_e = 1$) we have

$$i\frac{\partial}{\partial t}\psi(x_1,x_2,t) = \hat{H}\psi(x_1,x_2,t) = \left(-\frac{1}{2m_1}\frac{\partial^2}{\partial x_1^2} - \frac{1}{2m_2}\frac{\partial^2}{\partial x_2^2} + V(x_1,x_2)\right)\psi(x_1,x_2,t), \tag{2.10}$$

where m_1 and m_2 are the masses of both particles 1 and 2 respectively. Using the finite difference method presented in Sec. 2.1.1, the wave function is dicretized spatially. The discrete wave function is defined as

$$\psi(x_1,x_2,t) = \psi(r\Delta x_1, s\Delta x_2, n\Delta t) \equiv \psi^n_{r,s} \qquad \forall (r,s,n) \in \mathbb{Z}, \tag{2.11}$$

where r and s are spatial indices for particles 1 and 2 and n is the discrete time index. Plugging Equation 2.11 into Equation 2.10 yields

$$\hat{H}\psi = -\frac{1}{2m_1}\left(\frac{\psi_{r+1,s} - 2\psi_{r,s} + \psi_{r-1,s}}{\Delta x_1^2}\right) - \frac{1}{2m_2}\left(\frac{\psi_{r,s+1} - 2\psi_{r,s} + \psi_{r,s-1}}{\Delta x_2^2}\right) + V_{r,s}\psi_{r,s}. \tag{2.12}$$

For the purpose of simplicity, let us assume that the lattice spacing is defined equally for both particles, i.e. $\Delta x_1 = \Delta x_2 = \Delta x$. Time dependence can now be added to the system. When deriving the staggered leapfrog method, it is important to consider the two previous

time steps of the system's time evolution. As will be discussed later in this section, the wave function can be split into its real and imaginary components and each part of the wave function is solved for every other time step. The real and imaginary components are evaluated at different (staggered) time steps sequentially and "leapfrog" each other. The time evolution of the wave function is described by

$$\psi_{r,s}^{(n+1)} - \psi_{r,s}^{(n-1)} = \left(e^{-i\Delta t H} - e^{i\Delta t H}\right)\psi_{r,s}^{n} = -2i\Delta t H \psi_{r,s}^{n} + \mathscr{O}\left(\Delta t^2\right). \tag{2.13}$$

Keeping only the leading non zero-term of the Taylor expansion in Eq. 2.13 and replacing the Hamiltonian by the expression in Eq. 2.12 we get

$$\begin{aligned}\psi_{r,s}^{(n+1)} = \psi_{r,s}^{(n-1)} - 2i\Bigg\{ &\left[\left(\frac{1}{m_1}+\frac{1}{m_2}\right)\frac{\Delta t}{\Delta x^2} + \Delta t V_{r,s}\right]\psi_{r,s}^{n} \\ &- \frac{1}{2}\frac{\Delta t}{\Delta x^2}\left[\frac{1}{m_1}\left(\psi_{r+1,s}+\psi_{r-1,s}\right)+\frac{1}{m_2}\left(\psi_{r,s+1}+\psi_{r,s-1}\right)\right]\Bigg\}.\end{aligned} \tag{2.14}$$

It is now possible to separate the wave function into its real and imaginary parts:

$$\psi_{r,s}^{n} = u_{r,s}^{n} + i\, v_{r,s}^{n}. \tag{2.15}$$

The real and imaginary components of Equation 2.14 are

$$u_{r,s}^{n+1} = u_{r,s}^{n-1} + 2\left\{\left[\left(\frac{1}{m_1}+\frac{1}{m_2}\right)\lambda + \Delta t V_{r,s}\right] v_{r,s}^{n} - \frac{1}{2}\lambda\left[\frac{1}{m_1}\left(v_{r+1,s}^{n}+v_{r-1,s}^{n}\right)+\frac{1}{m_2}\left(v_{r,s+1}^{n}+v_{r,s-1}^{n}\right)\right]\right\} \tag{2.16a}$$

$$v_{r,s}^{n+1} = v_{r,s}^{n-1} - 2\left\{\left[\left(\frac{1}{m_1}+\frac{1}{m_2}\right)\lambda + \Delta t V_{r,s}\right] u_{r,s}^{n} - \frac{1}{2}\lambda\left[\frac{1}{m_1}\left(u_{r+1,s}^{n}+u_{r-1,s}^{n}\right)+\frac{1}{m_2}\left(u_{r,s+1}^{n}+u_{r,s-1}^{n}\right)\right]\right\} \tag{2.16b}$$

Evaluated at staggered times of one half time step, both real and imaginary components of the wave function are represented by

$$\left[u_{r,s}^{n}\ ,\ v_{r,s}^{n}\right] = \left[\mathrm{Re}\psi\left(x,t\right)\ ,\ \mathrm{Im}\psi\left(x,t+\tfrac{1}{2}\Delta t\right)\right]. \tag{2.17}$$

Assuming a sufficiently small time step Δt, the minor time discrepancy $\frac{1}{2}\Delta t$ can be ignored and both parts of the wave function are combined to obtain the new wave function after time

evolution. The staggered leapfrog method is not unconditionally convergent and must satisfy the stability criterion

$$\Delta t < \frac{\hbar}{\left(\frac{\hbar^2}{m}\right)\left(\frac{1}{\Delta x^2}+\frac{1}{\Delta y^2}+\frac{1}{\Delta z^2}\right)+V_{\max}} \tag{2.18}$$

for each particle, where $V_{\max}$ is the maximum value of the potential. As a result, the norm of the wave function is not strictly conserved, in general. To make sure the solutions calculated by my solver did not diverge significantly, I monitored the norm at every time step. Deviations from unity for the simulations presented in this work were usually on the order of 0.1% or less.

2.2 Potential Layout and Initial Eigenstates

One of the biggest challenges when solving quantum-mechanical problems is to ensure that the simulations reflect realistic experimental devices. The underlying electrostatic potential in Equations 2.4 and 2.10 must therefore be estimated accurately. In this thesis, I used two methods for calculating the underlying potential. For theoretical proposals such as those in Chapters 3 and 5, I used functional potentials. These functions can be coded directly into the time dependent solver and provide a more meaningful interpretation of the confinements required for certain quantum operations. By contrast, when simulating actual experimental devices such as the one fabricated by the CNRS [54, 149] and presented in Chapter 4, I used the commercial Poisson-Schrödinger solver NextNano++ [21].

2.2.1 Functional Potentials

Much of the work in this thesis consists of developing a theoretical framework for quantum operations on single-electron qubits. As such, it is a good idea to remain general and not force an implementation that is specific to a certain laboratory or fabrication method. Because of the historical expertise, with Prof. Crispin Barnes at the head of my research group, most of the examples presented here are related to flying electron qubits carried by surface acoustic waves in gallium arsenide heterostructures. However, the concepts developed here are applicable to other materials, such as silicon, and other qubit implementations such as static charge qubits, static spin qubits, topological insulator qubits, and many more.

The simulations in this thesis only consider electrons already in the conduction band. Therefore, we only require a one band Hamiltonian. A single function is enough to describe the electrostatic potential. For example, a double-quantum-dot potential can by described by

the sum of a harmonic potential and a Gaussian function,

$$V(x,y) = \frac{1}{2}m^*\omega_x^2 x^2 + \frac{1}{2}m^*\omega_y^2 y^2 + A_{\mathrm{TB}} m^* e^{-\frac{x^2}{2\sigma_{\mathrm{TB}}^2}}, \tag{2.19}$$

where ω_x and ω_y describe the amplitude of the parabolic confinement and A_{TB} and σ_{TB} characterise the amplitude and width of the Gaussian central barrier. Numerically, Eq. 2.19 is straightforward to implement and a sample of code is shown in Listing 2.1.

```
1 V = 0.5 * Mass1 * w2X * powf(x, 2.0) + 0.5 * Mass1 * w2Y * powf(y, 2.0)
2     + ATB1*Mass1*expf(-s2TB1*powf(x, 2.0) / 2.0)
3     + detuneX * Mass1 * x;
```

Listing 2.1 Double quantum dot functional potential from Eq. 2.19 implemented on the GPU CUDA kernel.

In Chapter 5, the spin of the electron was considered and two bands were used since the spin-up and spin-down configurations could experience different potentials. In this case, two different electric potentials and two magnetic potentials were defined.

2.3 Boundary Conditions

As with most finite-element solvers, this code requires boundary conditions to constrain the solutions of the differential equations to a finite domain. In most cases, we want to keep the non-zero parts of the wave function sufficiently far away from the edge of the simulation domain in order to avoid boundary effects introducing errors in the simulations. Since my goal is to simulate realistic devices, I must ensure that hard walls or wave-function leakage is not artificially introduced. In this work, I used three different types of boundary conditions. Dirichlet or “hard wall” boundaries were used most of the time since they are the most cost effective computationally and provide an easy way of identifying reflection errors. Absorbing boundary conditions were used when the wave function could escape the region of interest. In this scenario, the normalisation of the wave function was not preserved in an attempt to reduce the complexity of the simulation. The part of the electron outside the simulation domain is of no interest and its time evolution does not need to be fully solved quantum mechanically. Periodic boundaries are useful for simulating tubes or connected parts of a device on a 2D lattice. Although periodic boundary conditions are not presented directly in this thesis, they played an important role in the design of the measurement device presented in Chapter 5.

2.3.1 Dirichlet Boundary Conditions

By default, Dirichlet boundary conditions are used. These conditions specify that the wave function $\psi(x)$ takes a value of 0 on the boundary of the simulation domain Ω [39]. We require that

$$\psi(\boldsymbol{x}) = 0 \qquad \forall \boldsymbol{x} \in \partial\Omega, \tag{2.20}$$

where $\partial\Omega$ is the boundary of the domain. Numerically, this is simply implemented by setting the value of $\psi(\boldsymbol{x})$ to zero. GPU kernel code for a one-particle example in 3D is given by Listing 2.2.

```
1    if (i<0 || j<0 ||  k<0 )
2        return 0.0;
3    else if (i >= Nx || j >= Ny  || k >= Nz )
4        return 0.0;
5    else {
6        if (real)
7            return Psi[k + j*Nz + i*Nz*Ny].x;
8        else
9            return Psi[k + j*Nz + i*Nz*Ny].y;
10   }
```

Listing 2.2 Dirichlet boundary conditions implemented on the GPU CUDA kernel. The boundaries of the simulation domain are determined by the three dimensional indices x, y, and z range from 0 to Nx, Ny, and Nz respectively.

A visual example of a one-dimensional Gaussian wave packet interacting with a Dirichlet boundary is presented in Fig. 2.1. Here, the wave function $\psi(x)$ is initialised in the state

$$\psi(x) = \left(\frac{\omega}{\pi}\right)^{1/4} e^{-\frac{\omega x^2}{2}+ikx}, \tag{2.21}$$

in an infinite square potential well

$$V(x) = \begin{cases} 0 & -\frac{L}{2} < x < \frac{L}{2} \\ \infty & \text{otherwise.} \end{cases} \tag{2.22}$$

Since this simulation was done for illustration purposes only, the exact numerical values of the parameters are not important. We see from Figure 2.1 that non-zero parts of the wave function are reflected by the hard walls. The norm of the wave function is fully preserved at each time step of the simulation.

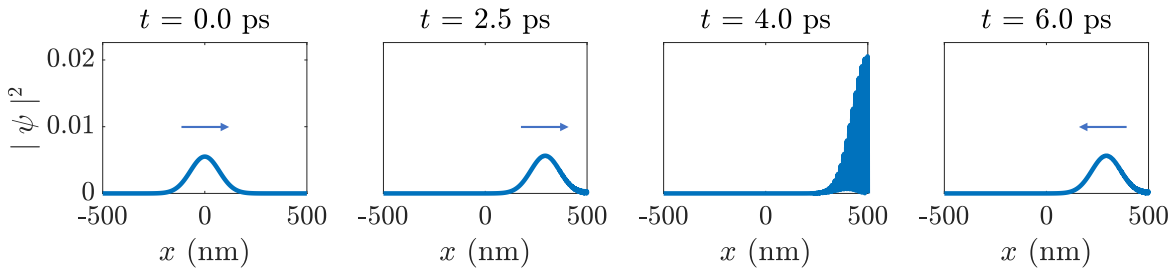

Fig. 2.1 A Gaussian wave packet is initialised in a 1D square well with initial momentum. As the wave function encounters the infinite wall, it is reflected. Self interference can be observed. Once the wave has fully reflected, it regains its original shape. The direction of motion of the wave function is indicated by a blue arrow.

When calculating the results presented in the later chapters of this thesis, I tailored the electrostatic potentials in order to avoid such reflections that would cause the electrons to exhibit an unphysical behaviour. To guarantee that at no point the particle was affected by the boundary conditions, I checked that the value wave function was zero (below floating point accuracy) for all lattice sites near the boundary. If at any point the values grew to be larger than numerical errors, the simulation was considered invalid and the domain was extended before solving the time-dependent Schrödinger equation (TDSE).

2.3.2 Absorbing Boundary Conditions

In some situations, the electron might be able to escape the confining potential defined by a semiconductor device or the surface acoustic wave. It is computationally impossible to simulate large spatial domains. In these situations, it might be favourable to use absorbing boundary conditions. We focus on the part of the wave function that is still in the region of interest, but we don't want parts of the wave to be reflected back into our simulation space. By using absorbing boundary conditions, it is possible to efficiently use computing power on the region of interest whilst simultaneously avoiding unphysical wave reflections introduced by Dirichlet boundary conditions. Here, we require that the derivative of the wave function $\psi(x)$ take on the value of 0 at the boundary of the simulation domain Ω. We have that

$$\frac{\partial \psi(x)}{\partial n} = 0 \qquad \forall x \in \partial\Omega, \tag{2.23}$$

where n is the unit vector normal to the boundary's surface.

One way to absorb a wave packet at the boundary is to use Von Neumann boundary conditions [137, 129, 57]. To implement Von Neumann boundary conditions, the wave is matched with one of equal velocity and opposite phase. The destructive interference cancels

the wave and only the parts that have not interacted with the boundary remain. This method can be complicated for arbitrary potentials since the wave function at the boundary is difficult to predict.

In this work, I used a method similar to references [138, 100, 165, 166, 117], where I let the particle evolve in imaginary time in an absorbing layer near the boundary. The Schrödiger equation becomes a simple diffusion equation and the wave function disappears without any reflections occurring. It is important to note that absorbing boundary conditions will not preserve the normalisation of the wave function and that, if these calculations are done numerically, renormalisation should not be introduced. Such a renormalisation would amplify numerical fluctuations and lead to erroneous results. Figure 2.2 illustrates a wave packet vanishing completely when crossing an absorbing boundary.

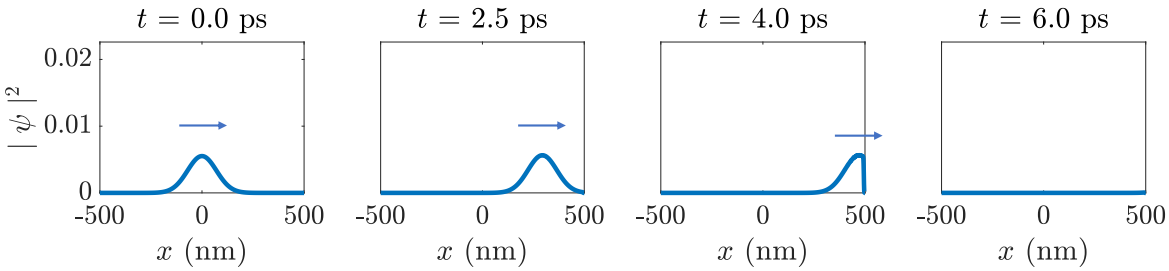

Fig. 2.2 A Gaussian wave packet is initialised in a 1D square well with initial momentum. The wave function passes through an absorbing region and its norm is no longer preserved. After some time, the entire wave function has left the simulation domain. The direction of motion of the wave function is indicated by a blue arrow.

2.3.3 Periodic Boundary Conditions

Another boundary that can be very useful to reduce computation time is the periodic boundary. Here, two opposing boundaries are mapped onto each other providing an infinite simulation domain via the compactification of one or many dimensions. Although periodic boundary conditions do not always represent physically realistic systems, they can be useful in a variety of situations. First, it is possible to represent cylindrical symmetry on a two-dimensional plane using periodic boundary conditions. Second, three-dimensional-like behaviour can be approximated by a single two-dimensional plane using periodic boundaries. For example, two planes at different heights that cross each other – similar to a road interchange – can be simulated entirely within one plane. Figure 2.3 shows a wave packet crossing a periodic boundary where the negative and positive extremes of the x dimension have been folded onto each other.

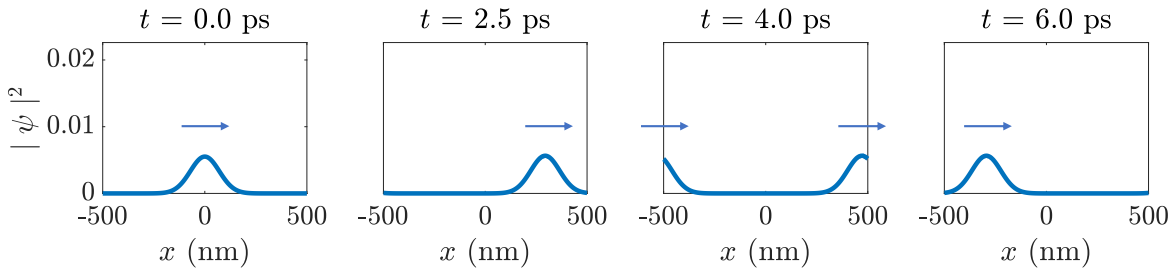

Fig. 2.3 A Gaussian wave packet is initialised in a 1D square well with initial momentum. The wave function is transmitted from the right boundary to the left boundary through periodic boundary conditions. The norm of the wave function is preserved throughout the simulation. The direction of motion of the wave function is indicated by a blue arrow.

2.4 Sliding-Window Simulation Domain

In certain cases, it is computationally beneficial to use a restricted simulation domain that is allowed to move over a larger area of interest. A semiconductor device is typically a few microns in length, but the desired spatial resolution of the wave function can be one nanometer or less. For large simulations, computational resources can become a limiting factor and time is wasted calculating the evolution of the wave function where it is zero. Instead, a sliding window domain can be used. Here, I find the solution to the Schrödinger equation for only a slice of the device. As the electron progresses through the device, the window is updated to keep the non-zero wave function lattice sites at the center of the domain.

Figure 2.4 shows two simulations of an electron being transported across a static potential by a surface acoustic wave. The underlying potential is a doubly-angled channel that takes the particle from $y = 0$nm to $y = 200$nm. In the left panel, the simulation domain spans the entire device and the wave function is only nonzero over a small fraction of the domain. An added benefit of a sliding window is that the wave function does not need to be initialised with a momentum component. Both simulations in Fig. 2.4 were initialised with zero momentum. A comparison between both panels shows that the surface acoustic wave provided an added momentum to the static wave function and caused the electron to oscillate in the x dimension within the SAW potential. This can be seen by the variable distance between the expected position of the electron in the left panel. By contrast, in the right panel, the sliding window simulation domain moved at the same speed as the SAW. Since the inertial reference frame is with respect to the surface acoustic wave, the default state of the electron is to move with the SAW. Sliding window simulations were used for all dynamic calculations in Chapter 6.

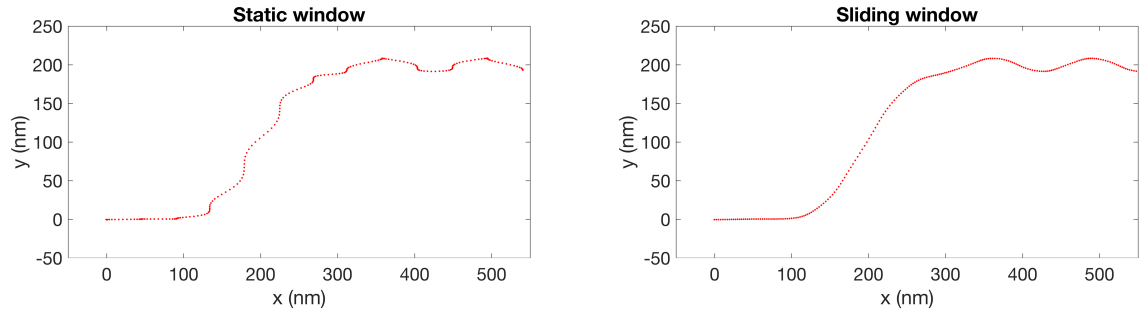

Fig. 2.4 Expected value of the position of a single-particle wave function as it travels across an electrostatic potential. A surface acoustic wave creates a confining potential in the x dimension and travels in the positive x direction.

2.5 Natural Units

Numerical calculations performed on modern computing systems typically use a floating-point system (floats) or double-precision numbers (doubles) for a greater number of significant digits. Other forms of numerical systems, such as complex numbers, are simply formed as arrays of floats or doubles. Because of the finite number of significant digits, it can be useful to use the *natural unit* system. In this system, orders of magnitude are centered around one. The advantage of the natural unit system is twofold. First, operations with floating-point numbers of the same order minimise the risk of truncating trailing digits. For example, when calculating the norm of the wave function, the sum of very small values divided another very small value should equal unity. However, this value may be smaller because of the truncation of trailing numbers. The second advantage is the rapid verification of nonsensical answers output from the simulations. It is hard for humans to have an intuitive understanding of numbers on the order of Planck's constant. A divergent solution may not appear immediately and would require post-processing to uncover. Using natural units, it is immediately apparent when a solution starts to diverge and parameters start drifting by orders of magnitude.

In this work, I set the reduced Planck constant [29] and the mass of an electron in free space to be equal to one.

$$m_e = 9.10938216 \times 10^{-31}\ \text{kg} \rightarrow 1 \tag{2.24}$$

$$\begin{aligned} \hbar &= 1.054571817 \times 10^{-34}\ \text{J}\cdot\text{s} \rightarrow 1 \\ &= 6.582119569 \times 10^{-16}\ \text{eV}\cdot\text{s} \rightarrow 1 \end{aligned} \tag{2.25}$$

The time-dependent Schrödinger equation is then expressed as

$$\begin{aligned} & i\hbar\frac{\partial}{\partial t}\psi = \left(-\frac{\hbar^2}{2m}\nabla^2 + V\right)\psi \\ \curvearrowright\quad & i\frac{\partial}{\partial t}\psi = \left(-\frac{1}{2}\nabla^2 + V\right)\psi \end{aligned} \tag{2.26}$$

The dimensions of the variables of interest must be scaled and expressed in terms of new units. In the simulations presented in this thesis, length is expressed in terms of nanometers. Units of time and energy are expressed as different powers of length. Table 2.1 offers a convenient conversion factor between units of energy, time, and momentum typically used in nanoscale experiments and the corresponding natural units.

Quantity	SI Units	Conversion Factor	Numerical Conversion	Natural Units
Energy	$[V] = \text{meV}$	$\frac{m_e}{\hbar^2}$	1.312342×10^{-2}	$\frac{1}{\text{nm}^2}$
Time	$[t] = \text{ps}$	$\frac{\hbar}{m_e}$	1.157676×10^{2}	nm^2
Momentum	$[p] = \text{kg}\frac{\text{m}}{\text{s}}$	$\frac{1}{\hbar}$	9.482522×10^{24}	$\frac{1}{\text{nm}}$

Table 2.1 Numerical conversion factors required when going from the International System of Units (SI) to Natural Units (NU).

2.6 GPU Acceleration

As discussed in this chapter, discretising large systems can lead to complex problems requiring a large amount of computational operations due to the rapid increase of spatial nodes. Graphics processing units (GPUs) are specially designed to process many operations simultaneously by splitting independent operations into blocks and executing them in parallel. Originally designed to rapidly create real-time images to be output to a display, GPUs are now optimised to make use of their parallel processing ability for processing large data structure and performing high performance computations. As a result, graphics cards offer a relatively inexpensive way of exploiting the equivalent of a small-scale supercomputer.

Modern GPUs have several thousand cores and can run on the order of 10^{13} floating-point operations per second (FLOPS). Figure 2.5 shows a comparison in the theoretical FLOPS achieved by Intel's most advanced central processing units (CPUs) and NVIDIA's GPUs.

Parallelising large tasks on a GPU can lead to a significant decrease in computational time compared to single- or multi-threaded CPU processing. To get a better idea of the use

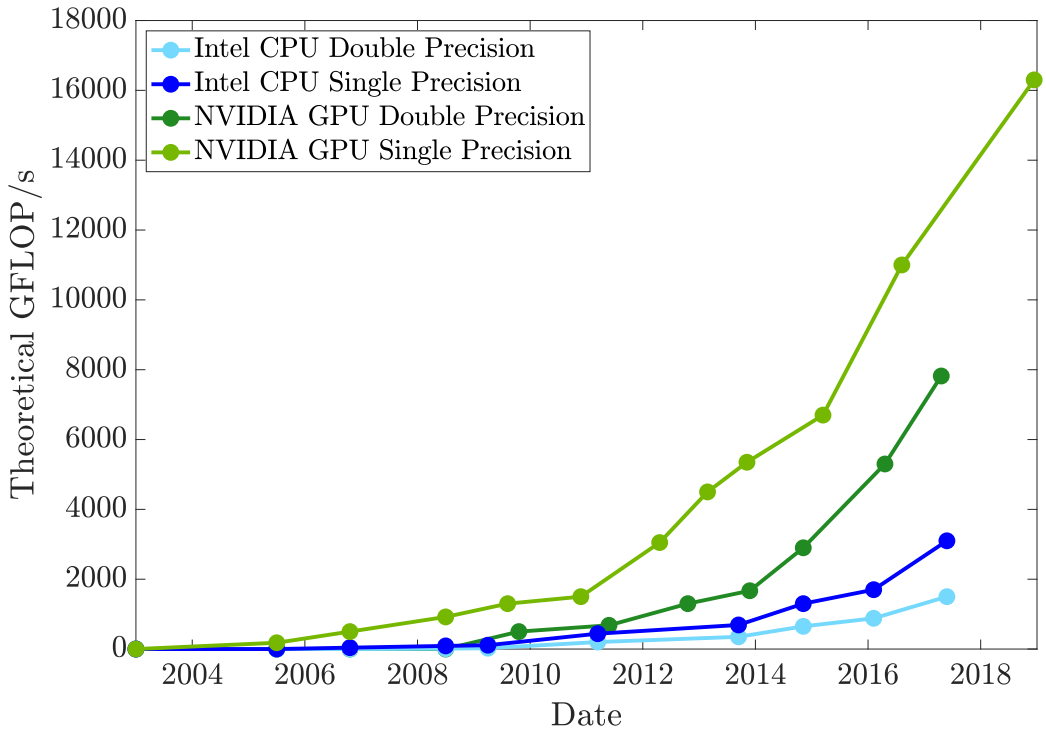

Fig. 2.5 Theoretical floating-point operations per second comparison between the modern, most advanced CPUs and GPUs. Image adapted from Nvidia CUDA programming guide.[119]

of parallel computing on GPUs, let us consider the simple case of vector addition. For this task, two arrays of size N, $\vec{a}$ and $\vec{b}$, are added to produce the resulting vector $\vec{c}$. A sample code in C to be executed by the CPU would look like the following:

```
1 for(int i = 0; i < N; ++i)
2 {
3     c[i] = a[i] + b[i];
4 }
```

Listing 2.3 CPU vector addition

The CPU executes this code in series. When encountering the `for` loop, it will execute each step of the loop in a sequential order. An equivalent expanded view of the CPU processing can be seen in the following code:

```
1 c[0] = a[0] + b[0];
2 c[1] = a[1] + b[1];
```

```
3 c[2] = a[2] + b[2];
4 ...
5 c[N-1] = a[N-1] + b[N-1];
```

Listing 2.4 CPU vector addition (expanded code)

Since each step of the vector addition operation is independent from another, the output result is no different if the operations are executed out of order. For such tasks, GPUs can split iterative processes and execute each operation on one of many computing cores. Independent operations are processed simultaneously to gain a greater time efficiency. A sample OpenCL code for vector addition can be seen below:

```
1 kernel void myVectorAddition(global float *a, global float *b, global ↩
    float *c)
2 {
3     i = get_global_id(0);
4     c[i] = a[i] + b[i];
5 }
```

Listing 2.5 GPU vector addition

Here, each thread is assigned a global index by the GPU kernel. Each work-group, or block of computing cores, can access and identify a thread using the `get_global_id(d)` function where `d` identifies the dimension of the problem. Since most graphics cards are designed to render scenes or images intended for display, GPUs are optimized to work in one, two, or three dimensions. Systems with higher dimensionality must be adapted to work within these constraints.

GPU acceleration is a powerful tool when applied to the staggered leapfrog method. In this case, the relevant equations to be solved in parallel are Eq. 2.16a and Eq. 2.16b. The temporal iterative process of the staggered leapfrog method must be solved sequentially since each time step depends on the previous, however, the nodes of the array generated by spatial discretization are independent from each other within one time step. Each node of the wave function can be solved in any given order. The possibility of accelerating simulations of the TDSE through the use of parallel processing is another reason why the staggered leapfrog method is desirable.

Data precision is an important factor to consider when performing numerical computations. The two main precision formats used to store floating-point values are single-precision and double-precision. Single floats use 4 bytes of computer memory and usually offer an accuracy of 7-8 decimal points, whereas double floats take, as the name suggests, 8 bytes of memory and can store 15-16 decimal places. Accuracy is desirable in physical simula-

tions, but the use of double-precision numbers at least doubles the necessary computational resources and requires longer running times. Furthermore, certain graphics cards are particularly affected by using double precision as will be discussed later in this section. The simulations in this thesis were done using single-precision floats to take advantage of faster computation times. A comparative test solving the same problems using double-precision values showed no change in the accuracy of the result.

2.6.1 CUDA vs OpenCL

Finally, there are many hardware platforms as well as application programming interfaces (APIs) to choose from when deciding to use GPUs for computational purposes. There are currently three main graphics cards manufacturers: AMD, Intel, and Nvidia. Intel GPUs are mainly marketed towards high power efficiency desktop and mobile devices. The computing power of Intel devices is not sufficient for the needs of this research. AMD and Nvidia both offer high-end products capable of increasing computational performance over CPUs and both device families come with their set of advantages and drawbacks. Nvidia devices are better supported by different platforms such as Windows and Linux through well maintained drivers, however, most Nvidia cards are not optimized for handling double precision floats and are even slowed down to promote Nvidia's more powerful Tesla devices. AMD, on the other hand, typically offers a more inexpensive product that can perform operations on floating point or double precision equally. AMD's driver support for Linux devices usually trails behind a few years.

The most developed APIs available for scientific computing on GPUs are CUDA, Microsoft DirectCompute, and OpenCL. CUDA is a well developed and well maintained parallel computing platform offered by Nvidia and is available on different platforms, however, it can only run on Nvidia hardware. DirectCompute is developed by Microsoft and released alongside the DirectX environment. It supports all hardware manufacturers, but it is tied to Windows systems only. OpenCL, maintained by the Khronos Group, offers the best balance by supporting all major card manufacturers and multiple operating systems (Windows, Linux, and MacOS). Other graphics card APIs such as OpenGL or Project Vulkan are designed for computer graphics processing and are not optimal for scientific simulations. In this research, I used a combination of OpenCL and CUDA. I originally used OpenCL, which produced the results for Chapter 5, for its versatility and compatibility with AMD graphics cards. I then used CUDA for the remaining simulations and the results of Chapters 3, 4, and 6 because of its constant development and active userbase. The results in Chapter 3 were produced using an NVIDIA GTX 970 GPU. The results in Chapter 4 were obtained with an NVIDIA GTX

1080Ti GPU. In Chapter 5, I used an AMD Radeon R9 390 GPU. Finally, in Chapter 6, I used an NVIDIA RTX 2080Ti GPU.

2.7 Example

As a preliminary check, I compare the results of my code to a well-known quantum phenomena, the double-slit experiment. Figure 2.6 shows the time evolution of a single-particle wave function initialised as two Gaussian wave packets separated in space. The exact parameters used to generate Fig. 2.6 as well as a simplified code of the staggered leapfrog method can be found in Appendix A. As expected, an interference pattern is observed matching both analytical calculations and experimental observations. It is important to note that in this particular case, additional interference fringes can be observed. This is due to the particle's wave function being reflected off the hard wall boundaries.

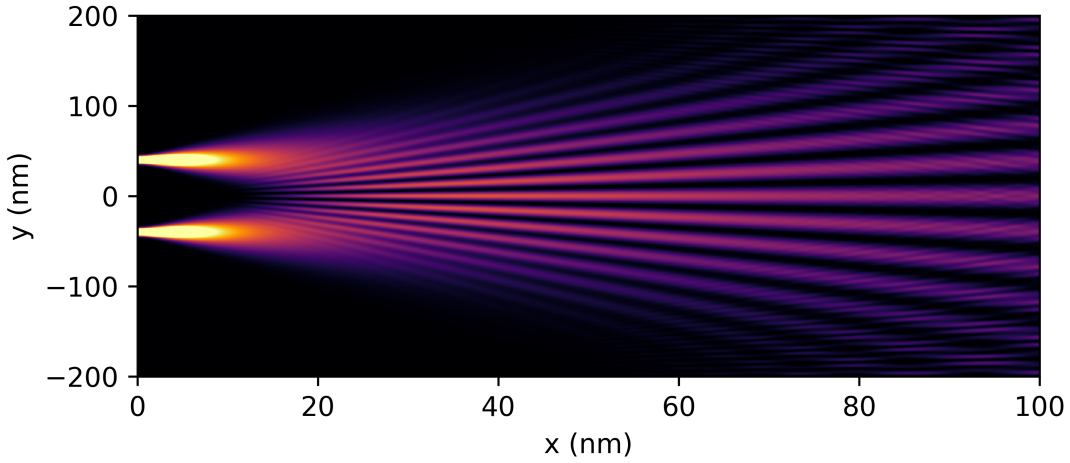

Fig. 2.6 A single particle wave function propagates from two slits. Interference patterns emerge both from self interference and from reflections of the wave function on the hard wall boundaries of the simulation domain.

3

SINGLE-ELECTRON MANIPULATION

Using the methods and tools presented in Chapter 2, I model the states of single particles and the way quantum information is encoded in them. In this research, I investigate single electrons as a physical platform for quantum information processing. In this chapter, I lay the groundwork for defining qubits using electrons. I define an electron qubit in a simple, static, double quantum dot. Simpler models are useful tools to gain insight into the behaviour and dynamics of particles in various systems. They are also a useful method to compare the results of numerical simulations against analytical predictions – an essential confirmation before moving on to more complex problems. The double quantum dot is also a natural starting point since most of the further work in this thesis relates to electrons being transported in parallel quantum channels by surface acoustic waves, thus creating moving double quantum dots.

3.1 The Electron Qubit

There are two main ways to encode quantum information using single electrons. First, two spatially separated states can be created from the energy eigenstates of the electron. This type of system is referred to as a charge qubit [22, 65]. In a semiconductor, a charge qubit can manifest itself as localised states in a double quantum dot. The $|0\rangle$ and $|1\rangle$ basis states

are defined as the particle's presence in one or the other quantum dot. An advantage of the charge qubit include the clear readout owing to the localisation of the wave function of the electron. This localisation can also be used to control any interactions with neighbouring qubits. Two-qubit operations can be turned on and off by controlling the spacial proximity of the electrons. Another advantage of charge qubit devices is that all the parameters controlling the quantum information can be adjusted by applying surface gate voltages. A second type of qubit is the spin qubit [124, 75]. In this case, the two spin states $|\uparrow\rangle$ and $|\downarrow\rangle$ form the basis of the qubit. Spin qubits are a natural candidate for quantum information processing since these are the two only possible states of the system. As opposed to charge qubits, careful engineering is not required to ensure other states are not present. However, the dynamics of charge qubits are important for spin qubits when two-qubit gate are constructed or when the qubits are transported.

In this chapter, I will focus on the charge qubit, since I am interested in the dynamic propagation of electrons in circuits and therefore the evolution of fermionic wave functions in quantum circuits. Experimental devices capable of creating, manipulating, and reading charge qubits currently exist and offer results capable of validating my simulations [149]. Comparisons to experimental results are presented in Chapter 4.

3.1.1 The "Optimal" Qubit

In experimental works, it is often assumed that the wave functions of the basis states of a single electron in a double quantum dot, $\psi_0(x)$ and $\psi_1(x)$, are fully localised in one or the other quantum dot and equivalent to the ground state eigenvector of a single quantum dot [77, 72, 51]. While this assumption is convenient for defining the spatial extent of the qubit and setting up the experimental layout, it introduces errors in the readout process, which measures the probability of the electron being in a particular quantum dot. In this case, the non-zero overlap between the two states as well as the presence of higher excitation states give rise to coherent oscillations typically on timescales faster than the qubit oscillation itself [87], ultimately inducing a loss of fidelity in gate operations. This issue is critical for practical implementations of quantum computation and schemes like bang-bang pulse sequences have been proposed in order to mitigate unwanted rotations around the Bloch sphere [158, 114]. However, such schemes involve additional gate operations that increase the overall operation time. Instead, the optimisation of the qubit basis states reduces the presence of high energy states and allows the coherent oscillations of the particle between the two quantum dots to be predicted and controlled.

For simplicity, let us define the double quantum dot potential as

$$V_{\mathrm{DQD}}(x) = Ax^2 + B\exp\left(\frac{-x^2}{2\sigma}\right). \tag{3.1}$$

This functional form for V_{DQD} allows the control of the DQD by varying the harmonic confinement A and the tunnel barrier height B and width σ. The energy difference $\Delta = E_{\mathrm{AB}} - E_{\mathrm{B}}$ is defined by the energy of the bonding ground state E_{B} and the antibonding first excited state E_{AB}. An electric detuning between the two quantum dots is introduced via a linear bias voltage:

$$V_{\mathrm{bias}}(x) = V_{\mathrm{slope}}\frac{x}{w}, \tag{3.2}$$

where w is defined as the width between the two quantum dots.

Given the double quantum dot potential in Eq. 3.1, let us define the optimal qubit basis two states $\psi_0(x)$ and $\psi_1(x)$. In order to make the readout measurement of arbitrary qubit states $\psi(x) = \alpha\psi_0(x) + \beta\psi_1(x)$ as straightforward as possible, these basis states should be maximally localised in either one of the other double quantum dot. In order to avoid complex, high frequency oscillations between both states, $\psi_0(x)$ and $\psi_1(x)$ are defined as a linear combinations of the two lowest eigenstates of the unbiased DQD system, that is, the bonding and anti-bonding states $\psi^{\mathrm{B}}(x,\varepsilon)$ and $\psi^{\mathrm{AB}}(x,\varepsilon)$ for detuning value ε. Detuning is defined as the potential energy difference between the minimum of each quantum dot. Hence, the qubit basis states are defined as

$$L,R(x,\varepsilon) \quad = \quad \alpha_\varepsilon\psi^{\mathrm{B}}(x,\varepsilon) \pm \beta_\varepsilon\psi^{\mathrm{AB}}(x,\varepsilon), \tag{3.3}$$

where α_ε and β_ε are complex variables, $|\,\alpha_\varepsilon\,|^2 + |\,\beta_\varepsilon\,|^2 = 1$. The parameters α_ε and β_ε are chosen such that the integrals

$$\int_{-\infty}^{0} |\,L(x,\varepsilon)\,|^2\,\mathrm{d}x \tag{3.4a}$$

$$\int_{0}^{\infty} |\,R(x,\varepsilon)\,|^2\,\mathrm{d}x \tag{3.4b}$$

are maximised. The natural detuning value for a symmetric system is $\varepsilon = 0$. An unbiased system provides the optimal readout probabilities for both $|0\rangle$ and $|1\rangle$ qubit basis states. It follows that the optimal values for the parameters α_ε and β_ε are also symmetric when $\varepsilon = 0$. When considering parity inversion symmetry for $V_{\mathrm{bias}}(x,t) = 0$, we have that $R(-x,0) = L(x,0)$ with $\psi^{\mathrm{B}}(-x,0) = \psi^{\mathrm{B}}(x,0)$ and $\psi^{\mathrm{AB}}(-x,0) = -\psi^{\mathrm{AB}}(x,0)$. Therefore,

the coefficients are $|\alpha_0| = |\beta_0| = 1/\sqrt{2}$ and the optimal charge qubits are defined as

$$\psi_0(x), \psi_1(x) = L, R(x,0) = \frac{\psi^{\mathrm{B}}(x,0) \pm \psi^{\mathrm{AB}}(x,0)}{\sqrt{2}}. \tag{3.5}$$

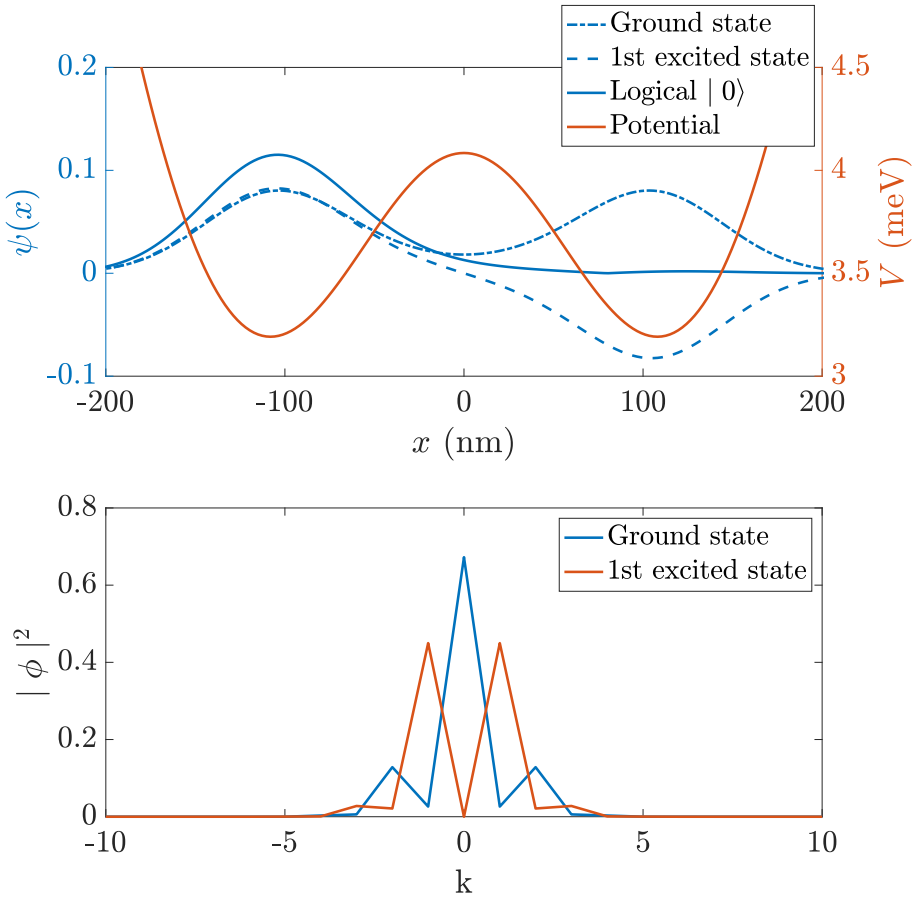

Fig. 3.1 Ideal DQD qubit. Top panel: Wave function of the ground state, first excited state and the logical formed using Eq. 3.5 Bottom panel: Ground and first excited state in momentum space.

This definition for qubits is optimal in the sense that the wave function is maximally and symmetrically localised on the quantum dots while being described by only two energy eigenstates. Although the basis states are not completely localised on a single dot, since there is a non-zero overlap between the two wave functions, they maximise the average probability of a successful readout. Further localisation of the states lead to higher-energy states which in turn affect the fidelity of quantum operations on the qubit. Figure 3.1 illustrates the wave function of the logical $|0\rangle$ basis state formed using Eq. 3.5. The lower panel in Fig. 3.1

shows that solving the Schrödinger equation in momentum space can significantly reduce the computational complexity of the problem since only a few momentum states are non-zero.

3.1.2 Qubit Rotations

In Sec. 3.1.1, I defined a qubit basis for an electron in a double quantum dot. In order to have complete control of this qubit, a general rotation scheme must be defined. Given the Hamiltonian in Eq. 2.4, a general rotation $\mathscr{R}_{\vec{n}}(\alpha(t))$ of angle α on the Bloch sphere around a vector $\vec{n}$ is given by the solution to the time-dependent Schrödinger equation:

$$\mathscr{R}_{\vec{n}}(\alpha(t)) = \hat{\mathscr{T}} \exp\left[\frac{1}{i\hbar}\int_0^t \hat{H}(t')\mathrm{d}t'\right], \tag{3.6}$$

where $\hat{\mathscr{T}}$ is a time-ordering operator. Such rotations are performed by applying an electric bias pulse of a fixed amplitude $A = \lambda\varepsilon$ for a duration t_p to the double quantum dot. Different values of A lead to different axes of rotation, which can be combined to apply a general rotation. Here, ε is the electric potential detuning between the two dots and λ is a proportionality constant relating the voltage applied to surface gates and the resulting change in electric potential. An instantaneous switch between the $A = 0$ and $A = \lambda\varepsilon$ bias states is generally preferred as this simplifies the dynamics rotations [97]. However, large instantaneous potential changes can cause further complicaions such as Landau-Zener transitions. In the case of instantaneous bias switching, the dynamic detuning $\varepsilon(t)$ is described by a set of step-functions. The resulting rotation $\mathscr{R}_{\vec{n}}(t)$ can be expressed analytically as a rotation of the qubit state on the Bloch sphere. The direction of the rotation is determined by the energy eigenstates of the system's Hamiltonian, including $\varepsilon(t)$, and the rate of rotation is defined by the energy difference between the two eigenstates. For a given detuning ε, the unitary time evolution of the qubit is

$$\mathscr{R}_{\vec{n}}(\alpha(t)) \propto \exp\left[-i\frac{(\Delta,0,\varepsilon)\cdot\vec{\sigma}}{2\hbar}t\right], \tag{3.7}$$

where Δ is the energy difference between the two first energy eigenstates and $\vec{\sigma}$ are the Pauli matrices [118]. The vector $(\Delta,0,\varepsilon)$ defines the rotation's axis as well as its frequency. When the symmetric and anti-symmetric eigenstates have different eigenenergies, $\Delta > 0$ and the qubit undergoes a natural preccession around the Bloch sphere. Both the frequency and the axis of rotation can be adjusted experimentally by applying voltages to surface gates and modulating ε. Although applying a voltage to surface gates is straightforward, implementing a perfect square pulse is technically challenging. Pulse pattern generator electronics have a

finite frequency bandwidth and a rising time τ greater than ten picoseconds. In this specific case, a step-function decomposition is not possible and, in general, Eq. 3.6 must be solved numerically.

In the case of a non-square pulse, the dynamics of the time evolution of Eq. 3.6 differ from Eq. 3.7 [63]. Arbitrary rotations around the Bloch sphere are possible, however, the more complex dynamics during the finite rise and fall of the pulse must be taken into account. These dynamics are currently being studied in ongoing research and are beyond the scope of this thesis. Experimentally, increasing both the pulse duration and amplitude reverse the effects of finite pulse times. These modified operations are still rotations on the Bloch sphere since the instantaneous Hamiltonian is expressed in terms of σ_x and σ_z matrices. Therefore, the effective operation is composed of rotations and is itself a rotation.

In order to be able to perform arbitrary qubit rotations, a series of up to five square pulses of alternating amplitudes are concatenated. In general, the fastest rotation operation time is obtained by applying a voltage that gives $\varepsilon = \pm\Delta$. Here, the axes of rotation during the pulse are along the vectors $(\pm 1, 0, 1)$ of the Bloch sphere. Let us label these new axes as $\vec{x'}$ and $\vec{z'}$ respectively. These new coordinates are rotated by $-\frac{\pi}{4}$ around $\vec{y}$ with respect to the $\vec{x}$ and $\vec{z}$ axes of the Bloch sphere.

An arbitrary rotation by an angle α is performed around the $\vec{n}$ axis using

$$\mathscr{R}_{\vec{n}}(\alpha) = \mathscr{R}_{\vec{x'}}\left(\frac{\pi}{2} - \phi\right)\mathscr{R}_{\vec{z'}}(\theta)\mathscr{R}_{\vec{x'}}(\alpha)\mathscr{R}_{\vec{z'}}(-\theta)\mathscr{R}_{\vec{x'}}\left(\phi - \frac{\pi}{2}\right), \tag{3.8}$$

where θ and ϕ are the polar and azimuthal angles on the Bloch sphere of $R_{\vec{y}}(-\frac{\pi}{4})$ applied onto $\vec{n}$.

While it is necessary to use a five-pulse train in order to perform an arbitrary rotation, a simpler pulse shape can be found for some common specific operations, such as initialisation from ground state to qubit $|0\rangle$ or $|1\rangle$.

3.1.3 State Preparation

Before any quantum operation, the qubit must be initialised to a well defined fiducial state, generally either $|0\rangle$ or $|1\rangle$. For a generic experiment involving a charge qubit, the initial state of the electron is expected to be in the ground state of Eq. 2.4. However, such a state is not part of the qubit's computational basis and an initial rotation is thus needed. From the ground state, the $R_{\vec{z'}}(\pi)$ rotation is used to rotate the wave function to the $|0\rangle$ state. Alternatively, a $R_{\vec{x'}}(\pi)$ rotation can be used to initialise a qubit from the ground state to the $|1\rangle$ state. Both of these operations are achieved with a single voltage pulse.

3.1.4 Single Axis Rotations

Any single qubit operation can be expressed in terms of rotations around three perpendicular axes. The control sequence for rotations around the $\vec{x}$, $\vec{y}$, and $\vec{z}$ axes of the Bloch sphere are given by

$$R_{\vec{x}}(\alpha) = R_{\vec{x}'}\left(\frac{\pi}{2}\right) R_{\vec{z}'}\left(\frac{3\pi}{4}\right) R_{\vec{x}'}(\alpha) R_{\vec{z}'}\left(\frac{5\pi}{4}\right) R_{\vec{x}'}\left(\frac{3\pi}{2}\right), \tag{3.9a}$$

$$R_{\vec{y}}(\alpha) = R_{\vec{z}'}\left(\frac{\pi}{2}\right) R_{\vec{x}'}(\alpha) R_{\vec{z}'}\left(\frac{3\pi}{2}\right), \tag{3.9b}$$

$$R_{\vec{z}}(\alpha) = R_{\vec{x}'}\left(\frac{\pi}{2}\right) R_{\vec{z}'}\left(\frac{1\pi}{4}\right) R_{\vec{x}'}(\alpha) R_{\vec{z}'}\left(\frac{7\pi}{4}\right) R_{\vec{x}'}\left(\frac{3\pi}{2}\right). \tag{3.9c}$$

At zero detuning, the spatial overlap between the two basis states $\psi_0(x)$ and $\psi_1(x)$ implies that a σ_z rotation occurs automatically with a period of $T_z = \frac{\hbar}{\Delta}$. For a single qubit, no pulsing is required to achieve this rotation. For multiple qubits, an idle σ_z rotation is not as straightforward. Realistically, multiple double quantum dots are not identical and the energy difference Δ, although experimentally tunable, is not necessarily the same for each dot, leading to different σ_z periods. In this case, each qubit can be delayed with respect to its neighbours by applying a single square pulse over a 2π rotation. The period of this delay rotation is determined by ε via the amplitude of the pulse.

Instead of using the $\vec{x},\vec{y},\vec{z}$ basis, it is favourable to use the rotated $\vec{x'},\vec{y},\vec{z'}$ basis, which is more natural for the detuned system. In this rotated basis, fewer pulses are required to define logic gates. $R_{\vec{x}'}, R_{\vec{z}'}$ are achieved with a single pulse, while $R_{\vec{y}}$ requires a three-pulse train, as in Eq. 3.9b. Typical quantum logic gates are defined as

$$X = R_{\vec{x}}(\pi), \tag{3.10}$$

$$Y = R_{\vec{y}}(\pi), \tag{3.11}$$

$$Z = R_{\vec{z}}(\pi), \tag{3.12}$$

$$H = R_{\vec{z}'}(\pi), \tag{3.13}$$

$$R_\phi = R_{\vec{z}}(\phi). \tag{3.14}$$

3.1.5 Correcting for Finite Rise Time

To account for the imperfect realistic pulse shape due to rise time and limited bandwidth, the bias voltage and pulse duration have to be adjusted. This adjustment depends on the single

pulse rotation angle and rise time, but not on the input state. Therefore, it is sufficient to optimise a single pulse for a given rise time and range of desired rotations. These adjusted pulses are concatenated into a pulse train to achieve arbitrary qubit rotations of high fidelity. Using a method of gradient descent, it is possible to numerically find the correct adjustments depending on rise time. This allows experimentalists to apply the ideal control sequence by simply changing the amplitude and duration of each square pulse in the train, thus avoiding complicated pulse shapes while retaining high fidelity.

3.2 Readout

DiVincenzo's 5$^{\text{th}}$ criterion requires a quantum state to be measurable. In experimental setups, it is the probability of finding the electron in one of the dots which is accessible and measured rather than the qubit superposition coefficients. For example, one can monitor the current through a quantum point contact to detect the presence of an electron in a quantum dot [9]. This shift is proportional to an effective charge that is related to the probability distribution in the double dot structure. We can relate this probability to the wave function coefficients [115].

Both qubit basis states defined in Eq. 3.5 can be written in terms of their spatial extent in the left $(\varphi_{iL}(x))$ and right $(\varphi_{iR}(x))$ quantum dots as

$$\psi_0(x) = \varphi_{0L}(x) + \varphi_{0R}(x) \tag{3.15a}$$

$$\psi_1(x) = \varphi_{1L}(x) + \varphi_{1R}(x) \tag{3.15b}$$

The basis states $\psi_0(x)$ and $\psi_1(x)$ are orthonormal, which gives

$$\begin{aligned} 0 &= \int \psi_0^*(x)\psi_1(x)dx \\ &= \int \varphi_{0L}^*(x)\varphi_{1L}(x)dx + \int \varphi_{0L}^*(x)\varphi_{1R}(x)dx + \int \varphi_{0R}^*(x)\varphi_{1L}(x)dx + \int \varphi_{0R}^*(x)\varphi_{1R}(x)dx \\ &= \int \varphi_{0L}^*(x)\varphi_{1L}(x)dx + \int \varphi_{0R}^*(x)\varphi_{1R}(x)dx. \end{aligned} \tag{3.16}$$

For an unbiased system, the optimal qubit basis states $\psi_0(x)$ and $\psi_1(x)$ are symmetrical.

The optimal qubit basis defined in Eq. 3.5 once again turns out to be the best suited. The qubit states $\psi_0(x)$ and $\psi_1(x)$ are mirror images of each other. This means $\psi_0(x)$ has the same

spatial distribution in the left (right) dot as $\psi_1(x)$ has in the right (left) dot, which leads to

$$\int \varphi_{0L}^*(x)\varphi_{1L}(x)dx = \int \varphi_{0R}^*(x)\varphi_{1R}(x)dx = 0. \tag{3.17}$$

Any arbitrary state can be written as a linear combination of the two qubit basis states and, thus, their left and right spatial contributions are written as

$$\psi(x) = \alpha\psi_0(x) + \beta\psi_1(x) = \alpha\Big(\varphi_{0L}(x) + \varphi_{0R}(x)\Big) + \beta\Big(\varphi_{1L}(x) + \varphi_{1R}(x)\Big). \tag{3.18}$$

As an example, the probability P_R of finding the particle in the right quantum dot is

$$P_R = \int_0^\infty \psi^*(x)\psi(x)dx = \int_0^\infty \Big(\alpha^*\varphi_{0R}^*(x) + \beta^*\varphi_{1R}^*(x)\Big)\Big(\alpha\varphi_{0R}(x) + \beta\varphi_{1R}(x)\Big)dx. \tag{3.19}$$

Using Eq. 3.17, the probability reduces to

$$P_R = |\alpha|^2\int_0^\infty \varphi_{0R}^*(x)\varphi_{0R}(x)dx + |\beta|^2\int_0^\infty \varphi_{1R}^*(x)\varphi_{1R}(x)dx \equiv |\alpha|^2P_{0R} + |\beta|^2P_{1R}, \tag{3.20}$$

where the probabilities P_{0R} and P_{1R} refer to the qubit state $|0\rangle$ and $|1\rangle$ being located in the right quantum dot. Although one may think it is desirable to have only one computational state per dot, therefore minimising the other, a finite spatial overlap is require to perform single-qubit unitary operations. Applying the normalisation condition $|\alpha|^2 + |\beta|^2 = 1$ to Eq. 3.20 yields

$$|\beta|^2 = \frac{P_R - P_0}{P_1 - P_0}, \tag{3.21}$$

This equation relates $|\beta|$ to the probability P_R of finding the particle in the right quantum dot. Similarly,

$$|\alpha|^2 = \frac{P_L - P_0}{P_1 - P_0}. \tag{3.22}$$

This concludes the definition of an optimal basis for a single-electron charge qubit. I defined a two-level system with the states $\psi_0(x)$ and $\psi_1(x)$ in Eq. 3.5 and I described how to initialise, rotate, and measure the qubit.

3.3 Coherent and Squeezed States

The double quantum dot system described in this chapter is assumed to be static. However, in the rest of this thesis, I investigate electrons carried by surface acoustic waves. Because of the constant confinement generated by the SAW potential, a moving quantum dot is no different from a static one if the observer's inertial frame of reference is boosted to match that

of the SAW. Differences arise when the underlying electrostatic potential forces the quantum dot out of its resting position. In Chapters 4, 5, and 6, I simulate circuits with channels that bend and couple to other channels via tunnel barriers. A non-adiabatic change in the underlying potential causes the electron carried by the SAW to become excited and exist in a superposition of higher-energy excited states [103, 167, 147, 109]. Investigating simple models of harmonic channels, I found that the excitations produced in the single-electron wave function matched optical coherent states [26, 25].

The ground-state wave function of a single particle carried by a SAW along a straight harmonic channel generates the same pattern as the vacuum state of laser light. A sharp tapering or thickening of this harmonic channel, created by applying different voltages to surface gates, creates an oscillating state similar to the optical squeezed vacuum state. A double bend in the channel, causing the particle to be displaced spatially, imparts momentum to the electron, causing it to oscillate in the harmonic channel while preserving its Gaussian shape. This behaviour is similar to a Glauber state for optical systems. Combining a tapered or thickened channel with a positional displacement creates oscillatory patterns that match optical amplitude-squeezed states and phase-squeezed states. All of these coherent states are shown in Fig. 3.2 for both experimental observations for laser light and simulation results for a single-electron wave function in a SAW potential.

It is important to consider the presence of coherent states when the underlying potential is changing. This is not to say that these states should be avoided. When accounted for correctly, they do not produce any loss in qubit fidelity, nor do they disrupt quantum-logic-gate operations. The creation of a coherent state is reversable and the ground state can be recovered from any of the states in Fig. 3.2.

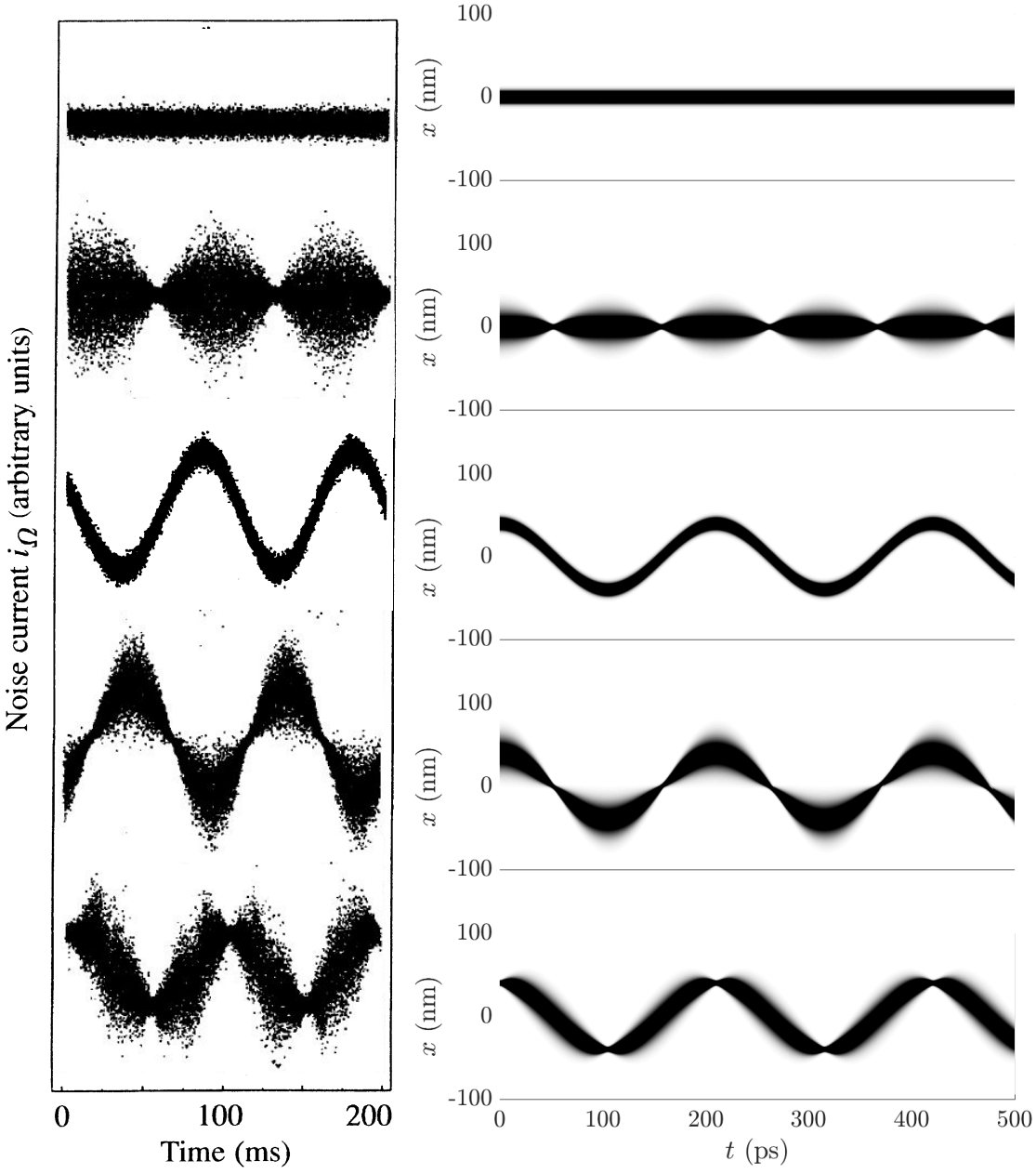

Fig. 3.2 Left: Coherent and squeezed states for laser light in a vacuum. From top to bottom, the different states are (i) vacuum state, (ii) squeezed vacuum state, (iii) Glauber state, (iv) amplitude-squeezed state (v) phase-squeezed state. This image was adapted from [26] and [25]. Right: Time-dependent simulations for a single-electron in a moving quantum dot. Each optical coherent state can be reproduced using electrons.

4

SINGLE-ELECTRON BEAM SPLITTER

In this chapter, I investigate DiVincenzo's 6th criterion, which requires the transmission of quantum information between stationary nodes [49]. My aim is to model a real semiconductor device and study the quantum information processing that can be performed on single electrons as they are in transit. Several approaches have demonstrated successful transmission of quantum states in solid-state devices such as in quantum-dot (QD) arrays [62, 66, 113] or microwave-coupled superconducting qubits [108, 131]. Here, I will combine the single-electron control methods presented in Chapter 3 with the surface-acoustic-wave techniques presented in Sec. 1.3. Experimentally, SAW-driven single-electron-transport devices are still in their early stages, but some groups have shown that it is possible to carry the particles reliably from one quantum dot to another [111, 79, 20]. From Sec. 1.3, we know that surface acoustic waves strongly modulate the electric potential in piezoelectric materials. In semiconductor heterostructures, such as GaAs/AlGaAs, SAWs can thus be employed to transfer individual electrons between distant quantum dots. This transfer mechanism makes SAW technologies a promising candidate to convey quantum information through a circuit of quantum logic gates [156, 14].

Figure 4.1 provides a three-dimensional schematic rendering of the electron transport process. A sinusoidal surface acoustic wave propagates along the device, creating a periodic train of minima capable of carrying electrons. This SAW train conveys single electrons from

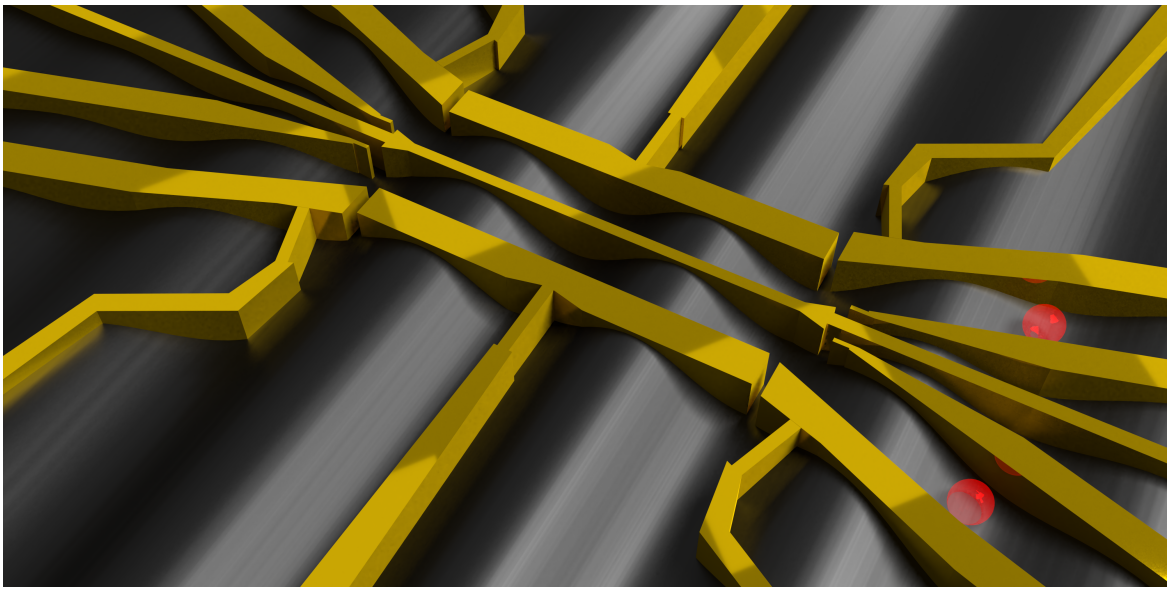

Fig. 4.1 3D rendering of a Single-electron beam splitter. Schottky gates (golden) create an electrostatic potential that guides the electron through the device. The central gate is tuned to allow the electron to coherently tunnel between both channels. Image adapted from [53]

one quantum dot to another along channels or "quantum rails" defined by metallic Schottky gates. Improving upon a simple transport process, one can apply voltages to the metallic gates and perform simple quantum information processing on the electrons whilst in transit. A quantum operation that is of particular interest is the generation of a superposition state via a tuneable beam splitter. Such a beam splitter can be used to create a spatial superposition for charge qubits or a spin-polarising beam splitter can couple the charge and spin states of spin qubits.

This work was a collaborative effort with various researchers at the Insitut Néel, Centre national de la recherche scientifique (CNRS) and the Université Grenoble Alpes. In particular, Dr. Hermann Edlbauer and Dr. Shintaro Takada are responsible for the experimental device fabrication, operation, and measurement. The findings in this chapter have been published in Nature Communications 10, 4557 (2019) [149].

4.1 Ideal Model

Typically, a beam splitter is used in optics to spatially separate a beam of light into two parts. Quantum mechanically, the wave function of a single photon can be split into a superposition of two spatial states. In 2001, Knill, Laflamme, and Millburn (KLM) put forward a scheme capable of universal quantum computation using only beam splitter and phase shifters on

single photons [94]. The same ideas put forward in the KLM scheme can be applied to single electrons. Electric or magnetic fields replace the phase shifters and a carefully tuned potential barrier can act as a beam splitter.

The ideal single-electron beam splitter is one where a single interaction between the particle and the barrier creates a spatial separation between two parts of the wave function. A repetition of the same operation should cause the wave function to return to a single beam, which is spatially localised. Figure 4.2 illustrates the path of a single-electron wave function as it interacts with a beam splitter twice. In this particular case, adjusting the phase of the separate parts of the wave function can cause the beam to be collimated on one side or the other of the beam splitter.

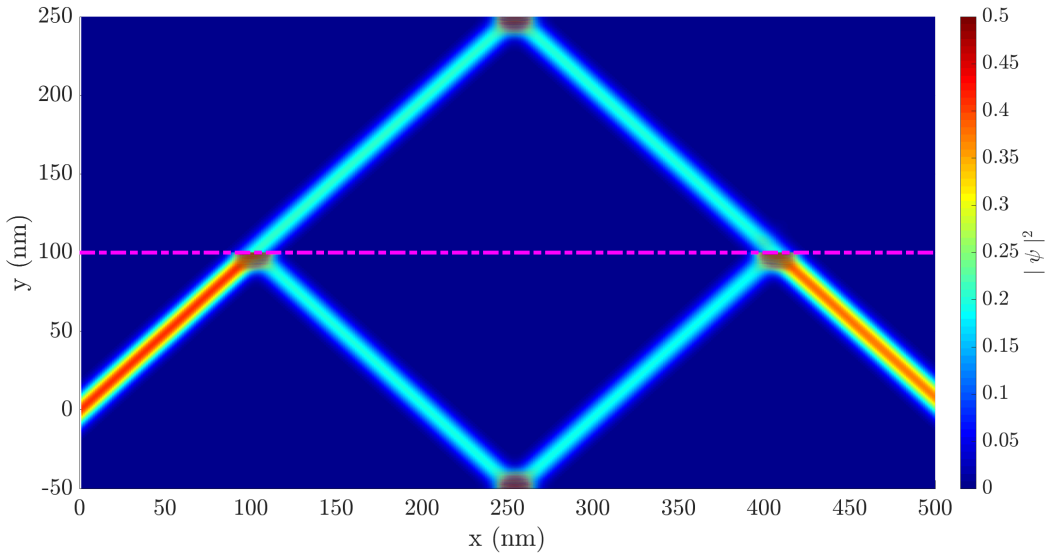

Fig. 4.2 Trajectory of a single-electron wave function as it encounters a beam splitter at $y = 100$nm (dashed magenta line). The electron interacts with the beam splitter twice, once at $x = 100$nm and once at $x = 100$nm. The phase of the wave function is chosen to maximize the wave function exiting in the lower part of the beam splitter. The underlying potential is an infinite square well with boundaries at $y = -50$nm and $y = 250$nm.

The operation presented in Fig. 4.2 is one of a 50/50 beam splitter, which splits the wave function into equal parts. The fraction of the wave function that is split is controlled by the height of the potential tunnel barrier (identified in magenta in Fig. 4.2). Experimentally, the amplitude of the tunnel barrier can be difficult to control precisely. In such a case, the desired superposition state can be achieved through multiple small operations. Although repeated operations increase the risk of introducing errors, as long as the process is coherent, the resulting state will be identical to a single operation.

4.2 Experimental Setup

The SAW-driven single-electron beam splitter is realised via surface electrodes forming a depleted potential landscape in the two-dimensional electron gas (2DEG) of a GaAs/AlGaAs heterostructure. An interdigital transducer (IDT) is used to send a finite SAW train towards our single-electron circuit as shown schematically in Fig. 4.3a. The SAW allows the transport of a single electron from one gate-defined QD (source) to another stationary QD (receiver) through a circuit of quantum rails. Figure 4.3b shows a scanning-electron-microscopy (SEM) image of a source QD with a schematic description of the electrical connections. To detect the presence of an electron, a quantum point contact (QPC) is placed next to the QD. By biasing this QPC at a sensitive working point, an electron leaving or entering the QD can be detected by a jump in the current, I_{QPC} [61].

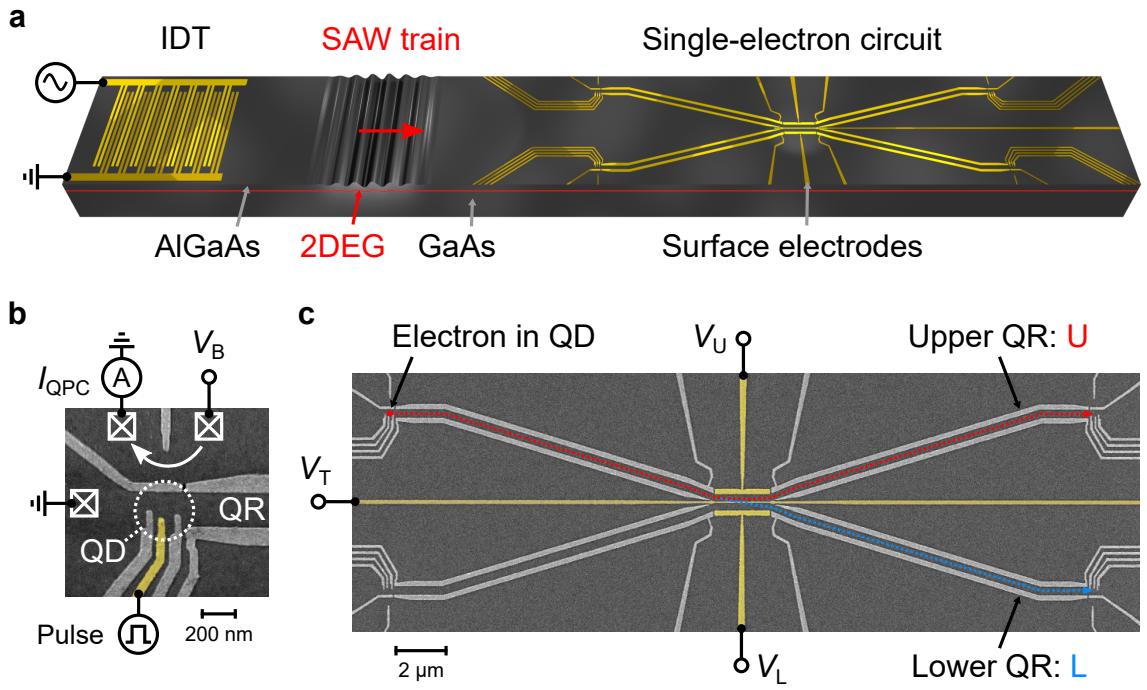

Fig. 4.3 Experimental setup. (a) Schematic showing an interdigital transducer (IDT) generating a SAW train propagating towards the single-electron circuit. (b) SEM image of the upper source quantum dot (QD), which is coupled to the quantum rail (QR) with the schematically indicated electrical connections. (c) SEM image showing the tunnel-coupled quantum rails with schematically indicated transport paths, U and L.

A SEM image of the whole single-electron circuit is shown in Fig. 4.3c. The device consists of two quantum rails having a total length of 22 μm. The transport channels are coupled along a region of 2 μm by a tunnel barrier defined by a 20-nm-wide surface gate.

This tunnel coupled region is the primary focus of my simulations since it is where critical quantum operations are performed. It is the 20 nm tunnel barrier that is responsible for the beam-splitter operation.

4.3 Time-Dependent Solutions

Using the exact device geometry from Sec. 4.2, I used the commercial software NextNano [21] to calculate the underlying electrostatic potential. Assuming that the charge density is constant across the 2DEG, it is possible to use experimental fabrication parameters to calculate the potential. Following the methods of Hou *et al.* [80], a frozen charge layer and deep boundary conditions were used. The donor concentration was calculated to be $1.6 \times 10^{10}\text{cm}^{-2}$ in the doping layer and the surface charge concentration was $1.3 \times 10^{10}\text{cm}^{-2}$. The exact fabrication parameters for this device can be found in Appendix C. This information, combined with the voltages applied to the Schottky gates, allows the potential to be calculated. The surface acoustic wave potential is superimposed over the electrostatic potential as a propagating sinusoidal wave. Using Coulomb-blockade measurements, the experimental amplitude of the SAW was estimated to 15 meV [149]. In my simulations, I varied the SAW amplitude to test for a variety of cases.

The experimental device described in Sec. 4.2 is a single-electron beam splitter. As such, an incoming electron wave function from one of the channels leaves the tunnel-coupled region in a superposition state between the upper and lower exit channels. The probability amplitude of the states in the superposition are determined by the voltage bias between gates V_U and V_L, as seen in Fig. 4.3. In a system where quantum coherence has been preserved, coherent oscillations should be observed when varying V_U and V_L. Instead, experimental observations point towards the single electrons being in a thermal equilibrium. When the detuning is $\Delta = V_U - V_L = 0$ V, the directional coupler leads to a 50-50 superposition between both channels. Alternatively, when the voltage is set such that $\Delta < 0$ V, the potential in the lower channel is more negative and pushes the electronic wave function to the upper channel. Likewise, when $\Delta > 0$ V, the wave function is more present in the lower channel.

For simplicity and since the device geometry is symmetrical, the particle is always injected from the upper left channel in my simulations. An example voltage configuration can be seen in Appendix D.

The top panel in Fig. 4.4 shows the dependence of the transfer probability in the upper or lower channel on the detuning Δ. As expected, for a large bias, the wave function is completely confined to a single channel. For an unbiased system, the quantum rails are electrostatically aligned and the superposition between both rails is equal. A concern that

is highlighted by Fig. 4.4 is the width of the probability transition. Here, it takes a change of about 200 mV for the electron to go from one channel to the other completely. For a ground-state system, this transition should be much narrower. In order for the simulations (black lines in Fig. 4.4) to match experimental results (red and blue circles), higher excited states were used. The bottom panel in Fig. 4.4 shows the energy spacing between the sites as well as their relative weight in the combined wave function. The occupation of higher energy states can be approximated with a Fermi function:

$$P_U(\Delta) \approx \frac{1}{\exp(-\Delta/\sigma)+1}, \tag{4.1}$$

where P_U is the probability of finding the particle in the upper channel and σ is some parameter related to the excitation of the electron.

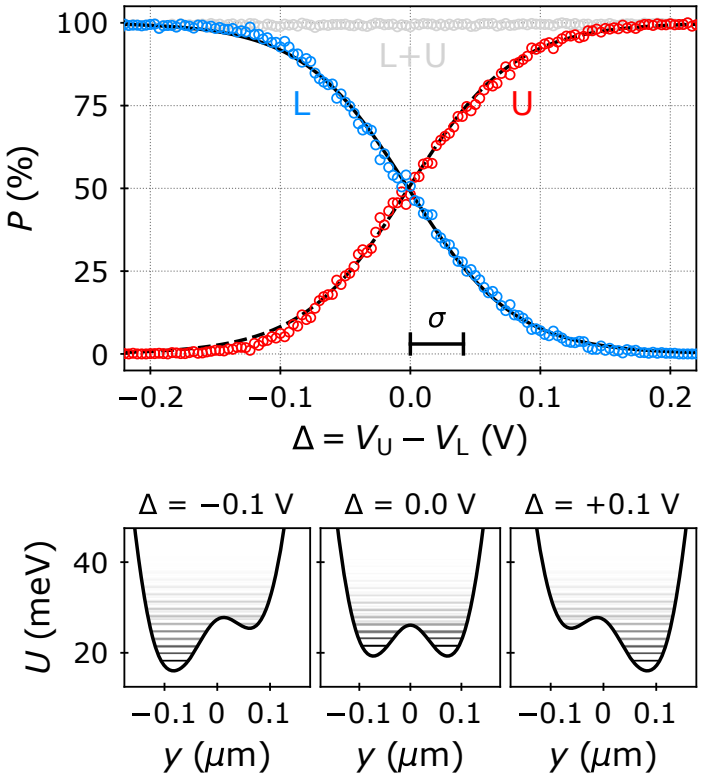

Fig. 4.4 Partitioning the wave function of an electron in flight. Top panel: Probability, P, for a single electron to end up in the upper (U) or lower (L) quantum rail for different values of potential detuning, $\Delta = V_U - V_L$. Red and blue circles indicate experimental results and the black lines show the predictions from simulations. Bottom panel: One-dimensional slices of the electric potential, U, along the double-well potential for different values of detuning. Horizontal lines indicate the instantaneous energy eigenstates of the double quantum dot. The occupation of these states to reproduce the results in the top panel is represented by the opacity of the lines.

In an ideal setting, given the device geometry, the electron wave function remains in a low energy state for the entire transport process. This ensures that the beam-splitter operation is coherent and reproducible. Given the electrostatic potential calculated, it would be expected for the transition from the upper channel to the lower channel to be rapid as the detuning $\Delta = V_U - V_L$ is swept. Furthermore, only a very specific potential landscape would lead to a single transition such as the one shown in Fig. 4.4. Coherent oscillations should cause the probability of detecting the electron in the upper or lower channel to vary multiple times between 0 and 100%. The frequency at which this transition occurs is closely related to the height of the tunnel barrier separating the two quantum rails and the voltage applied to the gate V_T.

A deviation from the ideal setting occurs when the particle is excited into higher energy states. The excited states of the electron can overcome the tunnel barrier more easily. This causes the detection of the electron in the upper or lower channel to transition over a larger range of detuning voltages. Figure 4.5 shows the transition widths for various levels of excitation. The black line represents an adiabatic transport process where the single electron remains in the instantaneous ground state of the potential at all times. It shows a very sharp transition over a small range of detuning values. As the energy of the electron is increased, the width of the transition becomes broader. The final simulated transition curve at $\varepsilon = 6.70$ meV corresponds to the the experimental data fitted in Fig. 4.4.

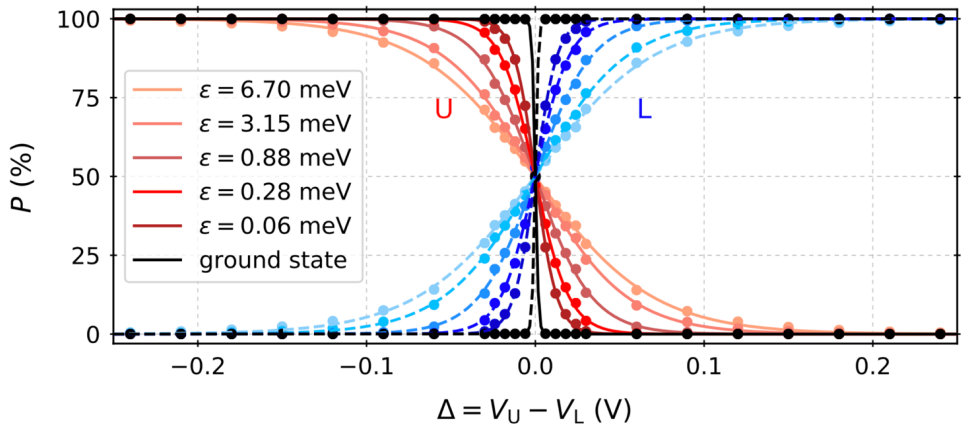

Fig. 4.5 Probability P (U and L) to find the electron in the upper and lower channels respectively as a function of the detuning $\Delta = V_U - V_L$. Each solid marker represents a time-dependent simulation outcome. The solid and dashed lines are fits using Eq. 4.1.

Here, the energy of the single electron is determined using an exponential distribution over the instantaneous eigenstates at the center of the tunnel coupled wire. Each state

contributes to the single-electron wave function with probability

$$p_i \propto \exp\left(-\frac{E_i - E_0}{\varepsilon}\right), \tag{4.2}$$

where E_i corresponds to the eigenenergy of the i^{th} excited state and E_0 corresponds to the energy of the ground state. The parameter ε serves as a label for the energy of a particular state configuration and is quoted in Fig. 4.5. The exponential state distribution in Eq. 4.2 leads to detection probability transitions that closely match experimental data. However, such a distribution does not arise simply from the propagation of the electron through the device potential. Assuming that the electron is originally in its ground state when it is picked up by the surface acoustic, the resulting state distribution after its propagation to the center of the tunnel coupled region is shown in red in Fig. 4.6. For comparison, the state distribution according to Eq. 4.2 is illustrated in black. Although the expectation value for the energy of the particle is not significantly different in both cases, the probability transition for the time-evolved excited state does not match experimental results. This is especially true when the detuning is set such that the particle should transition from the upper (lower) injection channel to the lower (upper) one. Experimentally, when the detuning is strong, this probability goes to 100%. However, time-dependent simulations show that at least part of the wave function remains in the channel with a high potential, reducing the transition probability from 100%. The match between the probability distribution given by Eq. 4.2 and experiments suggests that relaxation of the electron wave function occurs in the tunnel coupled region.

Time-dependent simulations of the SAW-driven quantum mechanical propagation of the electron are used in order to identify the source of electron wave function excitations. The change in the potential landscape causes a rapid reconfiguration of the eigenstates in the moving quantum dot leading to Landau-Zener transitions into higher energy states [103, 167]. These Landau-Zener transitions occur when there is a sharp non-adiabatic change in the potential. Since the underlying potential is static, sharp changes are determined by the geometry of the device. Kinks, bends, and the widening of the quantum channels at the injection point into the tunnel coupled region is where excitations are most likely to occur. These observations were also observed experimentally in previous investigations of SAW-driven electron transport [87]. For the device used in this chapter, there are three main areas that introduce excitations. Assuming that the single electron is initially in the upper left quantum dot (see Fig. 4.3), the first area is at the bend when the channel is angled downwards. This bend is progressive at the level of the 2DEG and does not contribute more than a 3% contribution loss of the ground state to the total wave function of the electron. The second

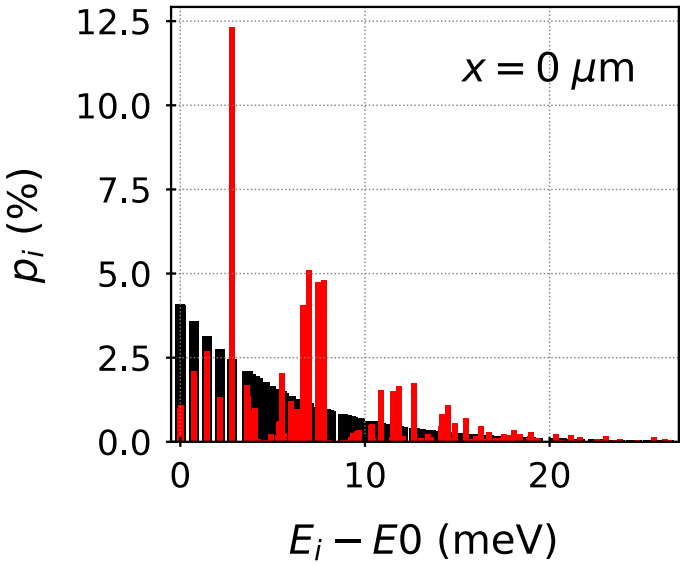

Fig. 4.6 Instantaneous energy eigenstate occupation for the time-evolved injected electron (red) and the relaxed electron wave function (black) as found using Eq. 4.2. The time evolution of the wave function for both electrons is shown in Fig. 4.7. The position $x = 0\mu$m corresponds to the center of the tunnel coupled region.

area is the entrance of the tunnel-coupled wire. Here, many Schottky gates cause an abrupt change in the electrostatic potential. Both the new angle in the direction of motion and the broadening of the channel confinement caused by the close proximity of the second channel introduce many Landau-Zener-type excitations and generate the distribution of states shown in Fig. 4.6. The third area of excitation is at the exit of the tunnel-coupled wire. Similar to the entrance, an abrupt change in the electrostatic potential shifts the angle at which the electron is travelling and restores a tight confinement. An added source of error that is present at the exit of the tunnel-coupled wire is displacement of the electron into a different SAW minimum. When the potential ramp is steeper than the SAW confinement, a part of the wave function is ejected back into the tunnelling area, over the SAW maximum. This leads to measurement time delays. A brief discussion on time-of-flight measurments is found in Sec. 4.4.2. Figure 4.7 shows the time evolution of the single-particle wave function.

I do not consider the final bend in the exit channel, just before the reciever quantum dot, as a source of error since any further excitation introduced at that location do not affect the probabilities of detecting the electron in either channel. Since the bend is not sharp enough to cause the electron to hop to a different SAW minimum, it does not affect the measurement outcome. Nevertheless, Landau-Zener transitions introduced in this region would need to

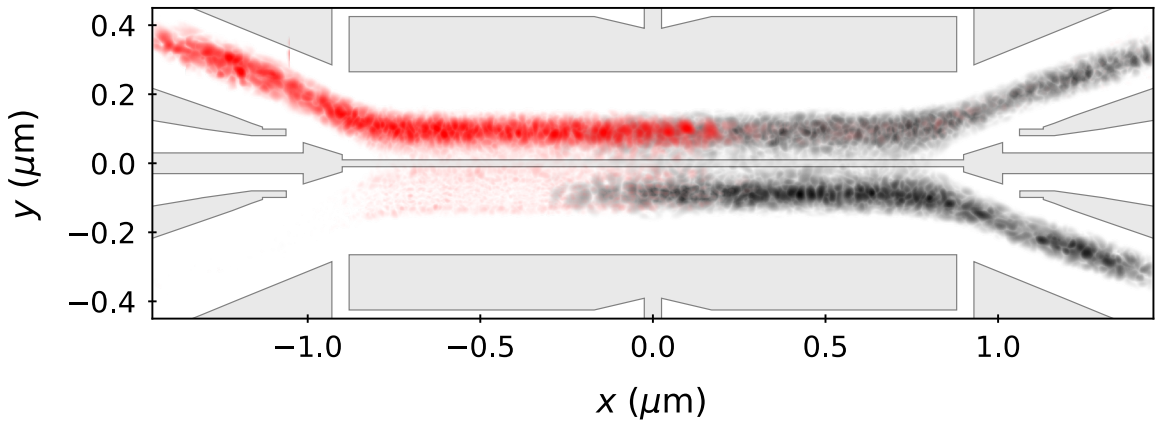

Fig. 4.7 Single-electron wave function propagation in the directional coupler. Surface-gate voltages are set such that the electrostatic potential is symmetric with no detuning ($\Delta = 0$. Initially, the particle in located in the upper left channel and is carried by a surface acoustic wave across the device. The wave function is illustrated in red. Somewhere in the tunnel coupled region, the electron is assumed to have relaxed to a lower energy state. The wave function for the relaxed state is shown in black. A comparison between the instantaneous energy eigenstates of the injected and relaxed wave function can be seen in Fig. 4.6. The relaxed wave function continues to propagate, creating a 50-50 superposition between the upper and lower exit channels.

be taken into account if such a beam splitter was linked to other devices carrying out more quantum operations.

4.4 Discussion

In this chapter, I investigated the accurate control of a single electron and the quantum information it carries. I performed simulations of realistic single-electron transport in semiconductor devices and compared the results to experimental observations. Although high-efficiency single-electron transport is possible for surface-acoustic-wave systems, the coherence of the quantum states is not fully preserved. The two main error mechanisms observed here are unwanted excitations in regions where the electrostatic potential varies sharply and relaxation of these excited states. Both contribute to the loss of coherent oscillations and ultimately the degradation of quantum state fidelity. By simulating different configurations, it is possible to find ways to mitigate these error mechanisms and recover coherent processes.

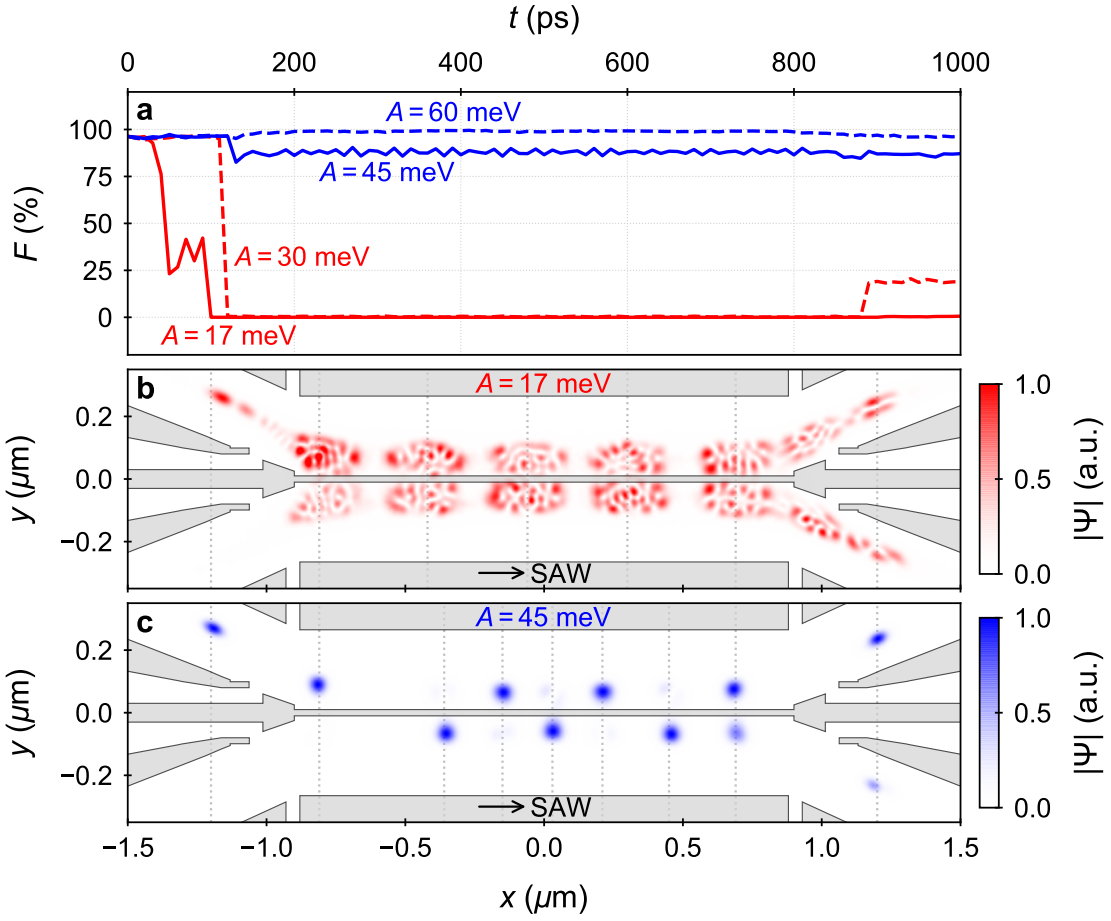

Fig. 4.8 The effects of SAW amplitude on excitations of the single-electron wave function. **(a)** Qubit fidelity as the electron propagates across the tunnel-coupled wire. For higher SAW amplitudes, the fidelity remains close to 100%. **(b)** Single-electron wave function at selected times (grey dashed vertical lines) when carried by a SAW with a 17 meV amplitude. This corresponds to the estimated SAW amplitude used experimentally. **(c)** Single-electron wave function at selected times (grey dashed vertical lines) when carried by a SAW with a 45 meV amplitude. Coherent oscillations between the upper and lower channel are observed.

4.4.1 Minimising Errors

Simulations of the transport process revealed that the main source of charge excitation is located at the entrance of the tunnel-coupled wire. In Sec. 4.3, I discussed the causes of excitations and determined that the bend in the channel's direction does not contribute significantly to altering the wave function of the electron. Excitations here arise from the abrupt lowering of the electrostatic potential in addition to the widening of the confinement within the channel. A carefully tailored tunnel barrier can ensure that the confinement change is gradual. To minimise the effect of the potential drop, a larger SAW amplitude can increase the particle confinement. Figure 4.8 shows a comparison of the single-electron transport process using different SAW amplitudes. The fidelity in panel (a) is defined as the overlap between the electron wave function and the instantaneous ground state and first excited state within the moving double quantum dot. A SAW amplitude of 17 meV, as is used in experiments, is insufficient to maintain a consistent confinement of the electron and the fidelity drops to near 0 % as the particle enters the tunnel-coupled wire. The excitations caused by the electrostatic potential are further illustrated in panel (b), which shows the electron wave function at several timestamps. Although a 50-50 superposition is created by the directional coupler, this device does not act as a quantum beam splitter. The charge state is not preserved and a repeated operation does not collimate the electron wave function into one channel. Using the same device geometry as well as the same surface-gate voltages, it is possible to recover coherent behaviour by increasing the SAW amplitude. Panel (c) in Fig. 4.8 shows that the wave function of the particle remains in its lower energy states and oscillates periodically between the two channels. It is important to note that although the potential and gate voltages are symmetric, the outcome of the beam-splitter is not a 50-50 superposition. This is because in the presence of coherent oscillations, the probability of measuring an electron in the upper or lower exit channel does not only depend on the detuning between the two, but also the phase of the oscillations. Here, the height of the tunnel barrier between the two channels plays an important role in determining the outcome of the directional coupler operation. In an ideal case, all gates could be held constant and only the voltage applied to the tunnel barrier gate V_T (see Fig. 4.3) would be necessary to control the transition of the single electron from the upper to the lower channel.

4.4.2 Time-of-Flight Measurements

A next step for this work, both theoretically and experimentally is to investigate the time of flight of the single electron throughout the device. Experimentally, loading an electron into a specific minimum of the SAW train via a voltage-pulse trigger was demonstrated

[149]. However, it is unclear if the electron remained in the same SAW minimum as it travelled across the semiconductor device. If the change in potential in the tunnel-coupled wire is greater than the amplitude of the SAW, the electron can escape its minimum and hop into a neighbouring one. This is especially problematic for the exit ramp out of the tunnel coupled region since the electron can be kicked back into the next SAW minimum repeatedly. Increasing the amplitude of the surface acoustic wave is once again a possible solution to increase the confinement within a single minimum. However, a large SAW amplitude cannot be used as a blanket solution to all error processes. Nanoscale devices become unstable when exposed to large modulations [64] and the loading of a single electron is impractical for large SAW amplitudes. Instead, a more careful engineering of the device geometry is required to minimise the variation of the electrostatic potential background between the tunnel-coupled wire and the injection and exit channels. Changes can include a modified device geometry or an adjusted voltage applied to surface gates.

5

Protocol for Fermionic Positive-Operator-Valued Measures

One of the benefits of studying theory and simulations is the possibility of going beyond what is currently accessible experimentally, such as the device presented in Chapter 4. A more complex circuit is useful for quantum information processing and quantum computing, but also allows the study of foundational questions. In this chapter, I present a more fundamental examination of the quantum behaviour of electrons.

Since its inception, the field of quantum mechanics has produced many interesting and often counterintuitive results. Although quantum theory has been extensively studied, there are still many aspects of the theory that are heavily debated. Not only do different interpretations of quantum mechanics cause lots of controversy, but the measurement process itself is often misunderstood. In quantum physics, a state is represented by a wave function, a complex-valued probability amplitude describing the physical properties of a system. Many physicists even question the existence of the wave function in physical reality, but this is an ontological question which beyond the scope of this thesis. The work in this chapter follows closely the publication generated in Phys. Rev. A 101, 022329 (2020) [8].

Consider a general wave function $|\psi\rangle$ and an associated observable M. An observable could be, for example, the spin of an electron or the polarisation of a photon, i.e. a measurable property of the system in study. If we were to measure the observable M of $|\psi\rangle$, we would find the output in one of the orthogonal eigenstates $|M_i\rangle$ of the measurement observable. In the Copenhagen interpretation of quantum mechanics, this is described by the "collapse" of the wave function onto one of the possible measurement outcomes. This definition of measurements is called *projective measurements* or *Von Neumann measurements* and has been shown to be too restrictive. Projective measurements fail to describe a broad range of fascinating quantum phenomena including non-demolition [24], weak [3], and continuous [50] measurements. For a more generalised theory of quantum measurement, one can use a positive-operator-valued measure (POVM).

5.1 Positive-Operator-Valued Measures

In projective measurement theory, an observable M has an associated operator $\hat{M}_i$, which is written in terms of its eigenvectors $|i\rangle$ and eigenvalues λ_i as

$$\hat{M} = \sum_{i=1}^{N} \lambda_i |i\rangle \langle i| . \tag{5.1}$$

The eigenvectors $|i\rangle$ form a complete orthonormal basis. A single projective measurement operator is defined as $\hat{M} = |i\rangle \langle i|$. Each projective measurement operator has an associated outcome probability, which is defined as

$$P_i = \langle \psi | \hat{M}_i^{\dagger} \hat{M}_i | \psi \rangle = | \langle i | \psi \rangle |^2 . \tag{5.2}$$

A shortcoming with the projective measurement is that a detector, or measurement device, cannot distinguish between nonorthogonal states using a single measurement. Consider an initial state that is in an arbitrary superposition of two states $|u\rangle$ and $|v\rangle$,

$$|\psi_0\rangle = (\alpha |u\rangle + \beta |v\rangle) |M_0\rangle . \tag{5.3}$$

Here, $|M_0\rangle$ is the state of the detector before it has interacted with the quantum state. After a measurement of M, the final state becomes

$$|\psi_f\rangle = \alpha |u\rangle |M_u\rangle + \beta |v\rangle |M_v\rangle . \tag{5.4}$$

Since both $|\psi_0\rangle$ and $|\psi_f\rangle$ must be normalised, we have that

$$\langle\psi_0|\psi_0\rangle - \langle\psi_f|\psi_f\rangle = 0 \tag{5.5}$$

and therefore

$$\alpha^\dagger\beta\,\langle u|v\rangle\,(1-\langle M_u|M_v\rangle) - \alpha\beta^\dagger\,\langle v|u\rangle\,(1-\langle M_v|M_u\rangle) = 0. \tag{5.6}$$

One way of satisfying this normalisation condition is to have the states $|u\rangle$ and $|v\rangle$ be orthogonal. However, if these states are not orthogonal and $\langle u|v\rangle \neq 0$, the only way to satisfy this condition is to have the measurement outcomes of M be the same, or $\langle M_v|M_u\rangle = 1$. This makes it impossible for projective measurements to distinguish non-orthogonal states. It is possible to measure states in a non-orthogonal basis *sometimes* by defining a set of so-called Kraus operators $\hat{M}_i$ [118, 101], as long as they satisfy

$$I_M = \sum_{i=1}^{N} \hat{M}_i^\dagger \hat{M}_i. \tag{5.7}$$

The outcome of a POVM with $\hat{M}_i$ is the normalised state

$$|\psi_i\rangle = \frac{\hat{M}_i\,|\psi\rangle}{\sqrt{\langle\psi|\,\hat{M}_i^\dagger\hat{M}_i\,|\psi\rangle}}, \tag{5.8}$$

with probability

$$P_i = \langle\psi|\,\hat{M}_i^\dagger\hat{M}_i\,|\psi\rangle\,, \tag{5.9}$$

where $\langle\psi_i|\psi_j\rangle \neq \delta_{i,j}$. This allows the POVM to distinguish non-orthogonal states. However, there is a possibility that the POVM yields no information at all. A POVM is a tool that allows the investigation of some of the strangest quantum phenomena and provides information about a system that normal projective measurements could never uncover [118].

5.1.1 Ahnert & Payne POVM

A variety of techniques have been proposed [13, 4, 5] and demonstrated [164, 15] for POVMs in optical systems. A breakthrough in the development of implementable POVMs was made by S. E. Ahnert and M. C. Payne at the Cavendish Laboratory (AP POVMs) [4, 5]. They made POVMs accessible to optics technologies based on single-photon polarisation states. Their proposal described a single setup for the general implementation of POVMs. The AP POVM implementation consists of two nested polarising Mach-Zehnder interferometers which are

joined by polarising beam splitters. Local operations are performed on the polarisation state of the photon qubit in the different arms of the interferometer using electro-optical phase modulators, wave plates, and mirrors, as shown in Fig. 5.1.

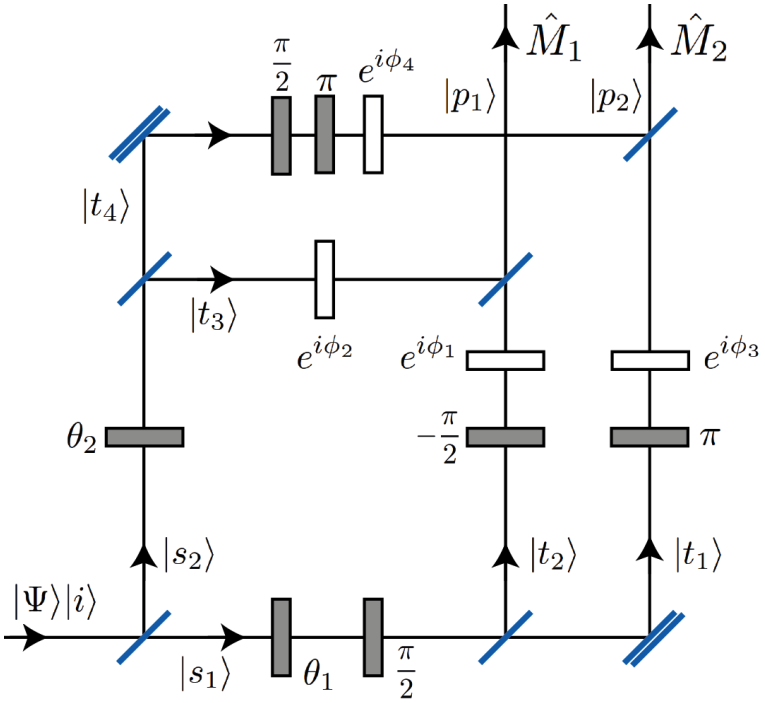

Fig. 5.1 AP POVM from reference [4]. Qubit rotations of the POVM are denoted by shaded rectangles, the phase shifts by open rectangles and the spatial degrees of freedom by the states $|i\rangle$, $|s_{1,2}\rangle$, $|t_{1,2,3,4}\rangle$ or $|p_{1,2}\rangle$. Single and double diagonal lines indicate polarizing beam-splitters and reflecting mirrors respectively.

A photon entering the system with a polarisation state $|\Psi\rangle = \alpha|0\rangle + \beta|1\rangle$ leaves the interferometer in a superposition of spatial states:

$$\sum_j |\Psi_j\rangle |p_j\rangle = \sum_j \hat{M}_j |\Psi\rangle |p_j\rangle, \tag{5.10}$$

where

$$\hat{M}_1 = \cos(\theta_1) e^{i\phi_1} |0\rangle\langle 0| + \cos(\theta_2) e^{i\phi_2} |1\rangle\langle 1|, \tag{5.11a}$$

$$\hat{M}_2 = \sin(\theta_1) e^{i\phi_3} |0\rangle\langle 0| + \sin(\theta_2) e^{i\phi_4} |1\rangle\langle 1| \tag{5.11b}$$

are the Kraus operators of the POVM. The states $|p_1\rangle$ and $|p_2\rangle$ denote the spatially decoupled output paths such that a specific Kraus operation is performed on the polarisation state of the photon, conditioned on whether the photon exits the interferometer from output $|p_1\rangle$ or $|p_2\rangle$. Non-diagonal Kraus operators can be created by applying unitary operations to the

input and outputs of Fig. 5.1. Note that generally $\hat{M}_1\hat{M}_2|\Psi\rangle \neq 0$ and $\hat{M}_1\hat{M}_1|\Psi\rangle \neq \hat{M}_1|\Psi\rangle$. As discussed in 5.1, the operators are not necessarily orthogonal and a POVM is different from a projective operation. Whilst the Kraus operators must satisfy:

$$\sum \hat{M}_i^\dagger \hat{M}_i = \hat{1}, \tag{5.12}$$

the individual Kraus operators, $\hat{M}_i$, are not necessarily unitary. In the rest of this chapter, I will expand the AP POVM to include fermionic particles with non-zero mass. The protocol described here is useful to many quantum information systems that use electrons as their physical platform. Furthermore, current semiconductor devices, such as the one decribed in Chapter 4 can be chained to create a POVM.

5.2 Unitary evolution of a massive particle

The interferometric scheme presented in Sec. 5.1.1 provides a template for demonstrating POVMs using photons. However, similar techniques can be applied to perform general measurements in quantum systems based on electrons. In this section, I will map the AP POVM to a fermionic system. To do so, I present processes which describes the individual unitary operations shown in Fig. 5.1 for spin-$\frac{1}{2}$ qubits in semiconductor heterostructures. Together, these processes form a toolkit allowing coherent particle propagation, spin rotations and spin-dependent particle translation on massive particles.

The transformation of spatial propagation from photonic to fermionic states is not straightforward. Whilst a photon can pass through free space without dispersing significantly, the wave function of a massive particle – such as an ion or an electron – will disperse. Most optical devices, including the polarising Mach-Zehnder Interferometer (MZI), rely on self-interference of spatially well-defined qubit states. These systems are especially sensitive to dispersion since repeated operations will not lead to the same outcomes. Figure 5.2 shows a staggered leapfrog time-evolution for the wave packet of a massive particle passing through a MZI. Spin-dependent beam splitters are inserted at the junctions. The device curvature as well as the initial wave packet shape and momentum distribution are chosen to maximise the output probability density in the upper exit port of the MZI (labelled by b_1 in Fig. 5.2). Nevertheless, over 5% of the probability density disperses to unwanted locations of the MZI and the shape of the wave packet is significantly distorted. This places an upper bound of 95% on the spin-qubit fidelity of a single polarising MZI. Additionally, the AP POVM relies on the spatial separation of the output states and any distortion of the spatial wave packet inhibits optimal control. The dramatic reduction in the fidelity of the qubit operation presents

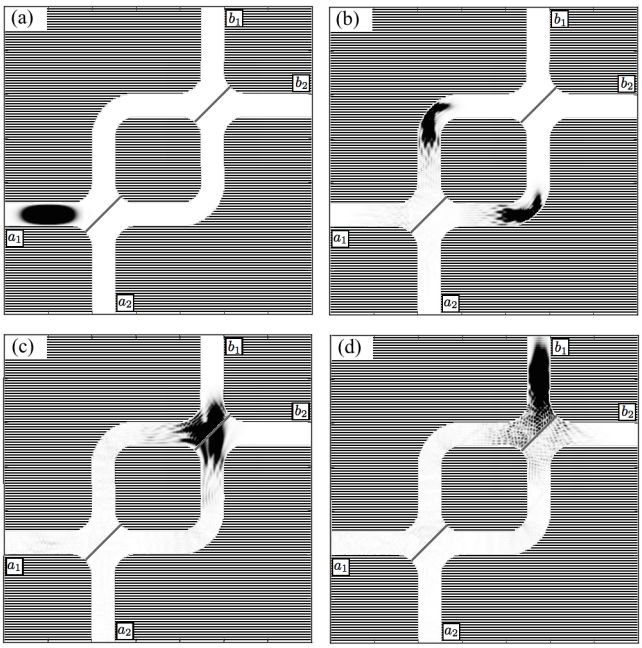

Fig. 5.2 Mach-Zehnder interferometer for free massive particles at four different time steps. The potential is infinite in the striped area and zero elsewhere. The beam-splitters of the MZI are indicated with grey diagonal lines.

a challenge for the implementation of quantum protocols, highlighting the need for a more sophisticated approach.

In order to successfully replicate the AP POVM presented in Fig. 5.1 using massive particles, three main requirements must be satisfied. First, the particle must match the free dispersiveless propagation of a photon through the interferometer. Second, qubit rotations, such as the arbitrary polarisation rotations using a combination of birefringent wave plates, must be possible. Third, the wave function of the particle must be spatially separated like the photon, which is split into a pair of polarised modes using polarising beam splitters.

5.2.1 Dispersion-free propagation

To satisfy the first condition using massive particles, the dispersion of the states has to be eliminated. This can be obtained with Gaussian wave packets in harmonic confining potentials. Such potentials have been used successfully in ion traps to perform coherent diabatic ion transport [23, 81], but equivalent potentials can be achieved in semiconductors by either electrostatically defining quantum dots using Schottky surface gates [87, 45, 153, 157] or lithographically confining charges in doped regions separated by tunnel barriers [59]. Using the staggered leapfrog algorithm presented in Chapter 2, simulations confirm that spatial propagation can be obtained in a manner that both preserves the fidelity of the

operation and keeps the shape of the wave packet intact. There are two main ways of preventing dispersion. First, the minima of the harmonic potentials can be shifted, displacing the wave packet and generating a coherent state. A rapid update of the underlying potential puts the wave function in a coherent state that is displaced from the ground state. The wave packet oscillates about the new potential minimum and can be coherently displaced to a new spatial location. Secondly, by moving the minima of the harmonic potentials in an adiabatic manner, it is possible to preserve the structure of the ground state whilst the qubit is transported between the optical component analogues. In this work, I found that an optimal way to adiabatically transport electrons non-dispersively is to use propagating SAW potentials. A ground-state electron (near Gaussian) trapped in the minimum of a sinusoidal SAW potential is transported coherently through the device at the propagation speed of the SAW. As discussed in Chapters 2, 3, and 4, the underlying potential can be defined by Schottky gates at the surface of a semiconductor device. This underlying potential adiabatically shifts the center of mass of the ground state in the SAW frame of reference, which effectively enables linear-optics like spatial control of the electron qubits.

5.2.2 Arbitrary Qubit Rotations

Arbitrary polarisation rotations for spin-$\frac{1}{2}$ particles can be described by time-ordered unitary operators:

$$\hat{R}_{\hat{k}} = \mathscr{T} \exp\{\left[i\lambda(t)\sigma_{\hat{\boldsymbol{k}}}t\right]\}, \tag{5.13}$$

where $\lambda(t)$ is some time-dependent strength parameter and $\sigma_{\hat{\boldsymbol{k}}}$ are the Pauli matrices. Such unitary operations can be realised using a magnetic field with the Hamiltonian

$$\hat{H}_{rot} = -\boldsymbol{\mu} \cdot \boldsymbol{B}(t), \tag{5.14}$$

where $\boldsymbol{\mu}$ is the magnetic dipole moment of the particle and the magnetic field $\boldsymbol{B}(t)$ is uniform over the particle wave packet [111, 67]. Spin-rotations of SAW qubits have been studied in previous works [12]. Charged qubits moving in a magnetic field naturally experience a Lorentz force. However, for SAW carried electrons in semiconductor heterostructures, this force is counteracted greatly by the device confinement [122, 121]. Electromagnetic corrections can also be applied as suggested in *Phys. Rev. B 62, 8410 (2000)* [12]. Other techniques for spin rotations include using a DC magnetic field to lift the spin degeneracy and applying an oscillating perpendicular magnetic field set in resonance between the two spin states [10]. Yet another technique uses electron spin resonance (ESR), where a pulse of microwaves becomes resonant with the upper and lower Zeeman-split spin states [89].

5.2.3 Spin Polarisation

Although solid-state physics present several possibilities to select the spin of an electron (Pauli blockade [125] or spin filtering [124]), implementing a spin splitter is difficult in practice, owing to the generally small dimensions of devices and the intrinsic nature of the spin. However, several structures, materials or techniques can be used to channel dedicated spin orientations.

Antidots [168] or quantum spin hall systems [88] are commonly used to create spin-polarised channels at the edges of structures with a minimum number of gates and simplified geometry. These have been realised in graphene [148] but also in semiconductors. More generally, it is possible to utilise materials with strong spin-orbit interaction to generate spin currents out of charge current. Another approach is to scatter the wave packet off of a narrow magnetic semiconductor barrier, such as europium oxide (EuO) [132, 40, 76], which acts as a spin filter, only transmitting a specific electron spin polarisation. Furthermore, new types of materials, like topological insulators, possess intrinsic properties that allow locking spin states to specific transport directions [96]. Finally, there exist a number of schemes for the projective measurement of fermion spin [84, 12, 141, 110, 68, 55, 160]. These schemes implement spin-dependent translations of the qubits followed by a single particle charge readout. Technologies for projective spin measurements are based on magnetic readout (utilising the spin-valve effect), double occupation readout (utilising spin-dependent tunneling) or Stern-Gerlach readout.

5.3 Example POVM

In this section, a POVM is implemented on a single-electron spin-$1/2$ qubit with an initially arbitrary spin polarisation. In this case, the massive wave packet undergoes Procrustean entanglement distillation, which transforms an arbitrary entanglement state into a pure Bell pair. Procrustean entanglement distillation is discussed further is Sec. 5.4. The single particle subject to the POVM is one part of a joint initial state of the form

$$|\Psi_{A,B}\rangle = \cos(60^\circ)\,|{\downarrow_A}\rangle\,|{\downarrow_B}\rangle + i\sin(60^\circ)\,|{\uparrow_A}\rangle\,|{\uparrow_B}\rangle\,. \tag{5.15}$$

The spatial degree of freedom is labelled by $|i\rangle$, $|s_{1,2}\rangle$, $|t_{1,2,3,4}\rangle$ and $|p_{1,2}\rangle$, as in Fig. 5.1. An underlying potential is necessary in order to achieve the confinement necessary for the double interferometer. It can be implemented with Schottky gates, as described above, or by etching the semiconductor material. The contour lines in Fig. 5.3 show such an electrostatic potential. The pattern produced by applying voltages to the Schottky gates defines the circuit

along which the single-particle wave function is confined. A sinusoidal surface acoustic wave carried the electron across the device and maintains a constant confinement along the direction of motion. The SAW potential is not included in Fig. 5.3.

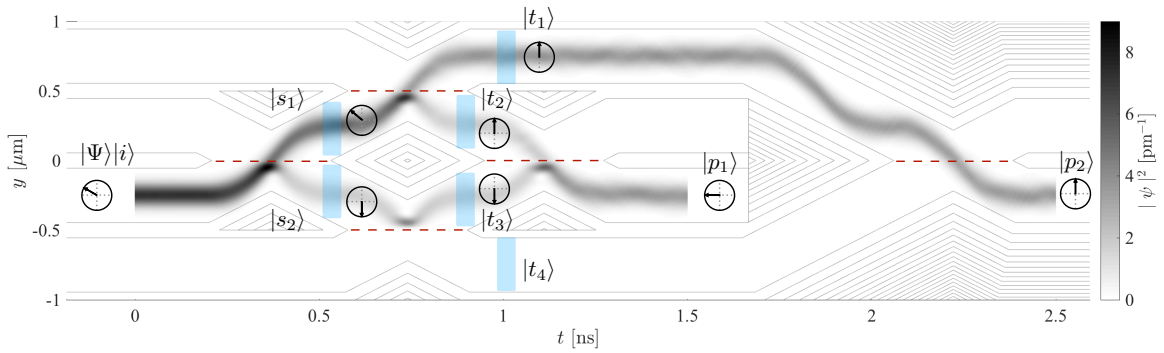

Fig. 5.3 Simulation of a massive wavepacket travelling through a POVM device. The paths $|s_1\rangle$, $|s_2\rangle$, $|t_1\rangle$, $|t_2\rangle$, $|t_3\rangle$, $|t_4\rangle$, $|p_1\rangle$, and $|p_2\rangle$ correspond to those from Fig. 5.1. The electrostatic potential of the proposed semiconductor device is represented by grey contour lines. Dashed lines indicate the position of the spin beam-splitters. After each beam-splitter, a magnetic field, represented by the shaded areas, is applied for spin rotations according to Fig. 5.1. The arrow in the projected Bloch spheres indicate the wavefunction's spin orientation in their respective regions. In the simulation presented, the electron wave function is split with equal probability between the $|p_1\rangle$ and $|p_2\rangle$ outputs.

In Fig. 5.3, the two-dimensional electron wave function is traced out in the x dimension. The plot shows the probability distribution in the y dimension as a function of time, t. Because of the strong confinement of the SAW potential, the particle distribution and movement in the x direction is minimal. Hence, the particle's position in x can be accurately estimated by $x = v \cdot t$, where v is the speed of sound in the material.

The electron initially exists in the ground state of the SAW minimum, in the spatial state $|i\rangle$. The direction of motion is changed, and it is incident on the first polarising beam splitter. Here, the electron is split into its spin components in a superposition of the spatial states $|s_1\rangle$ and $|s_2\rangle$. Two magnetic fields are applied to the respective components indicated by the shaded areas in Fig. 5.3. $|s_1\rangle$ and $|s_2\rangle$ are then incident on two more splitters forming a new superposition of the states $|t_1\rangle$, $|t_2\rangle$, $|t_3\rangle$, and $|t_4\rangle$. $|t_4\rangle$ is not occupied for this specific POVM. Again, magnetic fields (shaded areas) are applied to implement local phase shifts and spin-rotations on the individual spatial components of the electron. Following these magnetic fields, the spatial components $|t_2\rangle$ and $|t_3\rangle$ are interfered on a beam-splitter, forming an output component $|p_1\rangle$. Similarly, $|t_1\rangle$ and $|t_4\rangle$ are interfered to form $|p_2\rangle$. Hence, Fig. 5.3 shows how an input wave function $|\psi_A\rangle|i\rangle$ is transformed into a spatial superposition given by $\hat{M}_1|\psi_A\rangle|p_1\rangle + \hat{M}_2|\psi_A\rangle|p_2\rangle$.

In a 2D structure, $|p_1\rangle$ has to be trapped in a quantum dot such that $|t_1\rangle$ and $|t_4\rangle$ can evolve around it. However, recent successes in creating rolled-up semiconductor nanotubes [127, 134, 28] and layered quantum well structures [102, 143, 41] would allow output arms to continue to evolve through space, by enabling periodic boundary conditions, and finite 3D movement respectively. For certain applications, such as entanglement distillation presented here, there is no need to preserve both outputs. Only the output involving the pure Bell pair should be preserved and other outputs can be discarded via post selection.

By utilising the stability of a wave packet carried by a SAW, and by optimising the device parameters, my simulations are able to demonstrate experimentally achievable high fidelity POVMs. In this example, the Hamiltonian was tailored to provide a total POVM fidelity of $> 99.5\%$. This, however, is not an upper bound since further parameter optimisation could lead to even greater fidelities. Moreover, whilst this example demonstrated a specific implementation, the extension to a general POVM with more than two Kraus operators is straightforward [5]. Nested polarising Mach-Zehnder interferometers can be connected together by inserting the output states at $|p_1\rangle$ and $|p_2\rangle$ into subsequent interferometers in order to generate a POVM with any combination of Kraus operators.

5.4 Procrustean Entanglement Distillation

As presented in Sec. 5.3, one use of POVMs is found in the implementation of Bennett's Procrustean entanglement distillation [17]. This protocol allows a subset of pure state qubit pairs to be discarded from a weakly entangled ensemble, such that the remaining particle pairs are more entangled. Significantly, Bennett's method can be *local* and *non-iterative* as the entanglement distillation is achieved through the application of a single POVM on only one of the particles.

For the arbitrarily entangled state,

$$|\Psi_{\mathrm{A,B}}\rangle = \alpha\,|0_{\mathrm{A}}\rangle|0_{\mathrm{B}}\rangle + \beta\,|1_{\mathrm{A}}\rangle|1_{\mathrm{B}}\rangle\,, \tag{5.16}$$

shared between, say, Alice and Bob, Procrustean entanglement distillation is achieved by applying a POVM to just Alice's particle. This POVM creates the maximally entangled Bell state:

$$|\Psi_{\mathrm{A,B}}\rangle = \frac{1}{\sqrt{2}}\Big(\,|0_{\mathrm{A}}\rangle|0_{\mathrm{B}}\rangle \pm |1_{\mathrm{A}}\rangle|1_{\mathrm{B}}\rangle\,\Big). \tag{5.17}$$

with probability

$$P_{\mathrm{dist}} = 2\left[1 - \max(|\alpha|^2, |\beta|^2)\right]. \tag{5.18}$$

The parameters for the massive particle POVM can be adjusted to carry out the Procrustean entanglement distillation protocol described above. For simplicity, let's introduce two new parameters φ and γ. For a known initial state of the form of Eq. 5.16, these new parameters are set such that

$$\alpha \equiv \cos(\varphi) \tag{5.19}$$

and

$$\beta \equiv \exp(i\gamma)\sin(\varphi). \tag{5.20}$$

The POVM parameters are set according to Table 5.1. Alice inserts a detector at the $|p_2\rangle$ output and passes her particle through the POVM. The wave function output at $|p_1\rangle$, is then acted on by the operator

$$\hat{M}_1^A = \tan(\varphi)\,|0\rangle\langle 0| + |1\rangle\langle 1| \tag{5.21}$$

if $k\pi - \pi/4 \leq \varphi \leq k\pi + \pi/4$ (for integer k), and

$$\hat{M}_1^A = |0\rangle\langle 0| + \cot(\varphi)\,|1\rangle\langle 1| \tag{5.22}$$

otherwise. The two-particle state is output as

$$|\Psi_1\rangle = \frac{1}{\sqrt{2}}(|1_A\rangle|1_B\rangle + |0_A\rangle|0_B\rangle) \tag{5.23}$$

with probability

$$P_1 = 1 - |\cos(2\varphi)| = 2(1 - \max(|\alpha|^2, |\beta|^2)). \tag{5.24}$$

The choice of these parameters allows Alice to locally distill the entanglement she shares with Bob by passing her particle ensemble through the device in Fig. 5.1. The successful creation of a Bell state at the $|p_1\rangle$ output can be heralded by the lack of detection of a particle at the $|p_2\rangle$ output.

ϕ_1	0
ϕ_2	0
ϕ_3	$-\gamma$
ϕ_4	$-\gamma$
θ_1	$\mathrm{Re}\{[\arccos(\tan(\varphi))]\}$
θ_2	$\mathrm{Re}\{[\arccos(\cot(\varphi))]\}$

Table 5.1 POVM parameters for the implementation of entanglement distillation of the state in Eq. 5.16.

5.5 Discussion

In this chapter, I developed a methodology for the implementation of massive spin-$1/2$ qubit POVMs. The POVM builds on the framework of the AP double interferometer POVM [4]. This toolkit effectively translates the optical components from the AP POVM into processes which are suitable for electrons in surface acoustic wave systems. The use of ground-state wave functions of SAW minima eliminates the dispersion of the particle wave packets. Owing to the difficulty in controlling photon-photon interactions, linear-optics-like processing of massive (more easily interacting) particles is valuable for quantum computational aspirations or quantum cryptography with hybrid systems.

The Procrustean distillation protocol presented here assumes that the initial pure state is known. Experimentally, it is likely that processes which produce entangled massive states produce ensembles of particle pairs with a distribution of entanglement strengths. Whilst there exist theoretical methods for the entanglement distillation and purification of mixed states [18, 116, 123], these methods are iterative and require two-qubit operations. Owing to the experimental difficulties in the application of such operations, it is valuable to investigate the effect of the non-iterative single-qubit protocol on realistic particle pair ensembles. By selecting a subset of the particles from the ensemble, one can optimise the POVM configuration to maximise the entropy of entanglement of the pairs in the final ensemble. The subset of particles used in the optimisation is consumed. However, the remaining ensemble can pass through the optimised POVM, in order to generate a reduced ensemble of higher pairwise entanglement.

6

ENTANGLEMENT GENERATION VIA THE $\sqrt{SWAP}$ OPERATION

In chapters 3, 4, and 5, I discussed various ways to control single electrons, define them as qubits and perform single-qubit operations. As stated by DiVincenzo's criteria, both single-qubit operations and two-qubit operations are required for universal quantum computing. In this final results chapter, I present simulations for a realistic implementation of one of the fundamental two-qubit gates – the $\sqrt{SWAP}$ gate. The results presented in this chapter were published in 2020 in the journal *Physical Review A* under the title "Entanglement generation via power-of-SWAP operations between dynamic electron-spin qubits".[104] The simulations, analysis and discussion in this chapter were a collaborative effort between myself and Aleksander Lasek in the Cavendish Laboratory. His contributions to improve the solver to operate in momentum space were essential to the work in this chapter. It provided the numerical speedup required to sweep over simulation parameters and find accurate configurations to carry out the root-of-SWAP operation. Aleksander Lasek and I are co-authors of the publication and are listed as having contributed equally to the work.

To follow logically with the rest of the work in this thesis, I use single electrons as my qubits. These qubits are carried by a surface acoustic wave across a GaAs heterostructure. This implementation is not aimed at developing a fully SAW-driven quantum computer.

However, using this method, useful quantum operations can be performed on-the-fly while electrons are carried from one part of a quantum circuit to another. Figure 6.1 illustrates a schematic of the transport circuit. Here, electrons originally trapped by the source quantum dots labelled V_{S_1} and V_{S_2} are transported along parallel channels defined by metallic surface gates. When the potential barrier separating the two channels is low, the single electrons in the channels are allowed to tunnel through the barrier into the other channel. When only one electron is trapped in the surface acoustic wave, this device can be used as a beam splitter. The details of the single-electron beam splitter are described in Chapter 4 of this thesis. In this Chapter, I will consider the case where an electron is present in each channel. When tunnelling is allowed to occur, electron-electron interactions generate entanglement between the two particles. Here, I will discuss the process of entanglement generation using the root-of-SWAP operation.

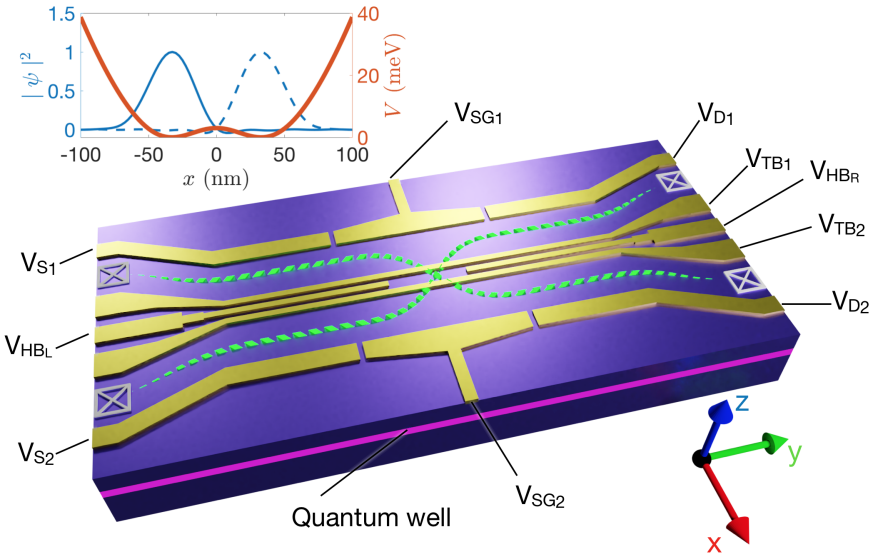

Fig. 6.1 Schematic of the power-of-SWAP device. Schottky gates (golden) are tuned to generate the electrostatic potential confinement required to obtain the desired power-of-SWAP. For simplicity, I refer to the dimension along which the operation is performed as the x-dimension and the direction of motion of the SAW as the y-dimension. The inset figure shows a cross section of the potential layout alongside a trace of the initial state of the wave function along the x-dimension. At the interaction region, the two channels are coupled by reducing the tunnel barrier height $\sim$3meV.

Using the two-qubit basis $|00\rangle, |01\rangle, |10\rangle$, and $|11\rangle$, the Power-of-SWAP operation for n^{th} power is represented by the matrix:

$$SWAP^n = \begin{pmatrix} 1 & 0 & 0 & 0 \\ 0 & \frac{1}{2}(1+e^{i\pi n}) & \frac{1}{2}(1-e^{i\pi n}) & 0 \\ 0 & \frac{1}{2}(1-e^{i\pi n}) & \frac{1}{2}(1+e^{i\pi n}) & 0 \\ 0 & 0 & 0 & 1 \end{pmatrix}. \tag{6.1}$$

For a root-of-SWAP, $n = \frac{1}{2}$ and the matrix representation is:

$$\sqrt{SWAP} = \begin{pmatrix} 1 & 0 & 0 & 0 \\ 0 & \frac{1}{2}(1+i) & \frac{1}{2}(1-i) & 0 \\ 0 & \frac{1}{2}(1-i) & \frac{1}{2}(1+i) & 0 \\ 0 & 0 & 0 & 1 \end{pmatrix}. \tag{6.2}$$

Once again, I am interested in the time-dependent dynamics of the quantum system. However, I now have to consider two particles. This effectively doubles the number of dimensions to consider and squares the size of the wave function. A simple solution to handle the increased size of the problem is to reduce it to one spatial dimension. A two-particle system of N lattice sites in 1D contains N^2 complex entries rather than N^4 as is the case in 2D. As I will show later in this chapter, this reduction to one dimension is an oversimplification that masks certain effects that are crucial to the two-particle interaction.

6.1 Hubbard Model and Exchange Interaction

To describe quantum dynamics in the device shown in Figure 6.1, I use a two-particle Hamiltonian of the form

$$\hat{H} = \sum_{i=1,2} \left(\frac{\hat{p}_i^2}{2m_i} + \hat{V}_{\mathrm{D}}(r_i) + \hat{V}_{\mathrm{SAW}}(t, r_i) \right) + \hat{V}_{\mathrm{C}}(r_1, r_2), \tag{6.3}$$

where $\hat{V}_{\mathrm{C}}(r_1, r_2)$ is the two-particle Coulomb potential, $\hat{V}_{\mathrm{SAW}}(t, r)$ is the SAW potential carrying the electrons along the channels and $\hat{V}_{\mathrm{D}}(r)$ is the eletrostatic potential created by the device itself. The potential $\hat{V}_{\mathrm{D}}(r)$ is made up of two parallel harmonic channels running along the y-dimension. These two channels are separated by a Gaussian barrier. At the center of the device, the two channels are coupled via a Gaussian tunnel barrier. Surface acoustic waves propagating in the x dimension modulate the potential and form a moving double quantum dot.

A cross section of the double quantum dot along the x dimension is illustrated in the inset of Figure 6.1. The potential barrier separating the two channels must be carefully

tuned as there exists a trade off between the spatial localisation of the electrons and the interaction between them. A high barrier separates the electrons spatially, minimising the overlap in their wave function. This is useful for single qubit control and readout operations but doesn't allow entanglement to be generated quickly. By contrast, a low potential barrier with a non-negligible overlap in the two-particle wave function lets the particles entangle quickly, but can reduce the fidelity of measurements. Since the region of measurements is not necessarily the same as the region of the exchange interaction, the issue with measurement fidelity may not be a significant problem.

Since the two-dimensional two-particle problem is computationally demanding, it is important to limit the simulation domain to a minimal number of points. Here, I use a sliding-window domain since the two-particle wave function is expected to remain confined by the double quantum dot. I can therefore focus all computational requirements on the DQD area and move the simulation domain with it, reducing the problem to that of a static DQD. By boosting the reference frame to match the velocity of the SAW, which is constant, I treat $\hat{V}_{\mathrm{SAW}}(t,r)$ as a time-independent confining potential along the channel direction.

The evolution of the two-particle state can be modelled with the Hubbard approach for short range Coulomb interaction without magnetic fields [12]. I find the eigenstates of the boosted time-independent Hamiltonian using a number basis derived from second quantization. With these states, it is possible to derive the two-particle wave functions when the barrier between both channels is static. Using second quantisation, the full set of basis states of the system with two spin-1/2 fermions occupying i^{th} and j^{th} out of N spatial sites respectively, is given by

$$\begin{aligned}
|\uparrow\uparrow\rangle_{ij} &= c^{\dagger}_{i\uparrow}c^{\dagger}_{j\uparrow}|0\rangle\,, \qquad i \neq j,\\
|\downarrow\downarrow\rangle_{ij} &= c^{\dagger}_{i\downarrow}c^{\dagger}_{j\downarrow}|0\rangle\,, \qquad i \neq j,\\
|\uparrow\downarrow\rangle_{ij} &= c^{\dagger}_{i\uparrow}c^{\dagger}_{j\downarrow}|0\rangle\,,\\
|\downarrow\uparrow\rangle_{ij} &= c^{\dagger}_{i\downarrow}c^{\dagger}_{j\uparrow}|0\rangle\,.
\end{aligned} \tag{6.4}$$

The fermionic creation operators obey the anticommutation relation $\{c^{\dagger}_{is_1}, c^{\dagger}_{js_2}\} = 0$. Therefore, the basis states are also related by $|\downarrow\uparrow\rangle_{ij} = -|\uparrow\downarrow\rangle_{ji}$. With $N = 2$, the basis states of the Hubbard two-site model are obtained analytically. The simplified two-site Hamiltonian

in the second quantisation basis from Eq. 6.4 has the form

$$\hat{H} = \begin{pmatrix} V & 0 & 0 & 0 & 0 & 0 \\ 0 & V & 0 & 0 & 0 & 0 \\ 0 & 0 & 0 & 0 & -t_{\mathrm{LR}} & -t_{\mathrm{LR}} \\ 0 & 0 & 0 & 0 & t_{\mathrm{LR}} & t_{\mathrm{LR}} \\ 0 & 0 & -t_{\mathrm{LR}} & t_{\mathrm{LR}} & U & 0 \\ 0 & 0 & -t_{\mathrm{LR}} & t_{\mathrm{LR}} & 0 & U \end{pmatrix}, \tag{6.5}$$

where t_{LR} is the hopping term

$$t_{\mathrm{LR}} = {}_{\mathrm{L}}\langle\uparrow| \frac{\hat{p}^2}{2m} |\uparrow\rangle_{\mathrm{R}} = {}_{\mathrm{L}}\langle\downarrow| \frac{\hat{p}^2}{2m} |\downarrow\rangle_{\mathrm{R}}, \tag{6.6}$$

U is the on-site energy

$$U = \frac{e^2}{4\pi\varepsilon} {}_{\mathrm{LL}}\langle\uparrow\downarrow| \frac{1}{r} |\uparrow\downarrow\rangle_{\mathrm{LL}} = {}_{\mathrm{RR}}\langle\uparrow\downarrow| \frac{1}{r} |\uparrow\downarrow\rangle_{\mathrm{RR}}, \tag{6.7}$$

and

$$V = \frac{e^2}{4\pi\varepsilon} {}_{\mathrm{LR}}\langle\uparrow\uparrow| \frac{1}{r} |\uparrow\uparrow\rangle_{\mathrm{LR}} = {}_{\mathrm{LR}}\langle\downarrow\downarrow| \frac{1}{r} |\downarrow\downarrow\rangle_{\mathrm{LR}}. \tag{6.8}$$

Solving the eigenvalue problem for the Hamiltonian in Eq. 6.5 gives the eigenenergies associated with the singlet and triplet states and defines the frequency of the SWAP operation in terms of U and t_{LR}:

$$J = \frac{1}{4\pi\hbar}\left(-U + \sqrt{U^2 + 16t_{\mathrm{LR}}^2}\right) = \frac{E_{\mathrm{T}} - E_{\mathrm{S}}}{2\pi\hbar}. \tag{6.9}$$

Initially, the electrons in both channels of the device in Fig. 6.1 are assumed to be in a separable spin state. At this stage, there is a high potential barrier between the channels and the particles are too far apart to interact. Let us also assume they are in eigenstates of the z-axis spin. The spin part of the wave function can thus be labelled $|s_1\rangle|s_2\rangle$, meaning that the first electron is in the spin state s_1, and the second one is in the spin state s_2. For a double-dot potential, the two-particle ground state is symmetric in spatial coordinates, described by a spatial wave function $|\Psi^{\mathrm{S}}(r_1, r_2)\rangle$, while the first excited state is anti-symmetric, with a spatial wave function $|\Psi^{\mathrm{A}}(r_1, r_2)\rangle$. The spin-antisymmetric combination is called a singlet state $|\mathrm{S}\rangle$, which corresponds to the ground state with energy E_{S}, and the symmetric state is called a triplet state $|\mathrm{T}\rangle$, corresponding to the first excited state with energy E_{T}:

$$|\mathrm{S}\rangle = \frac{1}{\sqrt{2}} |\Psi^{\mathrm{S}}(r_1, r_2)\rangle \left(|\uparrow\rangle|\downarrow\rangle - |\downarrow\rangle|\uparrow\rangle\right) \tag{6.10}$$

$$|\mathrm{T}\rangle = \frac{1}{\sqrt{2}} |\Psi^{\mathrm{A}}(r_1, r_2)\rangle \left(|\uparrow\rangle|\downarrow\rangle + |\downarrow\rangle|\uparrow\rangle\right). \tag{6.11}$$

Figure 6.2 illustrates these basis states and how they can be combined to form a localised qubit. A linear combination of the spatially symmetric and antisymmetric states $|\Psi^{\mathrm{S}}\rangle$ and $|\Psi^{\mathrm{A}}\rangle$ generates $|\Psi^{\mathrm{LR}}\rangle$, a two-particle state where the first particle is located on the left (L) and the second on the right (R). Here, the left and right channels are defined as the region where x is negative and positive respectively, taking $x = 0$ to be between the two channels. In panels (a), (b), and (c), the y dimension has been traced out and the axes labels x_1 and x_2 refer to the spatial extent in the x dimension of the wave function of particles 1 and 2 respectively. In panel (d), it is the x dimension that is traced out. These dimensions relative to the device and one-dimensional potential are shown in Fig. 6.1.

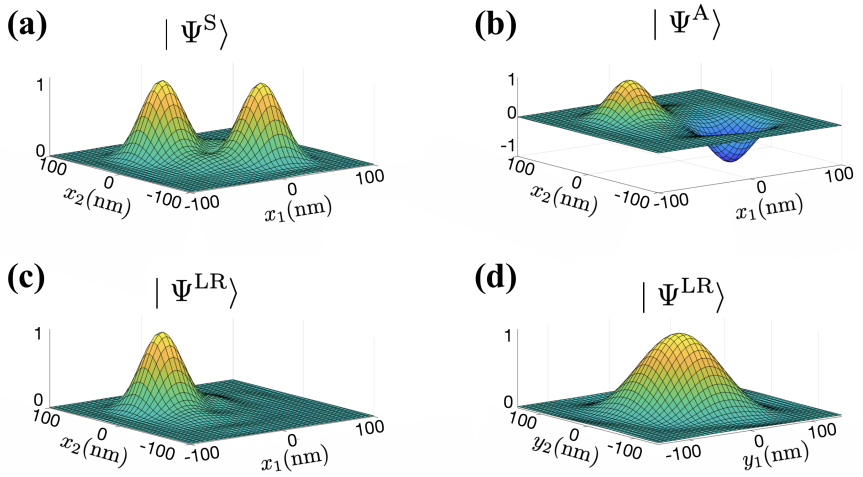

Fig. 6.2 Two-particle initial spatial wave functions. **(a)** Ground state $|\Psi^{\mathrm{S}}\rangle$ ($y_1 = 0$ and $y_2 = 0$). **(b)** First excited state $|\Psi^{\mathrm{A}}\rangle$ ($y_1 = 0$ and $y_2 = 0$). **(c)** Combination of the ground state and first excited state $|\Psi^{\mathrm{LR}}\rangle$. The first particle is localized in the left channel and the second particle is localized in the right channel ($y_1 = 0$ and $y_2 = 0$). **(d)** Gaussian spread of both particles in the y-dimension ($x_1 = 0$ and $x_2 = 0$). All four panels show the wave function divided by its extremum, with the z-axis in arbitrary units.

The double-dot potential of the gate region is chosen such that an equal linear combination of these states has both particles well localised in different channels. This results in the eigenstates of initial high tunnel barrier and those of the gate region having a high overlap. The disturbance introduced by adiabatically changing the tunnel barrier in the SAW reference frame is reduced by minimizing the amplitude and abruptness of the spatially changing potential.

We can write down combined space and spin states as $|s_1 s_2\rangle_{\mathrm{LR}}$, with particle 1 being in the left channel with spin s_1 and particle 2 being in the right channel with spin s_2. They are linear combinations of the triplet and singlet states:

$$\begin{aligned} |\downarrow\uparrow\rangle_{\mathrm{LR}} &= \frac{1}{\sqrt{2}}\left(|\mathrm{T}\rangle + |\mathrm{S}\rangle\right) \\ &= \frac{1}{\sqrt{2}}\left(|\Psi^{\mathrm{RL}}(r_1,r_2)\rangle\,|\uparrow\rangle|\downarrow\rangle - |\Psi^{\mathrm{LR}}(r_1,r_2)\rangle\,|\downarrow\rangle|\uparrow\rangle\right), \end{aligned} \tag{6.12}$$

$$\begin{aligned} |\uparrow\downarrow\rangle_{\mathrm{LR}} &= \frac{1}{\sqrt{2}}\left(|\mathrm{T}\rangle - |\mathrm{S}\rangle\right) \\ &= \frac{1}{\sqrt{2}}\left(|\Psi^{\mathrm{LR}}(r_1,r_2)\rangle\,|\uparrow\rangle|\downarrow\rangle - |\Psi^{\mathrm{RL}}(r_1,r_2)\rangle\,|\downarrow\rangle|\uparrow\rangle\right), \end{aligned} \tag{6.13}$$

where $|\Psi^{\mathrm{LR}}(r_1,r_2)\rangle$ denotes a spatial state with particle 1 in the left channel (negative x) and particle 2 in the right channel (positive x). These take the form

$$|\Psi^{\mathrm{RL}}(r_1,r_2)\rangle = \frac{1}{\sqrt{2}}\left(|\Psi^{\mathrm{S}}(r_1,r_2)\rangle + |\Psi^{\mathrm{A}}(r_1,r_2)\rangle\right), \tag{6.14}$$

$$|\Psi^{\mathrm{LR}}(r_1,r_2)\rangle = \frac{1}{\sqrt{2}}\left(|\Psi^{\mathrm{S}}(r_1,r_2)\rangle - |\Psi^{\mathrm{A}}(r_1,r_2)\rangle\right). \tag{6.15}$$

A system placed in such a linear superposition oscillates coherently with the period, $2\pi\hbar/(E_{\mathrm{T}} - E_{\mathrm{S}})$, determined by the energy difference between the ground state and first excited state. This period was derived in Eq. 6.9. A full SWAP operation takes half of this period whilst the root-of-SWAP operation takes a quarter of it, i.e. half the duration of a SWAP. In the limit where the on-site Coulomb energy is much greater than the hopping energy, the doubly-occupied states have vanishingly small probability amplitudes and can be ignored [12]. The state during the time evolution is

$$|\psi(t)\rangle = \frac{1}{\sqrt{2}}\left\{|\mathrm{T}\rangle + \exp\left(\frac{-it}{\hbar}\Delta E\right)|\mathrm{S}\rangle\right\}, \tag{6.16}$$

where $\Delta E = E_{\mathrm{T}} - E_{\mathrm{S}}$. This description of the power-of-SWAP operation allows the probabilities of observing spin-up (spin-down) particles in the left (right) channels after the operation to be calculated. The probability of measuring a swapped state, assuming an initial state

$|\uparrow\downarrow\rangle_{\mathrm{LR}}$ and a fixed time of interaction τ, is given by

$$\begin{aligned} P_{\mathrm{SWAP}}(J) &= |\langle \psi(t=\tau)|\downarrow\uparrow\rangle_{\mathrm{LR}}|^2 \\ &= \sin^2\left(\frac{1}{2}J\cdot\tau\right), \end{aligned} \tag{6.17}$$

where $J = \Delta E/(2\pi\hbar)$. This probability, given an input state, depends only on the energy difference between the triplet and singlet states, which in turn is a function of the device potential. For simplicity and computational resource optimisation, a spinless model is considered from hereon. Since the potential does not have any explicit spin dependence, because of a weak Lorentz term, single-qubit spin rotations do not occur.

6.2 Entanglement Generation via Electron Collisions

In a previously suggested root-of-SWAP scheme [121], two electrons travel in individual channels separated by a high potential barrier, such that there is no wave-function overlap. The potential barrier *abruptly* (or diabatically) changes in the SAW reference frame such that the two channels are joined to create a global potential minimum between them. Without the presence of the barrier, both electrons fall towards one another in a harmonic oscillator potential and interact via the Coulomb force. Once the operation is completed, the central barrier is reintroduced, causing the reappearance of separate decoupled channels. As the quantum states of particles in layered semiconductor technologies are confined in the dimension perpendicular to the quantum wells, which has a constant potential throughout the device, the third dimension does not significantly affect the operation. However, the previous reduction to one dimensional simulations presented in Owen *et al.* [121] is an oversimplification, as the possible spatial dynamics in the second dimension strongly affect the electron-electron interactions.

In our paper (Phys. Rev. A 101, 022329), [104] we simulate this *single-shot* (i.e. in a single collision) entanglement generation. We find that under current experimentally realistic parameters, it is impossible to generate a root-of-SWAP, or any significant entanglement over the x-dimension.

Figure 6.3 shows snapshots of the two-electron wave function undergoing a single collision in two dimensions. The wave function remains fully separable along the x dimension. However, in the y dimension, it transitions from a Gaussian-like low-energy state to a more spread-out entangled state. This is conflicting with the desired outcome of generating a maximally entangled state in the x dimension. The operation is effectively a SWAP instead of a root-of-SWAP, with the additional downside of exciting higher-energy states in the y

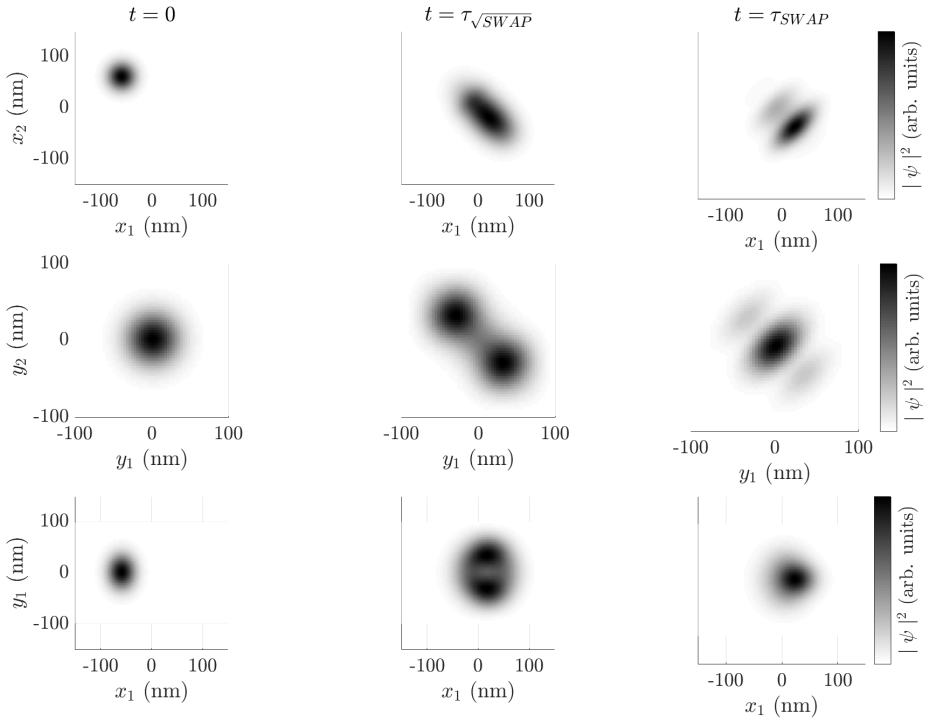

Fig. 6.3 Entanglement generation via the collision of two electrons. Top and middle row: trace over the x-dimension and y-dimension respectively for the initial state (left), root-of-SWAP state (centre), and SWAP state (right) of the wave function. Bottom row: trace over the second particle for the initial state (left), root-of-SWAP state (centre), and SWAP state (right) of the wave function. Coordinates are chosen to be in the SAW frame of reference with $y = 0$ corresponding to a SAW minimum and $x = 0$ the middle of the harmonic channel.

dimension. These unwanted spatial excitations of the wave function lead to lowering the spatial fidelity of the operation and thus it is not possible to concatenate multiple operations for useful quantum information processing. Excitations in the y dimension also prevent the restoration of the wave function to its original state by applying the SWAP twice, a fundamental property of this operation. The energy of the available states in y do not, in general, have the same splitting as in x. Even if the wave function projected along the x dimension is restored, perturbations in y affect future entangling operations.

Increasing the y confinement does not prevent this behaviour until the SAW amplitude is increased by a factor on the order of 10^3, where the problem effectively reduces to one dimension. However, such a confinement would require SAW amplitudes on the order of 10^4 meV, which is experimentally unrealistic.[150] Varying the x confinement over a wide range also does not solve the issue. Therefore, the conclusion is that the collision method is unable to produce the root-of-SWAP operation in a realistic two-dimensional scenario.

6.3 Entanglement Generation via Coulomb Tunnelling

Although a single-shot root-of-SWAP scheme for two electrons in moving quantum dots is not viable, two-qubit operations and entanglement generation is not impossible. Building on a proposal from Barnes *et al.* [12], it is possible to use an exchange-interaction method for the generation of entanglement between two electrons in a SAW system. In this scheme, the two particles undergo a continuous power-of-SWAP, which can be tuned to halt at any desired fraction of the complete SWAP. As described in Sec. 6.1, the two electrons occupy adjacent channels separated by a high potential barrier, suppressing any wave function overlap. As the electrons travel across the device, they enter a region in which the potential barrier between them is lower. They are allowed to tunnel through to the other channel at a rate that is determined in part by the barrier height and in part by the Coulomb force, thus allowing for the control of the power-of-SWAP gate by tuning the appropriate Schottky gates. Figure 6.4 shows snapshots of the wave function during an entangling operation with realistic experimental parameters. When the potential barrier is low, the two-particle state undergoes coherent oscillations between the initial state and the fully swapped state. The duration of the two-particle operation is determined by the length of the tunnel-coupled region. Since the speed of a SAW is constant in a given material, the operation is identical for all incoming electron pairs.

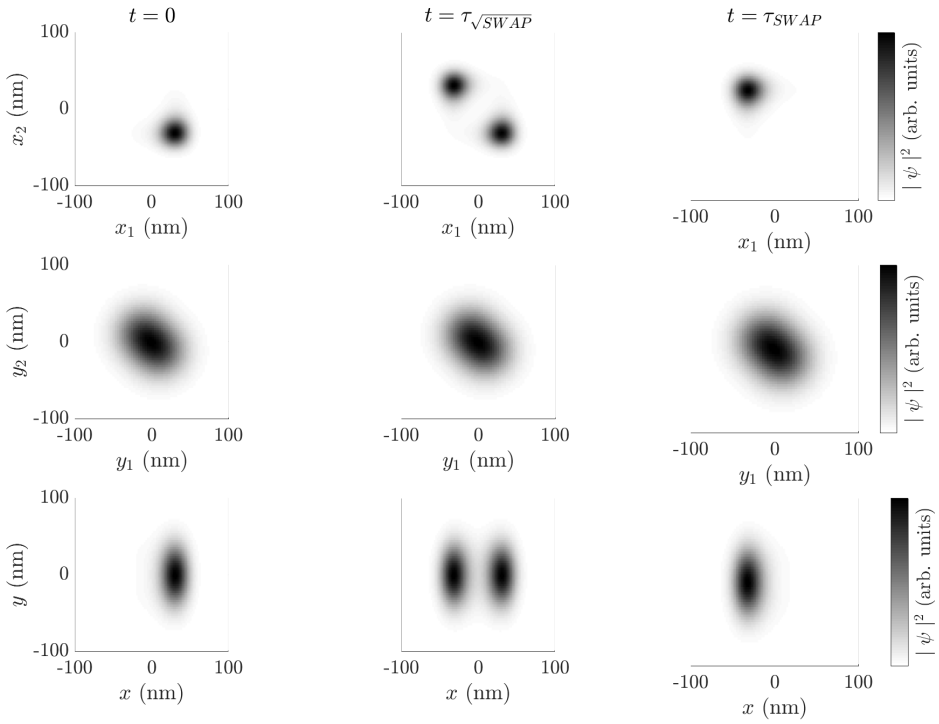

Fig. 6.4 Entanglement generation using the Coulomb tunneling method. Top and middle row: trace over the x-dimension and y-dimension respectively for the initial state (left), root-of-SWAP state (center), and SWAP state (right) of the wave function. Bottom row: trace over the second particle for the initial state (left), root-of-SWAP state (centre), and SWAP state (right) of the wave function. Coordinates are chosen to be in the SAW frame of reference with $y = 0$ corresponding to a SAW minimum and $x = 0$ the peak of the tunnel barrier.

Starting with Eq. 6.17, and assuming that J is exponentially dependent on the tunnel barrier height A_{TB}, and time of interaction τ is fixed, the probability of the final state being swapped with respect to the initial state has the following dependence on the tunnel barrier:

$$P_{\mathrm{SWAP}}\left(A_{\mathrm{TB}},\tau\right)=\sin^2\left(\frac{1}{2}J_0\cdot e^{-b\cdot A_{\mathrm{TB}}}\cdot\tau\right), \tag{6.18}$$

where J_0 and b are numerically determined parameters. Figure 6.5 shows a fit of the time-dependent numerical simulation data (See Appendix B for the exact values of the parameters) with the analytical prediction from Eq. 6.18. It is important to note that although Eq. 6.18 can describe the behaviour of a power-of-SWAP under ideal conditions, a numerical approach is required to account for more realistic scenarios. These can include the presence of impurities in the quantum channels as well as a finite transition length between the low and high tunnel barrier heights. The inset in Fig. 6.5 shows the probability amplitude of the computational basis states as well as double occupancy states during the root-of-SWAP operation. Interactions between the electrons are initially prohibited by the high potential barrier separating them. As they are carried through the tunnel-coupled region, the electrons become entangled. Upon leaving the region of low potential barrier, the particles can no longer interact and the probability amplitudes become constant.

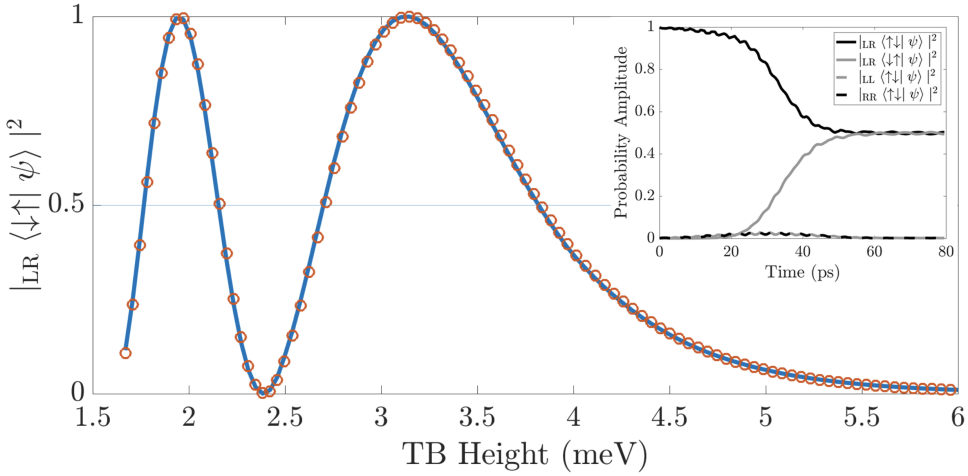

Fig. 6.5 Probability of SWAP as a function of tunnel barrier height for fixed interaction duration. Time evolution simulation results (circles) are fit using Equation 6.17 (solid line). The parameters $J_0 = 2.888\mathrm{ps}^{-1}$ and $b = 0.933\mathrm{meV}^{-1}$ were found numerically. The inset figure illustrates the occupation of the computational basis states as well as the double occupancy states. In this example, the input state $|\uparrow\downarrow\rangle_{\mathrm{LR}}$ undergoes a root-of-SWAP operation with finite tunnel barrier potential ramps.

A noteworthy observation is that although the interaction between the two particles depends exponentially on the height of the tunnel barrier separating them, the probability of a SWAP operation oscillates. Because of this, the gradient of the curve seen in Fig. 6.5 is smaller and the operation is more controllable experimentally. The SWAP probability around $P_{\mathrm{SWAP}} = 0.5$ varies with the tunnel barrier height at a rate of 8.07×10^{-4} $\mu\mathrm{eV}^{-1}$. This allows for an experimentally viable tunability of the quantum gate via the control of the tunnel barrier height. Assuming a device temperature of 300 mK, tunnel barrier variations due to thermal fluctuations will decrease the root-of-SWAP fidelity by $< 0.1\%$. This error could be reduced by increasing the height of the tunnel barrier, at the cost of extending the operation time.

6.3.1 Comparison to Analytical 2-site Models

To solve the dynamics of the power-of-SWAP operation in a heterostructure SAW-based device, including the 2D spatial extent of the wave function and a time-dependent potential, numerical simulations must be used. However, to avoid lengthy and complicated computations, ΔE can be estimated using simplified two-site models, thus getting an approximation for the power-of-SWAP extent via Eq. 6.17.

Assuming a tight-binding-like model, where electrons can tunnel between the quantum dots, we can estimate the full 2D time evolution by applying the Hund-Mulliken model for molecular orbitals.[33] This model builds a two-particle basis from right- and left-localised single-particle states $|\phi_{\pm}\rangle$. The states are orthonormalised to $|\Phi_{\pm}\rangle = (|\phi_{\pm}\rangle - g\,|\phi_{\mp}\rangle)/(\sqrt{1-2Sg+g^2})$, where $S = \langle \phi_{\pm} \mid \phi_{\mp} \rangle$ is the wave function overlap and $g = (1 - \sqrt{1-S^2})/S$. The singly- and doubly-occupied two-particle basis is constructed with direct products:

$$\begin{aligned} |\Psi^{s}_{\mp}\rangle &= \frac{1}{\sqrt{2}}\left(|\Phi_{+}\rangle|\Phi_{-}\rangle \mp |\Phi_{-}\rangle|\Phi_{+}\rangle\right), \\ |\Psi^{d}_{\mp}\rangle &= |\Phi_{\mp}\rangle|\Phi_{\mp}\rangle\,. \end{aligned} \tag{6.19}$$

The Hamiltonian in this basis has the form:

$$\hat{H} = \begin{pmatrix} V_{-} & 0 & -\sqrt{2}t_{\mathrm{h}} & 0 \\ 0 & V_{+} & -\sqrt{2}t_{\mathrm{h}} & 0 \\ 0 & -\sqrt{2}t_{\mathrm{h}} & U & X \\ 0 & -\sqrt{2}t_{\mathrm{h}} & X & U \end{pmatrix}, \tag{6.20}$$

where each entry is defined as:

$$U = \frac{e^2}{4\pi\varepsilon} \langle \Psi^d_{\pm} | \frac{1}{r} | \Psi^d_{\pm} \rangle , \tag{6.21}$$

$$X = \frac{e^2}{4\pi\varepsilon} \langle \Psi^d_{\pm} | \frac{1}{r} | \Psi^d_{\mp} \rangle , \tag{6.22}$$

$$V_+ = \frac{e^2}{4\pi\varepsilon} \langle \Psi^s_{+} | \frac{1}{r} | \Psi^s_{+} \rangle , \tag{6.23}$$

$$V_- = \frac{e^2}{4\pi\varepsilon} \langle \Psi^s_{-} | \frac{1}{r} | \Psi^s_{-} \rangle , \tag{6.24}$$

and t_h is the hopping term

$$t_\mathrm{h} = \langle \Phi_{\pm} | \frac{\hat{p}^2}{2m} | \Phi_{\mp} \rangle - \frac{e^2}{4\sqrt{2}\pi\varepsilon} \langle \Psi^s_{+} | \frac{1}{r} | \Psi^d_{\pm} \rangle . \tag{6.25}$$

Here, ε is the relative permittivity of GaAs and e is the electric charge of an electron.

Solving the eigenvalue problem for the Hund-Mulliken Hamiltonian in Eq. 6.20, gives the eigenenergies associated with the singlet and triplet states and define the SWAP frequency in terms of U and t_h:

$$J = \frac{1}{2\pi\hbar} \left[V_- - V_+ + \frac{1}{2} \left(\sqrt{U_\mathrm{h}^2 + 16 t_\mathrm{h}^2} - U_\mathrm{h} \right) \right] = \frac{E_\mathrm{T} - E_\mathrm{S}}{2\pi\hbar}, \tag{6.26}$$

where $U_\mathrm{h} = U - V_+ + X$.

Alternatively, the evolution of the two-particle state can also be modelled with the Hubbard approach for short range Coulomb interaction.[12] Without magnetic fields, the simplified 2-site Hamiltonian in the second quantisation basis from Eq. 6.4 is described in Sec. 6.1

Solving the eigenvalue problems for this Hamiltonian, gives the eigenenergies associated with the singlet and triplet states and defines the SWAP frequency in terms of U and t_LR:

$$J = \frac{1}{4\pi\hbar} \left(-U + \sqrt{U^2 + 16 t_\mathrm{LR}^2} \right) = \frac{E_\mathrm{T} - E_\mathrm{S}}{2\pi\hbar}. \tag{6.27}$$

For realistic Hamiltonians, it is impossible to obtain U analytically. Instead, this parameter must be calculated numerically. To avoid unphysical results introduced by the $1/r$ factor in Eq. 6.7, a softened Coulomb potential is used [121] both for the models and the numerical simulations. This softening is implemented by assuming that the wave function has a Gaussian spread in the third dimension, with a standard deviation of Δ_z. Since the semiconductor heterostructure is of constant width in the z dimension and is made up of the

same material, it is safe to assume that the wave function spread Δ_z is constant everywhere in the device. The effective Coulomb potential becomes

$$V_C(r) = \frac{e^2}{4\sqrt{2}\pi\varepsilon\Delta_z U(-\frac{1}{2}, 0, \frac{r^2}{2\Delta_z^2})}, \tag{6.28}$$

where U is the confluent hypergeometric function of the second kind.[161, 2] The integral representation of this function, also referred to as the Kummer U function, is

$$U(a,b,z) = \frac{1}{\Gamma(a)} \int_0^\infty e^{-zt} t^{a-1} (1+t)^{b-a-1} dt. \tag{6.29}$$

Both the Hubbard model and the Hund-Mulliken method described above are compared to the full two-dimensional simulation results for a range of Δ_z. The comparison of both analytical models with the numerical simulations is shown in Fig. 6.6. Comparing the frequency of the SWAP operation between the time-dependent numerical solver and the energy difference found by solving the time-independent eigenvalue problem numerically shows a close match. This is to be expected if the underlying potential remains constant. Since the initial wave function is a superposition of the two first eigenstates, the period of oscillation can be found analytically. This match serves as further validation that the time-dependent simulations are accurate and that the calculations with a time-varying potential such as the ones that produced the inset in Fig. 6.5 can be trusted. It is important to note that, because of the time-varying potential, the inset in Fig. 6.5 can not be calculated using the simpler and faster eigenvalue solver.

Both models calculated from Eq. 6.9 and Eq. 6.26 show significant discrepancy for most values of Δ_z. Moreover, the Hund-Mulliken model predicts negative frequencies for $\Delta_z < 1$ nm. Although both models provide a reasonable qualitative prediction of the two-particle dynamics for Gaussian spread of $\Delta_z \sim 10 - 100$ nm, a more sophisticated numerical approach, such as the one provided with my simulations, is required to obtain precise quantitative dynamics.

6.4 Discussion

The two-qubit entangling operation is an essential building block of a quantum information processor and of the the DiVincenzo criteria listed in Sec. 1.1.2. In the early 2000s, two schemes were proposed to implement the power-of-SWAP operation to generate entanglement between electron-spin qubits [12, 33]. These proposals suggested using the exchange interaction between the single electrons to entangle them. Both papers provided

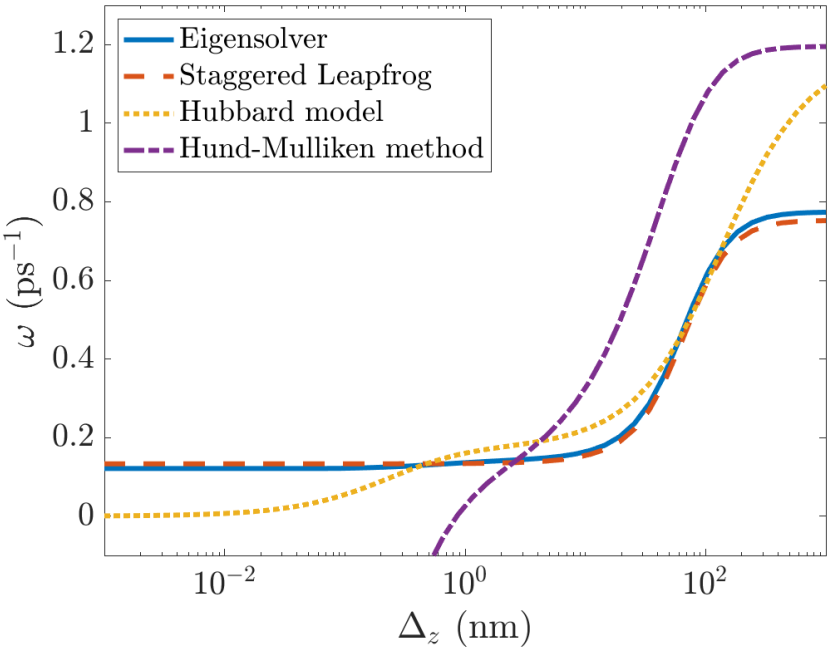

Fig. 6.6 Comparison to analytical models. Power-of-SWAP frequency as a function of effective wave function spread in the z-dimension. Coulomb softening accounts for the finite z-dimension and plays an important role in determining the rate of the exchange interaction.

analytical solutions that predicted the eigenvalues associated with the two-level systems and therefore the period of the gate operation. In this chapter, I showed numerically that surface-gate-controlled flying electron-spin qubits are able to generate entanglement through the power-of-SWAP operation in a reliable and stable fashion. Once again, the problem of wave function dispersion can be solved through the use of SAWs, which generate the potential confinement needed to preserve the wave function's profile. While the behaviour of an ideal system can be predicted exactly by solving the eigenvalue problem for the two-particle two-site Hamiltonian and assuming that the electrons are initialised to and remain in a combination of triplet and singlet states, the advantage of my numerical methods is to simulate realistic entangling operations. In any real setup, the interaction between the two particles is not controlled instantaneously. A two-site analytical model is insufficient to capture the complete dynamics of a changing potential.

In 2012, Owen *et al.* proposed a new method for entangling qubits [121] that built upon the work of Burkard *et al.* [33] and Barnes *et al.* [12]. This method had two electrons "fall" towards each other in a single harmonic potential and entangle in a single-shot operation. The appeal of this method is that the finite response time of the surface gates is no longer a problem since there are relatively long periods of time when the two particles are not

interacting. The central barrier gate can be turned on and off when the two electrons are far apart. This paper was also the first to provide numerical simulations for experimentally realistic potentials. However, the more sophisticated simulations presented in this chapter have shown that the original calculations in one dimension were an oversimplification of the problem. When solving for the two-particle dynamics in one dimension only, even with a softened Coulomb potential, the particles would interact strongly and entangle. By contrast, in two dimensions, the particles repel each other and simply swap channels without entangling. Furthermore, the displacement of the wave function in the new dimension prevent the wave function from returning to its initial state since the oscillations in this dimension do not have the same period as that of the SWAP operation. To recover the desired behaviour, the confinement in the new dimension must be increased to levels that far exceed what is possible experimentally. This leads to the conclusion that a continuous approach based on the exchange interaction is more stable.

The two-particle simulations presented in this chapter use experimentally realistic parameters and potential layouts. They show that root-of-SWAP devices are readily realisable using current semiconductor fabrication techniques. These results provide new evidence that an entangling root-of-SWAP gate based on the exchange interaction is experimentally viable in SAW-based semiconductor heterostructures. As with the rest of this thesis, these simulations were focused on the experimental parameters of GaAs-based devices. However, the same behaviour is expected in other SAW-based semiconductor devices. Moreover, these findings can be generalised to systems that do not include SAWs. Static quantum dots, confined in every dimension and separated by a tunnel barrier, interact in the same way. Such a tunnel barrier can be modulated using fast microwave pulses [31]. A static root-of-SWAP gate was recently realised with high fidelity using phosphorus donors in silicon [78], proving that such systems are achievable experimentally. Coherent spin-state SWAP operations between electron-spin qubits in a quadruple array of semiconductor quantum dots were also achieved [83].

7

CONCLUSION

In 2000, the original idea for a universal quantum computer using electrons trapped in surface acoustic waves was put forward [12]. Since then, many physical implementations of quantum computers have been introduced. Systems such as superconducting qubits [7, 38] and electron-spin qubits in phosphorous donors in silicon [157, 32] have gained significant traction in both the academic and industrial scene. Although it would seem that SAW-based systems are not currently ahead of the race to build a quantum computer, many of the concepts developed for the SAW platform are useful for designing specific components of quantum information systems. As quantum computers become larger, both in number of qubits and in size, coupling distant qubits becomes increasingly challenging. It is a requirement for universal quantum computation to be able to entangle any qubit with any other qubit. Therefore, a solution must be found to transport quantum information to different parts of a computer without the need to carry out many quantum operations, each acting as a source for errors.

In this thesis, I extensively covered the transport of single-electron qubits and the processing of their quantum information using surface acoustic waves. Electron qubits trapped in static quantum dots are displaced by the electric potential modulation generated by SAWs in piezoelectric materials. The constant confinement caused by the SAW solves the problems of wave function dispersion and scattering typically associated with massive particles.

I started by defining the optimal two level system for a charge qubit in a double quantum dot. Although this step may seem trivial, it is crucial to have a definition that is both realisable experimentally and scalable to future systems. Although a two-level system defined by the energy eigenstates of a particle in a double quantum dot is not directly accessible by experimentalists, I provide a straightforward method for initialising and rotating a single-electron qubit.

I am interested in transporting quantum information over distances on the scale of nanodevices and performing on-the-fly quantum operations. Much of the work in this thesis was inspired by quantum information processing in optical systems. Using surface acoustic waves, it is possible to replicate established devices and frameworks using massive fermionic particles. A key component of optical system is the beam splitter. Such a device can be designed using a shallow tunnel barrier between two quantum channels. The SAW potential guides single electrons through the tunnel-coupled region and defines the operation time. Surface gates creating the underlying electrostatic potential control the transmission and reflection coefficients of the beam splitter. Although there are still many challenges to overcome experimentally before a high-fidelity beam splitter can be made, simulations such as the ones presented in this thesis offer cost-effective solutions to experimental problems.

Once again inspired by optical quantum information processing, I put forward a scheme for performing a positive-operator-valued measure using massive particles. By chaining beam splitters together, a nested Mach-Zehnder interferometer is created. Local magnetic fields cause electron-spin-polarisation rotations, thus fulfilling all the requirements for realising Ahnert and Payne's POVM.

Semiconductor devices can also support multiple particles. In this case, interacting particles become entangled and each particle can be carried to a different part of a larger system. In this work, I present the root-of-SWAP operation as a maximally entangling operation. However, the idea of generating entanglement between flying electron qubits is essential to the realistic scaling of a large quantum computer.

7.1 Further Work

My code has produced a large amount of results, both in theoretical development and alongside experimental advances. When designing this software, I always kept expandability and modular additions in mind. As new research requires different devices to be modelled or more complex operations to be simulated, the simple addition of an electrostatic potential file or a tailored Hamiltonian is sufficient to adapt the master code. However, there is still

much work that can be made to expand the scope of this base code. In this section, I list a few project ideas that are realisable with current methods and technologies.

7.1.1 Solving the Lindblad Master Equation

In this work, I iteratively solved the time-dependent Schrödinger equation for complex systems. This method allowed me to get the accurate time evolution of a single or few-particle wave function. Although the wave function is a useful mathematical tool to study the behaviour of quantum particles, it does not intrinsically deal with decoherence. Since the effects due to the environment are not built into the Schrödinger equation, approximations must be made to simulate the coupling of system particles to external ones. An alternative approach is to solve a master equation for the density matrix ρ of the system rather than its wave function ψ. In this case, the most general solution to an open system is given by the Lindblad master equation [105, 27] :

$$\frac{\partial \rho}{\partial t} = -\frac{i}{\hbar}\left[\hat{H}, \rho\right] + \sum_{m,n} h_{mn}\left(\hat{A}_m \rho \hat{A}_n^\dagger - \frac{1}{2}\left\{\hat{A}_n^\dagger \hat{A}_m, \rho\right\}\right), \tag{7.1}$$

where $\hat{A}$ is an arbitrary Hermitian operator (also called Lindblad operator), h is the coefficient matrix of the system and the density matrix is defined as

$$\rho = \sum_j p_j \left|\psi_j\right\rangle \left\langle\psi_j\right|. \tag{7.2}$$

Although solving Eq. 7.1 instead of the time-dependent Schrödinger equation (Eq. 2.1) provides information about the decoherence of the quantum system coupling to the environment, it significantly increases the computational complexity of a given problem. A system described by a wave function of size N requires a density matrix of size N^2 to be iterated. This increased complexity is on the same order as adding a particle to the system or solving a problem in an extra dimension. It is therefore possible to solve the Lindblad equation using state-of-the-art GPUs for problems of slightly reduced complexity.

7.1.2 Quantum Media Conversion

The Bloch sphere described in Section 1.1.3 is typically used to represent electron spin states or electron charge qubit states. There exists a similar representation for photon polarisation qubits called the Poincaré sphere. A quantum state transfer from electron spins to photon polarisation and vice versa bridges the two spheres and provides a possible resolution to the

6th and 7th DiVincenzo criteria. In 2008, Kosaka *et al.* demonstrated that it was possible to coherently transfer an arbitrary superposition state from light polarization to electron spins [98, 99]. It is therefore possible to establish a one-to-one mapping between the Bloch and Poincaré spheres as illustrated in Figure 7.1.

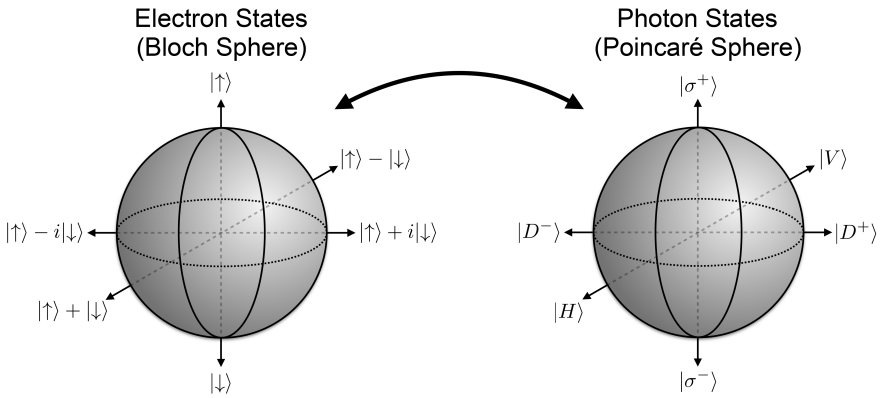

Fig. 7.1 Representations of the Bloch and Poincaré spheres. A one-to-one mapping can be found for every state on the spheres.

The quantum state of a single photon emitted from an electron-hole recombination is determined by selection rules. These rules arise from the conservation of angular momentum between electron spin and photon polarisation helicity [93]. A schematic of the quantum state of light emitted from an electron-hole recombination in a four-band model can be seen in Fig. 7.2. It has been shown that careful engineering of the material band structure can lead to a depletion of light holes [98] and thus generate a one-to-one mapping of electron-spin to photon-polarization pure states.

Using a modified version of the staggered-leapfrog algorithm could lead to a more complete theoretical description of the recombination process and light emission. Although the spin to polarisation mapping has a simple set of rules, the effects of momentum in the electron on the emitted photon have not been studied thoroughly. A study of quantum media conversion between electrons and photons is not only useful for quantum communication applications, but also provides a new way of linking different parts of a quantum computer together. The SAW-driven quantum bus described in this thesis offers a robust way of transporting quantum information, but it is limited to relatively short distances. The speed of photons would allow distant components to be entangled or even allow the transport of quantum information between two separate computers.

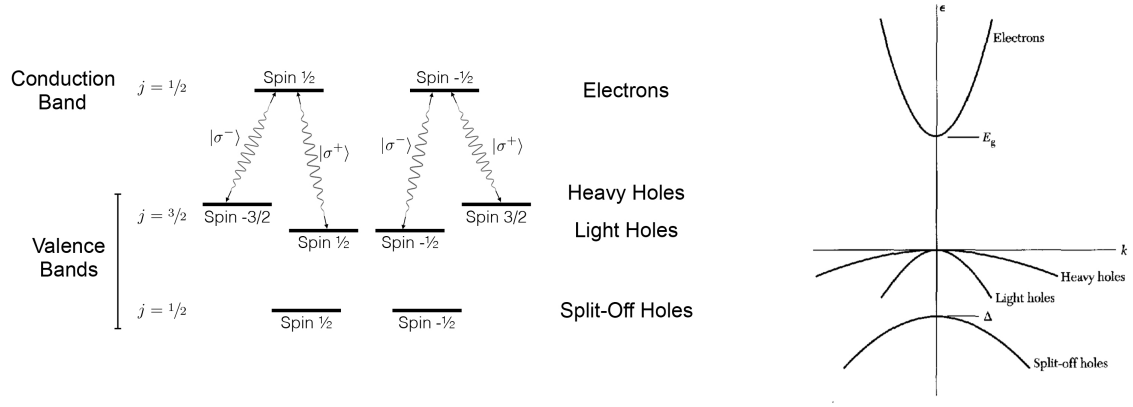

Fig. 7.2 Schematic of the electronic band structure in a semiconductor material (right) and the selection rules for electron-hole recombination with single photon emission in a four-band model (left).

7.1.3 FPGA Programming

A field-programmable gate array (FPGA) is a collection of integrated circuits on a chip. These circuits can be configured to perform specific tasks very quickly and with minimal computational overhead. Similar to an application-specific integrated circuit (ASIC), an FPGA uses a hardware description language to physically configure the array of logic gates on the chip. However, as opposed to ASICs, FPGAs are reconfigurable after their manufacturing, which makes them more versatile and often less expensive for small-scale production volumes.

Owing to their flexibility, high-bandwidth, and computational speed, FPGAs are widely used in avionics guidance systems for aerospace and defence technologies, real-time signal processing, and computer vision. Other common applications include high-performance computing applied to bioinformatics, data mining systems, Monte Carlo simulations, and stochastic simulations of chemistry. Recently, companies such as Intel and Microsoft have started using FPGAs to accelerate computationally intensive systems such as data centres and AI research. Most of these applications rely on the FPGA's ability to process very large amounts of data as fast as possible.

In this thesis, I used GPUs as a hardware platform for accelerating numerical solutions to the time-dependent Schrödinger equation. As a future project, FPGA hardware could be introduced to physics simulations as a novel tool to solve problems that are currently out of reach for traditional CPU or GPU calculations. The simulation of quantum systems is a task that would greatly benefit from FPGA acceleration. The integrated components on FPGAs are particularly useful for this kind of simulation. A large amount of digital signal

processors (DSPs) on-board allows for efficient Fourier Transforms (for momentum-based solutions) and moving average filters (for spatial solutions) without the large overhead that accompanies these algorithms in CPUs and GPUs. I have observed that these are the limiting steps in my quantum simulations and thus have preliminary evidence that FPGA systems would provide a significant acceleration over current GPU implementations. Eliminating this GPU bottleneck opens up the possibility of simulating more complicated systems in shorter times.

With the arrival of noisy intermediate-scale quantum computers, the need for validation of these systems is now evident. Currently, it is impossible to test if systems of a few particles are controlled accurately. Many quantum-computer simulators are currently being developed [128], but these all assume well defined qubit states, which is not necessarily the case for many experimental systems. With a new FPGA-based technology, it would be possible to investigate quantum systems at the hardware level and possibly even simulate some biochemical molecules.

Furthermore, a more complete numerical model for quantum mechanical simulations would allow for an intuitive investigation of the foundations of quantum mechanics. There are still some fascinating and paradoxical phenomena that are being discovered in the field of quantum mechanics, but experimentally, it is difficult to create an apparatus capable of showing these strange results. Experimentalists are often uncertain if their equipment will yield the precision required to observe the quantum nature of particles. By extending my current quantum solver to include decoherence and making adequate hardware available, it will be possible to test the viability of experimental setups.

REFERENCES

[1] Scott Aaronson. The limits of quantum computers. *Scientific American*, 298(3):50–57, 2008.

[2] Milton Abramowitz, Irene A Stegun, and Robert H Romer. Handbook of mathematical functions with formulas, graphs, and mathematical tables, 1988.

[3] Yakir Aharonov, David Z Albert, and Lev Vaidman. How the result of a measurement of a component of the spin of a spin-1/2 particle can turn out to be 100. *Physical review letters*, 60(14):1351, 1988.

[4] SE Ahnert and MC Payne. General implementation of all possible positive-operator-value measurements of single-photon polarization states. *Physical Review A*, 71(1): 012330, 2005.

[5] SE Ahnert and MC Payne. All possible bipartite positive-operator-value measurements of two-photon polarization states. *Physical Review A*, 73(2):022333, 2006.

[6] Sanjeev Arora and Boaz Barak. *Computational complexity: a modern approach*. Cambridge University Press, 2009.

[7] Frank Arute, Kunal Arya, Ryan Babbush, Dave Bacon, Joseph C Bardin, Rami Barends, Rupak Biswas, Sergio Boixo, Fernando GSL Brandao, David A Buell, et al. Quantum supremacy using a programmable superconducting processor. *Nature*, 574 (7779):505–510, 2019.

[8] David RM Arvidsson-Shukur, Hugo V Lepage, Edmund T Owen, Thierry Ferrus, and Crispin HW Barnes. Protocol for fermionic positive-operator-valued measures. *Physical Review A*, 96(5):052305, 2017.

[9] MR Astley, M Kataoka, CJB Ford, CHW Barnes, D Anderson, GAC Jones, Ian Farrer, DA Ritchie, and Michael Pepper. Non-invasive charge detection in surface-acoustic-wave-defined dynamic quantum dots. *Applied Physics Letters*, 109(18):183501, 2016.

[10] David D Awschalom, Lee C Bassett, Andrew S Dzurak, Evelyn L Hu, and Jason R Petta. Quantum spintronics: engineering and manipulating atom-like spins in semiconductors. *Science*, 339(6124):1174–1179, 2013.

[11] Adriano Barenco, Charles H Bennett, Richard Cleve, David P DiVincenzo, Norman Margolus, Peter Shor, Tycho Sleator, John A Smolin, and Harald Weinfurter. Elementary gates for quantum computation. *Physical review A*, 52(5):3457, 1995.

[12] CHW Barnes, JM Shilton, and AM Robinson. Quantum computation using electrons trapped by surface acoustic waves. *Physical Review B*, 62(12):8410, 2000.

[13] Stephen M Barnett, David T Pegg, and John Jeffers. Bayes' theorem and quantum retrodiction. *Journal of Modern Optics*, 47(11):1779–1789, 2000.

[14] Christopher Bäuerle, D Christian Glattli, Tristan Meunier, Fabien Portier, Patrice Roche, Preden Roulleau, Shintaro Takada, and Xavier Waintal. Coherent control of single electrons: a review of current progress. *Reports on Progress in Physics*, 81(5): 056503, 2018.

[15] FE Becerra, Jingyun Fan, and A Migdall. Implementation of generalized quantum measurements for unambiguous discrimination of multiple non-orthogonal coherent states. *Nature communications*, 4(1):1–6, 2013.

[16] David Beckman, Amalavoyal N Chari, Srikrishna Devabhaktuni, and John Preskill. Efficient networks for quantum factoring. *Physical Review A*, 54(2):1034, 1996.

[17] Charles H Bennett, Herbert J Bernstein, Sandu Popescu, and Benjamin Schumacher. Concentrating partial entanglement by local operations. *Physical Review A*, 53(4): 2046, 1996.

[18] Charles H Bennett, Gilles Brassard, Sandu Popescu, Benjamin Schumacher, John A Smolin, and William K Wootters. Purification of noisy entanglement and faithful teleportation via noisy channels. *Physical review letters*, 76(5):722, 1996.

[19] Korte Bernhard and J Vygen. Combinatorial optimization: Theory and algorithms. *Springer, Third Edition, 2005.*, 2008.

[20] Benoit Bertrand, Sylvain Hermelin, Shintaro Takada, Michihisa Yamamoto, Seigo Tarucha, Arne Ludwig, Andreas D Wieck, Christopher Bäuerle, and Tristan Meunier. Fast spin information transfer between distant quantum dots using individual electrons. *Nature nanotechnology*, 11(8):672, 2016.

[21] Stefan Birner, Tobias Zibold, Till Andlauer, Tillmann Kubis, Matthias Sabathil, Alex Trellakis, and Peter Vogl. Nextnano: general purpose 3-d simulations. *IEEE Transactions on Electron Devices*, 54(9):2137–2142, 2007.

[22] Vincent Bouchiat, D Vion, Ph Joyez, D Esteve, and MH Devoret. Quantum coherence with a single cooper pair. *Physica Scripta*, 1998(T76):165, 1998.

[23] Ryan Bowler, John Gaebler, Yiheng Lin, Ting Rei Tan, David Hanneke, John D Jost, JP Home, Dietrich Leibfried, and David J Wineland. Coherent diabatic ion transport and separation in a multizone trap array. *Physical review letters*, 109(8):080502, 2012.

[24] Vladimir B Braginsky, Yuri I Vorontsov, and Kip S Thorne. Quantum nondemolition measurements. *Science*, 209(4456):547–557, 1980.

[25] Gerd Breitenbach. *Quantum state reconstruction of classical and nonclassical light and a cryogenic opto-mechanical sensor for high-precision interferometry*. PhD thesis, 1998.

[26] Gerd Breitenbach, S Schiller, and J Mlynek. Measurement of the quantum states of squeezed light. *Nature*, 387(6632):471–475, 1997.

[27] Heinz-Peter Breuer, Francesco Petruccione, et al. *The theory of open quantum systems*. Oxford University Press on Demand, 2002.

[28] Delia Brick, Vivienne Engemaier, Yuning Guo, Martin Grossmann, Guodong Li, Daniel Grimm, Oliver G Schmidt, Martin Schubert, VE Gusev, Mike Hettich, et al. Interface adhesion and structural characterization of rolled-up gaas/in 0.2 ga 0.8 as multilayer tubes by coherent phonon spectroscopy. *Scientific reports*, 7(1):1–8, 2017.

[29] SI Brochure. The international system of units (si) [2019]. *BIPM, Paris*, 2019.

[30] David C Brock and Gordon E Moore. *Understanding Moore's law: four decades of innovation*. Chemical Heritage Foundation, 2006.

[31] R Brunner, Y-S Shin, T Obata, M Pioro-Ladrière, T Kubo, K Yoshida, T Taniyama, Y Tokura, and S Tarucha. Two-qubit gate of combined single-spin rotation and interdot spin exchange in a double quantum dot. *Physical review letters*, 107(14):146801, 2011.

[32] H Büch, S Mahapatra, Rajib Rahman, Andrea Morello, and MY Simmons. Spin read-out and addressability of phosphorus-donor clusters in silicon. *Nature communications*, 4(1):1–6, 2013.

[33] Guido Burkard, Daniel Loss, and David P DiVincenzo. Coupled quantum dots as quantum gates. *Physical Review B*, 59(3):2070, 1999.

[34] John Charles Butcher. *Numerical methods for ordinary differential equations*. John Wiley & Sons, 2016.

[35] John Canny. Some algebraic and geometric computations in pspace. In *Proceedings of the twentieth annual ACM symposium on Theory of computing*, pages 460–467, 1988.

[36] Manuel Cardona and Y Yu Peter. *Fundamentals of semiconductors*. Springer, 2005.

[37] James A Carlson, Arthur Jaffe, and Andrew Wiles. *The millennium prize problems*. American Mathematical Society Providence, RI, 2006.

[38] Davide Castelvecchi. Ibm's quantum cloud computer goes commercial. *Nature News*, 543(7644):159, 2017.

[39] Alexander H-D Cheng and Daisy T Cheng. Heritage and early history of the boundary element method. *Engineering Analysis with Boundary Elements*, 29(3):268–302, 2005.

[40] G Chrobok and M Hofmann. Electron spin polarization of secondary electrons ejected from magnetized europium oxide. *Physics Letters A*, 57(3):257–258, 1976.

[41] Kobi Cohen, Maxim Khodas, Boris Laikhtman, Paulo V Santos, and Ronen Rapaport. Vertically coupled dipolar exciton molecules. *Physical Review B*, 93(23):235310, 2016.

[42] B Jack Copeland. *Colossus: The secrets of Bletchley Park's code-breaking computers*. Oxford University Press, 2010.

[43] John Crank and Phyllis Nicolson. A practical method for numerical evaluation of solutions of partial differential equations of the heat-conduction type. In *Mathematical Proceedings of the Cambridge Philosophical Society*, volume 43, pages 50–67. Cambridge University Press, 1947.

[44] Jacques Curie and Pierre Curie. Développement par compression de l'électricité polaire dans les cristaux hémièdres à faces inclinées. *Bulletin de minéralogie*, 3(4): 90–93, 1880.

[45] John H Davies, Ivan A Larkin, and EV Sukhorukov. Modeling the patterned two-dimensional electron gas: Electrostatics. *Journal of Applied Physics*, 77(9):4504–4512, 1995.

[46] David Deutsch. Quantum theory, the church-turing principle and the universal quantum computer. In *Proceedings of the Royal Society of London A: Mathematical, Physical and Engineering Sciences*, volume 400, pages 97–117. The Royal Society, 1985.

[47] David Deutsch and Richard Jozsa. Rapid solution of problems by quantum computation. *Proceedings of the Royal Society of London. Series A: Mathematical and Physical Sciences*, 439(1907):553–558, 1992.

[48] David P DiVincenzo. Two-bit gates are universal for quantum computation. *Physical Review A*, 51(2):1015, 1995.

[49] David P DiVincenzo. The physical implementation of quantum computation. *Fortschritte der Physik: Progress of Physics*, 48(9-11):771–783, 2000.

[50] Andrew C Doherty and Kurt Jacobs. Feedback control of quantum systems using continuous state estimation. *Physical Review A*, 60(4):2700, 1999.

[51] Yuliya Dovzhenko, Jiri Stehlik, KD Petersson, Jason R Petta, Hong Lu, and AC Gossard. Nonadiabatic quantum control of a semiconductor charge qubit. *Physical Review B*, 84(16):161302, 2011.

[52] L-M Duan, JI Cirac, and P Zoller. Geometric manipulation of trapped ions for quantum computation. *Science*, 292(5522):1695–1697, 2001.

[53] Hermann Edlbauer. *Electron-quantum-optics experiments at the single particle level*. PhD thesis, Grenoble Alpes, 2019.

[54] Hermann Edlbauer, Shintaro Takada, Grégoire Roussely, Michihisa Yamamoto, Seigo Tarucha, Arne Ludwig, Andreas D Wieck, Tristan Meunier, and Christopher Bäuerle. Non-universal transmission phase behaviour of a large quantum dot. *Nature communications*, 8(1):1–8, 2017.

[55] JM Elzerman, R Hanson, LH Willems Van Beveren, B Witkamp, LMK Vandersypen, and Leo P Kouwenhoven. Single-shot read-out of an individual electron spin in a quantum dot. *nature*, 430(6998):431–435, 2004.

[56] Emerging Technology from the arXiv. How a quantum computer could break 2048-bit RSA encryption in 8 hours, 2020. URL https://www.technologyreview.com/s/613596/how-a-quantum-computer-could-break-2048-bit-rsa-encryption-in-8-hours/.

[57] Björn Engquist and Andrew Majda. Absorbing boundary conditions for numerical simulation of waves. *Proceedings of the National Academy of Sciences*, 74(5):1765–1766, 1977.

[58] Lara Faoro, Jens Siewert, and Rosario Fazio. Non-abelian holonomies, charge pumping, and quantum computation with josephson junctions. *Physical review letters*, 90 (2):028301, 2003.

[59] T Ferrus, A Rossi, M Tanner, G Podd, P Chapman, and DA Williams. Detection of charge motion in a non-metallic silicon isolated double quantum dot. *New Journal of Physics*, 13(10):103012, 2011.

[60] Richard P Feynman. Quantum mechanical computers. *Foundations of physics*, 16(6): 507–531, 1986.

[61] M Field, CG Smith, Michael Pepper, DA Ritchie, JEF Frost, GAC Jones, and DG Hasko. Measurements of coulomb blockade with a noninvasive voltage probe. *Physical Review Letters*, 70(9):1311, 1993.

[62] H Flentje, P-A Mortemousque, R Thalineau, A Ludwig, AD Wieck, C Bäuerle, and T Meunier. Coherent long-distance displacement of individual electron spins. *Nature communications*, 8(1):1–6, 2017.

[63] Sandra Foletti, Hendrik Bluhm, Diana Mahalu, Vladimir Umansky, and Amir Yacoby. Universal quantum control of two-electron spin quantum bits using dynamic nuclear polarization. *Nature Physics*, 5(12):903–908, 2009.

[64] Christopher J. B. Ford. personal communication.

[65] Toshimasa Fujisawa, Toshiaki Hayashi, Sung Woo Jung, Yoon-Ha Jeong, and Yoshiro Hirayama. Single-electron charge qubit in a double quantum dot. In *Quantum Computing in Solid State Systems*, pages 279–287. Springer, 2006.

[66] Takafumi Fujita, Timothy Alexander Baart, Christian Reichl, Werner Wegscheider, and Lieven Mark Koenraad Vandersypen. Coherent shuttle of electron-spin states. *npj Quantum Information*, 3(1):1–6, 2017.

[67] S Furuta, CH Wand Barnes, and CJL Doran. Single-qubit gates and measurements in the surface acoustic wave quantum computer. *Physical Review B*, 70(20):205320, 2004.

[68] S Gardelis, CG Smith, CHW Barnes, EH Linfield, and DA Ritchie. Spin-valve effects in a semiconductor field-effect transistor: A spintronic device. *Physical Review B*, 60 (11):7764, 1999.

[69] Michael R Garey and David S Johnson. *Computers and intractability*, volume 174. freeman San Francisco, 1979.

[70] Oded Goldreich. Computational complexity: a conceptual perspective. *ACM Sigact News*, 39(3):35–39, 2008.

[71] Herman H Goldstine. *The computer from Pascal to von Neumann*. Princeton University Press, 1980.

[72] J Gorman, DG Hasko, and DA Williams. Charge-qubit operation of an isolated double quantum dot. *Physical review letters*, 95(9):090502, 2005.

[73] Lov K Grover. A fast quantum mechanical algorithm for database search. In *Proceedings of the twenty-eighth annual ACM symposium on Theory of computing*, pages 212–219. ACM, 1996.

[74] Lov K Grover. From schrödinger's equation to the quantum search algorithm. *Pramana*, 56(2-3):333–348, 2001.

[75] R Hanson, JM Elzerman, LH Willems van Beveren, LMK Vandersypen, and LP Kouwenhoven. Electron spin qubits in quantum dots. In *IEDM Technical Digest. IEEE International Electron Devices Meeting, 2004.*, pages 533–536. IEEE, 2004.

[76] X Hao, JS Moodera, and R Meservey. Spin-filter effect of ferromagnetic europium sulfide tunnel barriers. *Physical review B*, 42(13):8235, 1990.

[77] Toshiki Hayashi, Toshimasa Fujisawa, Hai-Du Cheong, Yoon Hee Jeong, and Yoshiro Hirayama. Coherent manipulation of electronic states in a double quantum dot. *Physical review letters*, 91(22):226804, 2003.

[78] Yu He, SK Gorman, Daniel Keith, Ludwik Kranz, JG Keizer, and MY Simmons. A two-qubit gate between phosphorus donor electrons in silicon. *Nature*, 571(7765): 371–375, 2019.

[79] Sylvain Hermelin, Shintaro Takada, Michihisa Yamamoto, Seigo Tarucha, Andreas D Wieck, Laurent Saminadayar, Christopher Bäuerle, and Tristan Meunier. Electrons surfing on a sound wave as a platform for quantum optics with flying electrons. *Nature*, 477(7365):435–438, 2011.

[80] Hangtian Hou, Yousun Chung, Girish Rughoobur, Tzu-Kan Hsiao, Ateeq Nasir, Andrew J Flewitt, JP Griffiths, Ian Farrer, David A Ritchie, and CJB Ford. Experimental verification of electrostatic boundary conditions in gate-patterned quantum devices. *Journal of Physics D: Applied Physics*, 51(24):244004, 2018.

[81] D Hucul, M Yeo, WK Hensinger, J Rabchuk, S Olmschenk, and C Monroe. On the transport of atomic ions in linear and multidimensional ion trap arrays. *Quantum Information and Computation*, 8(6-7):501–578, 2008.

[82] G. Ifrah. *The universal history of computing*. New York: John Wiley, 2001.

[83] Yadav P Kandel, Haifeng Qiao, Saeed Fallahi, Geoffrey C Gardner, Michael J Manfra, and John M Nichol. Coherent spin-state transfer via heisenberg exchange. *Nature*, 573(7775):553–557, 2019.

[84] Bruce E Kane. A silicon-based nuclear spin quantum computer. *nature*, 393(6681): 133–137, 1998.

[85] Richard M Karp. Reducibility among combinatorial problems. In *Complexity of computer computations*, pages 85–103. Springer, 1972.

[86] M Kataoka, RJ Schneble, AL Thorn, CHW Barnes, CJB Ford, D Anderson, GAC Jones, I Farrer, DA Ritchie, and M Pepper. Single-electron population and depopulation of an isolated quantum dot using a surface-acoustic-wave pulse. *Physical review letters*, 98(4):046801, 2007.

[87] M Kataoka, MR Astley, AL Thorn, DKL Oi, CHW Barnes, CJB Ford, D Anderson, GAC Jones, I Farrer, DA Ritchie, et al. Coherent time evolution of a single-electron wave function. *Physical review letters*, 102(15):156801, 2009.

[88] Yuichiro K Kato, Roberto C Myers, Arthur C Gossard, and David D Awschalom. Observation of the spin hall effect in semiconductors. *science*, 306(5703):1910–1913, 2004.

[89] Erika Kawakami, Thibaut Jullien, Pasquale Scarlino, Daniel R Ward, Donald E Savage, Max G Lagally, Viatcheslav V Dobrovitski, Mark Friesen, Susan N Coppersmith, Mark A Eriksson, et al. Gate fidelity and coherence of an electron spin in an si/sige quantum dot with micromagnet. *Proceedings of the National Academy of Sciences*, 113(42):11738–11743, 2016.

[90] Khan Academy. Electron shells & orbitals | The periodic table, 2020. URL https://www.khanacademy.org/science/biology/chemistry--of-life/electron-shells-and-orbitals/a/the-periodic-table-electron-shells-and-orbitals-article.

[91] Laszlo B Kish. End of moore's law: thermal (noise) death of integration in micro and nano electronics. *Physics Letters A*, 305(3):144–149, 2002.

[92] Charles Kittel. *Introduction to solid state physics*, volume 8. Wiley New York, 1996.

[93] Charles Kittel and Donald F Holcomb. Introduction to solid state physics. *American Journal of Physics*, 35(6):547–548, 1967.

[94] Emanuel Knill, Raymond Laflamme, and Gerald J Milburn. A scheme for efficient quantum computation with linear optics. *nature*, 409(6816):46–52, 2001.

[95] Donald Ervin Knuth. *The art of computer programming*, volume 3. Pearson Education, 1997.

[96] Markus König, Steffen Wiedmann, Christoph Brüne, Andreas Roth, Hartmut Buhmann, Laurens W Molenkamp, Xiao-Liang Qi, and Shou-Cheng Zhang. Quantum spin hall insulator state in hgte quantum wells. *Science*, 318(5851):766–770, 2007.

[97] Frank HL Koppens, Christo Buizert, Klaas-Jan Tielrooij, Ivo T Vink, Katja C Nowack, Tristan Meunier, LP Kouwenhoven, and LMK Vandersypen. Driven coherent oscillations of a single electron spin in a quantum dot. *Nature*, 442(7104):766–771, 2006.

[98] Hideo Kosaka, Hideki Shigyou, Yasuyoshi Mitsumori, Yoshiaki Rikitake, Hiroshi Imamura, Takeshi Kutsuwa, Koichiro Arai, and Keiichi Edamatsu. Coherent transfer of light polarization to electron spins in a semiconductor. *Physical review letters*, 100 (9):096602, 2008.

[99] Hideo Kosaka, Takahiro Inagaki, Yoshiaki Rikitake, Hiroshi Imamura, Yasuyoshi Mitsumori, and Keiichi Edamatsu. Spin state tomography of optically injected electrons in a semiconductor. *Nature*, 457(7230):702–705, 2009.

[100] R Kosloff and D Kosloff. Absorbing boundaries for wave propagation problems. *Journal of Computational Physics*, 63(2):363–376, 1986.

[101] Karl Kraus, Arno Böhm, John D Dollard, and WH Wootters. States, effects, and operations: fundamental notions of quantum theory. lectures in mathematical physics at the university of texas at austin. *Lecture notes in physics*, 190, 1983.

[102] B Laikhtman and R Rapaport. Exciton correlations in coupled quantum wells and their luminescence blue shift. *Physical Review B*, 80(19):195313, 2009.

[103] Lev D Landau. Zur theorie der energieubertragung ii. *Z. Sowjetunion*, 2:46–51, 1932.

[104] Hugo V Lepage, Aleksander A Lasek, David RM Arvidsson-Shukur, and Crispin HW Barnes. Entanglement generation via power-of-swap operations between dynamic electron-spin qubits. *Physical Review A*, 101(2):022329, 2020.

[105] Goran Lindblad. On the generators of quantum dynamical semigroups. *Communications in Mathematical Physics*, 48(2):119–130, 1976.

[106] Daniel Loss and David P DiVincenzo. Quantum computation with quantum dots. *Physical Review A*, 57(1):120, 1998.

[107] Jon JV Maestri, Rubin H Landau, and Manuel J Páez. Two-particle schrödinger equation animations of wave packet–wave packet scattering. *American Journal of Physics*, 68(12):1113–1119, 2000.

[108] J Majer, JM Chow, JM Gambetta, Jens Koch, BR Johnson, JA Schreier, L Frunzio, DI Schuster, Andrew Addison Houck, Andreas Wallraff, et al. Coupling superconducting qubits via a cavity bus. *Nature*, 449(7161):443–447, 2007.

[109] Ettore Majorana. Atomi orientati in campo magnetico variabile. *Il Nuovo Cimento (1924-1942)*, 9(2):43–50, 1932.

[110] Yuriy Makhlin, Gerd Scöhn, and Alexander Shnirman. Josephson-junction qubits with controlled couplings. *nature*, 398(6725):305–307, 1999.

[111] RPG McNeil, M Kataoka, CJB Ford, CHW Barnes, D Anderson, GAC Jones, I Farrer, and DA Ritchie. On-demand single-electron transfer between distant quantum dots. *Nature*, 477(7365):439–442, 2011.

[112] GJ Milburn. Photons as qubits. *Physica Scripta*, 2009(T137):014003, 2009.

[113] Pierre-Andre Mortemousque, Emmanuel Chanrion, Baptiste Jadot, Hanno Flentje, Arne Ludwig, Andreas D Wieck, Matias Urdampilleta, Christopher Bauerle, and Tristan Meunier. Coherent control of individual electron spins in a two dimensional array of quantum dots. *arXiv preprint arXiv:1808.06180*, 2018.

[114] John JL Morton, Alexei M Tyryshkin, Arzhang Ardavan, Simon C Benjamin, Kyriakos Porfyrakis, Stephen Aplin Lyon, and G Andrew D Briggs. Bang–bang control of fullerene qubits using ultrafast phase gates. *Nature Physics*, 2(1):40–43, 2006.

[115] J Mosakowski, ET Owen, T Ferrus, DA Williams, MC Dean, and CHW Barnes. An optimal single-electron charge qubit for solid-state double quantum dots. *arXiv preprint arXiv:1603.05112*, 2016.

[116] M Murao, MB Plenio, Sandu Popescu, V Vedral, and PL Knight. Multiparticle entanglement purification protocols. *Physical Review A*, 57(6):R4075, 1998.

[117] Daniel Neuhasuer and Michael Baer. The time-dependent schrödinger equation: Application of absorbing boundary conditions. *The Journal of chemical physics*, 90 (8):4351–4355, 1989.

[118] Michael A Nielsen and Isaac L Chuang. Quantum computation and quantum information: 10th anniversary, 2011.

[119] Nvidia. Cuda C Programming Guide v8.0. *Design Guide*, (September):228, 2016. ISSN 15284972. doi: 10.1073/pnas.1010880108/-/DCSupplemental.www.pnas.org/cgi/. URL http://docs.nvidia.com/cuda/pdf/CUDA{_}C{_}Programming{_}Guide.pdf.

[120] The Editors of Encyclopaedia Britannica. *Seismic wave*. Encyclopædia Britannica, 2017.

[121] ET Owen, MC Dean, and CHW Barnes. Generation of entanglement between qubits in a one-dimensional harmonic oscillator. *Physical Review A*, 85(2):022319, 2012.

[122] ET Owen, MC Dean, and CHW Barnes. Coherent-state spin qubits in the presence of spin-orbit coupling. *Physical Review A*, 89(3):032305, 2014.

[123] Jian-Wei Pan, Christoph Simon, Časlav Brukner, and Anton Zeilinger. Entanglement purification for quantum communication. *Nature*, 410(6832):1067–1070, 2001.

[124] Jarryd J Pla, Kuan Y Tan, Juan P Dehollain, Wee H Lim, John JL Morton, David N Jamieson, Andrew S Dzurak, and Andrea Morello. A single-atom electron spin qubit in silicon. *Nature*, 489(7417):541–545, 2012.

[125] Enrico Prati. Valley blockade quantum switching in silicon nanostructures. *Journal of nanoscience and nanotechnology*, 11(10):8522–8526, 2011.

[126] John Preskill. Quantum computing and the entanglement frontier. *arXiv preprint arXiv:1203.5813*, 2012.

[127] V Ya Prinz, VA Seleznev, AK Gutakovsky, AV Chehovskiy, VV Preobrazhenskii, MA Putyato, and TA Gavrilova. Free-standing and overgrown ingaas/gaas nanotubes, nanohelices and their arrays. *Physica E: Low-dimensional Systems and Nanostructures*, 6(1-4):828–831, 2000.

[128] Quantiki. List of QC simulators, 2020. URL https://www.quantiki.org/wiki/list-qc-simulators. [Online; accessed 17-March-2020].

[129] Albert C Reynolds. Boundary conditions for the numerical solution of wave propagation problems. *Geophysics*, 43(6):1099–1110, 1978.

[130] Ronald L Rivest, Adi Shamir, and Leonard Adleman. A method for obtaining digital signatures and public-key cryptosystems. *Communications of the ACM*, 21(2):120–126, 1978.

[131] Nicolas Roch, Mollie E Schwartz, Felix Motzoi, Christopher Macklin, Rajamani Vijay, Andrew W Eddins, Alexander N Korotkov, K Birgitta Whaley, Mohan Sarovar, and Irfan Siddiqi. Observation of measurement-induced entanglement and quantum trajectories of remote superconducting qubits. *Physical review letters*, 112(17):170501, 2014.

[132] Tiffany Suzanne Santos. *Europium oxide as a perfect electron spin filter*. PhD thesis, Massachusetts Institute of Technology, 2007.

[133] SAWtrain Network. A few words about surface acoustic waves. http://www.sawtrain.eu/research/, 2019. Accessed: 2019-03-21.

[134] Oliver G Schmidt and Karl Eberl. Thin solid films roll up into nanotubes. *Nature*, 410 (6825):168–168, 2001.

[135] Max Schulz. The end of the road for silicon? *Nature*, 399(6738):729–730, 1999.

[136] Benjamin Schumacher. Quantum coding. *Physical Review A*, 51(4):2738, 1995.

[137] Ulrich Schumann and Roland A Sweet. A direct method for the solution of poisson's equation with neumann boundary conditions on a staggered grid of arbitrary size. *Journal of Computational Physics*, 20(2):171–182, 1976.

[138] Tamar Seideman and William H Miller. Quantum mechanical reaction probabilities via a discrete variable representation-absorbing boundary condition green's function. *The Journal of chemical physics*, 97(4):2499–2514, 1992.

[139] Semiconductor Physics Group. The use of saws to manipulate quantum bits (qubits), 2020. URL https://www.sp.phy.cam.ac.uk/research/surface-acoustic-waves-saws/sawqc. [Online; accessed 12-March-2020].

[140] Mark S Sherwin, Atac Imamoglu, and Thomas Montroy. Quantum computation with quantum dots and terahertz cavity quantum electrodynamics. *Physical Review A*, 60 (5):3508, 1999.

[141] Alexander Shnirman and Gerd Schoen. Quantum measurements performed with a single-electron transistor. *Physical Review B*, 57(24):15400, 1998.

[142] Peter W Shor. Polynomial-time algorithms for prime factorization and discrete logarithms on a quantum computer. *SIAM review*, 41(2):303–332, 1999.

[143] Kanchana Sivalertporn, Leonidas Mouchliadis, AL Ivanov, Roger Philp, and Egor A Muljarov. Direct and indirect excitons in semiconductor coupled quantum wells in an applied electric field. *Physical Review B*, 85(4):045207, 2012.

[144] Paolo Solinas, Paolo Zanardi, Nino Zanghì, and Fausto Rossi. Semiconductor-based geometrical quantum gates. *Physical Review B*, 67(12):121307, 2003.

[145] Matthias Steffen, Jay M Gambetta, and Jerry M Chow. Progress, status, and prospects of superconducting qubits for quantum computing. In *Solid-State Device Research Conference (ESSDERC), 2016 46th European*, pages 17–20. IEEE, 2016.

[146] James A Storer. On the complexity of chess. *Journal of computer and system sciences*, 27(1):77–100, 1983.

[147] Ernst Karl Gerlach Stückelberg. *Theorie der unelastischen Stösse zwischen Atomen*. Birkhäuser, 1933.

[148] K Tada, T Hashimoto, J Haruyama, H Yang, and M Chshiev. Spontaneous spin polarization and spin pumping effect on edges of graphene antidot lattices. *physica status solidi (b)*, 249(12):2491–2496, 2012.

[149] Shintaro Takada, Hermann Edlbauer, Hugo V Lepage, Junliang Wang, Pierre-André Mortemousque, Giorgos Georgiou, Crispin HW Barnes, Christopher JB Ford, Mingyun Yuan, Paulo V Santos, et al. Sound-driven single-electron transfer in a circuit of coupled quantum rails. *Nature communications*, 10(1):1–9, 2019.

[150] VI Talyanskii, JM Shilton, M Pepper, CG Smith, CJB Ford, EH Linfield, DA Ritchie, and GAC Jones. Single-electron transport in a one-dimensional channel by high-frequency surface acoustic waves. *Physical Review B*, 56(23):15180, 1997.

[151] James William Thomas. *Numerical partial differential equations: finite difference methods*, volume 22. Springer Science & Business Media, 2013.

[152] Scott E Thompson and Srivatsan Parthasarathy. Moore's law: the future of si micro-electronics. *Materials today*, 9(6):20–25, 2006.

[153] AT Tilke, FC Simmel, RH Blick, H Lorenz, and JP Kotthaus. Coulomb blockade in silicon nanostructures. *Progress in quantum electronics*, 25(3):97–138, 2001.

[154] Alan Mathison Turing. Systems of logic based on ordinals. *Proceedings of the London Mathematical Society*, 2(1):161–228, 1939.

[155] RG Unanyan, BW Shore, and K Bergmann. Laser-driven population transfer in four-level atoms: Consequences of non-abelian geometrical adiabatic phase factors. *Physical Review A*, 59(4):2910, 1999.

[156] LMK Vandersypen, H Bluhm, JS Clarke, AS Dzurak, R Ishihara, A Morello, DJ Reilly, LR Schreiber, and M Veldhorst. Interfacing spin qubits in quantum dots and donors—hot, dense, and coherent. *npj Quantum Information*, 3(1):1–10, 2017.

[157] M Veldhorst, JCC Hwang, CH Yang, AW Leenstra, Bob de Ronde, JP Dehollain, JT Muhonen, FE Hudson, Kohei M Itoh, A Morello, et al. An addressable quantum dot qubit with fault-tolerant control-fidelity. *Nature nanotechnology*, 9(12):981, 2014.

[158] Lorenza Viola and Seth Lloyd. Dynamical suppression of decoherence in two-state quantum systems. *Physical Review A*, 58(4):2733, 1998.

[159] Rutger Vrijen, Eli Yablonovitch, Kang Wang, Hong Wen Jiang, Alex Balandin, Vwani Roychowdhury, Tal Mor, and David DiVincenzo. Electron-spin-resonance transistors for quantum computing in silicon-germanium heterostructures. *Physical Review A*, 62 (1):012306, 2000.

[160] Bent Weber, YH Matthias Tan, Suddhasatta Mahapatra, Thomas F Watson, Hoon Ryu, Rajib Rahman, Lloyd CL Hollenberg, Gerhard Klimeck, and Michelle Y Simmons. Spin blockade and exchange in coulomb-confined silicon double quantum dots. *Nature nanotechnology*, 9(6):430, 2014.

[161] Eric W Weisstein. Confluent hypergeometric function of the second kind, 2003. URL https://mathworld.wolfram.com/ConfluentHypergeometricFunctionoftheSecondKind.html. Wolfram Research, Inc.

[162] Stephen Wiesner. Conjugate coding. *ACM Sigact News*, 15(1):78–88, 1983.

[163] Wikipedia contributors. Zinc sulfide, 2020. URL https://en.wikipedia.org/wiki/Zinc_sulfide. [Online; accessed 05-March-2020].

[164] Wei Wu, Wei-Tao Liu, Yang Han, Ping-Xing Chen, and Cheng-Zu Li. Experimental realization of deterministic entanglement transformations of bipartite pure states. *Optics communications*, 282(10):2093–2096, 2009.

[165] David Yevick and Björn Hermansson. New formulations of the matrix beam propagation method: Application to rib waveguides. *IEEE Journal of Quantum Electronics*, 25(2):221–229, 1989.

[166] David Yevick, Jun Yu, and Yosef Yayon. Optimal absorbing boundary conditions. *JOSA A*, 12(1):107–110, 1995.

[167] Clarence Zener. Non-adiabatic crossing of energy levels. *Proceedings of the Royal Society of London. Series A, Containing Papers of a Mathematical and Physical Character*, 137(833):696–702, 1932.

[168] Igor V Zozoulenko and Martin Evaldsson. Quantum antidot as a controllable spin injector and spin filter. *Applied physics letters*, 85(15):3136–3138, 2004.

A

Double-Slit Simulation Code

```
import numpy as np
import matplotlib.pyplot as plt

x = np.linspace(-200, 200, 1000)
dx = x[1] - x[0]
w = 0.1
xoffset = 40
re = ((w/np.pi)**(1/4)*np.exp(-w*(x-xoffset)**2/2) + (w/np.pi)**(1/4)*↩
    np.exp(-w*(x+xoffset)**2/2))/2
im = np.zeros(len(x))
V = np.zeros(len(x))
dt = 0.005
N = 100000
PrintStep = 100
aa = dt/dx**2
bb = 2*dt

psi2 = np.zeros((int(N/PrintStep),len(x)))
k = 0
for i in range(0, N):
    if i % 2:
```

```
      for j in range(1,len(x)-2):
        im[j] = im[j] +  V[j]*bb*re[j] + aa*(2*re[j] - (re[j-1] + re[j+1]))
    else:
      for j in range(1,len(x)-2):
        re[j] = re[j] - (V[j]*bb*im[j] + aa*(2*im[j] - (im[j-1] + im[j+1])))

    if (i % PrintStep) == 0:
      psi2[k] = re**2 + im**2
      k = k + 1

plt.imshow(np.transpose(psi2), extent=[0,100,-200,200], aspect=0.1, cmap='inferno', vmin=0, vmax=0.01)
plt.xlabel('x (nm)')
plt.ylabel('y (nm)')
# plt.savefig('DoubleSlit.png', dpi=600)
plt.show()
```

Listing A.1 Python solver for the double slit experiment

B

ROOT-OF-SWAP PARAMETERS

Parameter	Value range
Distance between channels	80 nm
Tunnel coupled region start	y_d = 36 nm
Tunnel coupled region end	y_u = 144 nm
Interaction time	$\tau = 36$ ps
SAW amplitude	A_{SAW} = 25 meV
SAW wavelength	$\lambda = 1\mu$m
SAW velocity	v = 3 nm / ps
Harmonic channel confinement	$\omega_x^2 = 0.002 \frac{\mathrm{meV}}{\mathrm{nm}^2 m_e}$
Electron effective mass	0.067 m_e
Relative permitivitty (GaAs)	13.1
Gaussian tunneling barrier amplitude	A_1 = 15.3 meV
Gaussian tunneling barrier width	σ_1 = 30 - 40 nm
Gaussian barrier amplitude	A_2 = 510 meV
Gaussian barrier width	σ_2 = 0.8 nm
Transition between barrier heights	σ_y = 10 nm
Coulomb softening	Δ_z = 10 - 100 nm

Table B.1 Ranges of parameter values used in simulations.

Explicit form of the potentials used in Eq. 6.3, in terms of the parameters above, in the reference frame of the SAW:

$$V_{\mathrm{D}}(x,y) = \frac{m_e}{2}\omega_x^2 x^2 + A_1 \exp\left(\frac{-x^2}{2\sigma_1^2}\right) + \frac{A_2}{2}\exp\left(\frac{-x^2}{2\sigma_2^2}\right) \times \left(2 - \tanh\left(\frac{y-y_d}{\sigma_y}\right) - \tanh\left(-\frac{y-y_u}{\sigma_y}\right)\right), \tag{B.1}$$

$$V_{\mathrm{SAW}}(x,t) = \frac{A_{\mathrm{SAW}}}{2}\left(1 - \cos\left(\frac{x-tv}{\lambda}\right)\right), \tag{B.2}$$

$$V_C(r) = \frac{e^2}{4\sqrt{2}\pi\varepsilon\Delta_z U(-\frac{1}{2},0,\frac{r^2}{2\Delta_z^2})}, \tag{B.3}$$

where U is the confluent hypergeometric function of the second kind, which encapsulates a Gaussian spread with standard deviation Δ_z in the z-dimension:

$$U(a,b,z) = \frac{1}{\Gamma(a)}\int_0^\infty e^{-zt}t^{a-1}(1+t)^{b-a-1}dt. \tag{B.4}$$

C

HETEROSTRUCTURE LAYERS

Layer Material	Thickness (nm)
GaAs	50.0
GaAs	5.0
AlAs	5.0
GaAs	650.0
$Al_{0.34}Ga_{0.66}As$	45.0
Si-Delta	0.0
$Al_{0.34}Ga_{0.66}As$	4.0
$Al_{0.34}Ga_{0.66}As$	46.0
GaAs	5.0

Table C.1 GaAs-AlGaAs heterostructure fabrication thickness.

D

Surface Gate Configuration

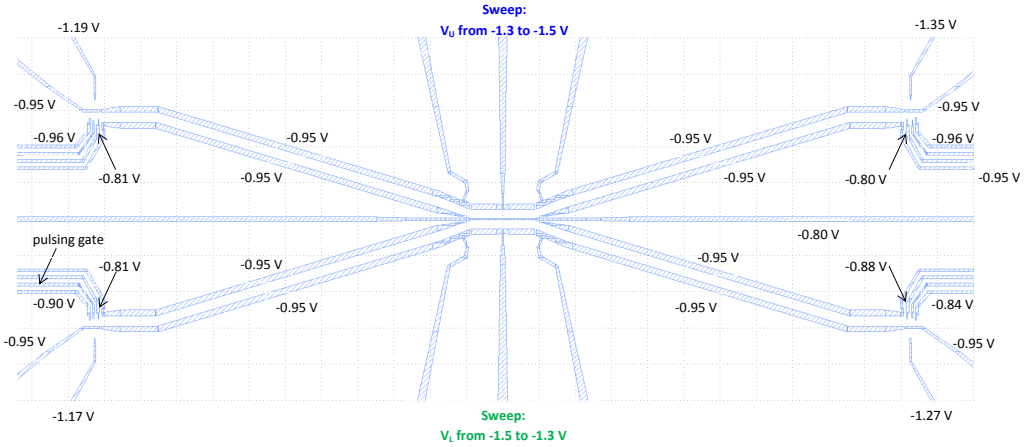

pulsing gate ... 0 V; not used for directional coupler operation